Development and Validation of a Predictive Model of Chemotherapy

in Triple Negative Breast Cancer

By

Matthew Thomas McKenna

Dissertation

Submitted to the Faculty of the

Graduate School of Vanderbilt University

in partial fulfillment of the requirements

for the degree of

DOCTOR OF PHILOSOPHY

in

Biomedical Engineering

December 16, 2017

Nashville, Tennessee

Approved:

Thomas E. Yankeelov, Ph.D.

Michael I. Miga, Ph.D.

Vandana G. Abramson, M.D.

William A. Grissom, Ph.D.

Vito Quaranta, M.D.

To my family

ACKNOWLEDGEMENTS

I first want to first and foremost thank BD, Big Mommy, Katie, Colleen, Unc, and Gram. Graduate school has been challenging, and I am so grateful to have your unwavering support throughout the process. I am thankful for all of the phone calls, visits, and vacations. You have helped me maintain my sanity throughout graduate school.

Monica - I know that you are as excited as I am to wrap up my graduate work. Thank you for your endless patience. It's been quite the experience navigating medical school, graduate school, and residency, and I could not have asked for a better companion for the journey. I also want to particularly thank you for tolerating some pretty gnarly graduate school facial hair.

The Vanderbilt MSTP is the best in the country, and I want to thank the leadership team for gambling on an engineer whose research interests fell outside those of a tradition MSTP student. I vividly remember getting the call from Dr. Dermody with my admission offer, and I can only hope that I have done the program proud. I am grateful for the continued support of the leadership team throughout my time in the MSTP. Drs. Dermody, C. Williams, York, Winder, Estrada, Bills, Swift, and M. Williams – Thank you! I particularly want to recognize Melissa Krasnove. You make the MSTP run, and I have appreciated all of our conversations throughout my time in the MSTP. I also want to thank the MSTPals. I believe we are the strongest class in the MSTP. Thank you for your friendship, and thank you for sharing your experiences in graduate school. Your companionship has helped me through the challenges of graduate school.

While several people contributed in this work, I especially want to thank Dr. Jared Weis and (soon-to-be) Dr. Bishal Paudel. Jared – our conversations were critical in developing the ideas detailed throughout this Dissertation. I appreciate all of the modeling wisdom you imparted to me, and I am thankful for your patience in listening to me ramble about science. Bishal – I have really enjoyed working in lab with you. It was motivating to see how hard you work, and I really appreciated all of our scientific (and not-so-scientific) conversations.

To my advisor, Tom Yankeelov: Thank you. Thinking back to the Aims page we first developed, I could not have foreseen the research that I have completed over the last three years. Accordingly, I have appreciated the freedom you have given me to explore my own ideas. Thank you for all of the paper edits and all of the college basketball discussions. I can only hope to emulate your work ethic and communication skills, and I aspire to balance work and home life as well as you do. Your mentorship has made me a better scientist and person. I look forward to

working with you as we carry on the ideas developed in this Dissertation, and I am excited to see what you build down in Texas.

To my committee members, Professors Michael Miga, Vito Quaranta, William Grissom, and Vandana Abramson: Thank you for your insight and time. I particularly would like to thank Dr. Miga and his graduate students for adopting me for the latter half of my graduate work, and Dr. Quaranta for giving me space to work in his lab. This work was spread over several labs and disciplines, and I am thankful that you fostered an environment that let me pursue such research.

TABLE OF CONTENTS

LIST OF TABLES

LIST OF FIGURES

CHAPTER 1

PRECISION MEDICINE WITH IMPRECISE THERAPY: COMPUTATIONAL MODELING FOR BREAST CANCER THERAPY

1.1 Introduction

On May 25, 1961, President Kennedy proposed to Congress that the United States should commit itself to "landing a man on the moon and returning him safely to earth" by the end of the decade. Similarly, on December 23, 1971, President Nixon signed into law the National Cancer Act and stated it was time for the concentrated effort that resulted in the lunar landings to be turned towards conquering cancer. Of course, Neil Armstrong first set foot on the lunar surface on July 20, 1969, yet 46 years after Nixon's announcement we have made only modest advances in controlling this disease. This is particularly striking with the renewed lunar-centric announcement of the Cancer Moonshot Initiative by former President Obama in his 2016 State of the Union. A fundamental difference between the planetary and cancer moonshots is that the basic mathematics for gravity were known for nearly three centuries at the time of Kennedy's speech, while we still do not have a mathematical description of cancer that allows us to compute the spatiotemporal evolution of an individual patient's tumor. In the current state of oncology, we are tasked with getting to the moon without knowing $F = ma$.

Precision medicine is the concept of incorporating patient-specific variability into prevention and treatment strategies (1). The advent of precision medicine has brought significant advances to oncology. The majority of these efforts have focused on the use of genetics to classify and pharmaceutically target cancers (2). This approach has led to a paradigm in which tumor genotypes are matched to appropriate treatments (3,4). For example, the addition of trastuzumab, a monoclonal antibody targeting the human epidermal receptor 2 (HER2) protein, to chemotherapeutic regimens in breast cancer patients with HER2-positive disease has resulted in improved disease-free and overall survival (5). While the current genetic-centric approach to cancer therapy has great merit in appropriately selecting therapies and identifying new pharmaceutical targets, it can frequently overlook a host of patient-specific measures that influence response to therapy. For example, the microenvironment of the tumor alters response (6), delivery of therapy to tumors is variable as tumor perfusion is limited (7,8), and patient-specific

pharmacokinetic properties vary (9,10). Furthermore, the schedule on which therapy is given may significantly alter response (11–13). These issues may be partly responsible for the high attrition rates of proposed cancer therapeutics (14).

The goal of precision medicine is to tailor therapeutic strategies to each patient's specific biology. More specifically, we define the goal of precision medicine to be the use of the optimal dose of the optimal therapy on the optimal schedule for each patient. Under this interpretation, there is an opportunity to expand precision oncology beyond the tumor-genotype-driven selection of therapy. The challenge facing expansion of precision oncology into the dosing and scheduling realm is two-fold. First, new hypotheses related to optimal dosing and scheduling are needed. Whereas the hypotheses in genetic studies often compare tumor volume changes to a static genetic marker, dosing and scheduling require temporally-resolved hypotheses and concomitant treatment response measures. In particular, such hypotheses would need to specify *quantitatively* how the tumor microenvironment and/or patient pharmacokinetics influence response to therapy in order to adapt therapeutic approaches to measured responses. Second, biomarkers are needed to provide clinically-relevant insights into tumor behavior and to inform these new hypotheses. Fortunately, the tools to probe cancer from the genetic to tumor scales have rapidly matured over the past decade. While more time is needed to fully understand and contextualize the micro-, meso-, and macro-scale data coming online, several groups have demonstrated the utility of new technologies. For example, advances in imaging technologies, such as diffusion weighted magnetic resonance imaging (DW-MRI) and dynamic contrast enhanced MRI (DCE-MRI), have led to the discovery of clinically-relevant biomarkers that are predictive of response (15). To rephrase the second challenge, new approaches are needed to synthesize available biomarkers to test new hypotheses. We (and others (16–18)) believe that mathematical modeling holds the potential to not only improve our ability to treat cancer, but it will also allow precision cancer care to enter the dosing and scheduling domains.

A goal of mathematical modeling is to abstract the key features of a physical system to succinctly describe its behavior in a series of mathematical equations. In this way, the system can be simulated *in silico* to further understand system behavior, generate hypotheses, and guide experimental design. When experimental data is available, model predictions can be compared to those data. The model can then be iteratively refined to account for data-prediction mismatches. Models can also identify high-yield experiments in cases where an exhaustive investigation of

experimental conditions is infeasible (19). Traditionally, cancer models are built off of first order biological and physical principles, such as evolution (20) and diffusion (21). Part of the recent excitement about applications of mathematical models to cancer is the discovery of higher-order, emergent properties that any one model component does not possess (22). For example, cancer models have been constructed to investigate the role of tumor cell-matrix interactions in shaping tumor geometry and in enhancing selective pressures (23). Fundamentally, models built from these first principles are designed to discover new biological behaviors and principles, identify new hypotheses for further investigation, and predict the behavior of cancer systems to perturbations. These models are tuned with any available data and simulated to discover system properties (18). However, the majority of these models are not structured to leverage currently-available clinical data to make patient-specific predictions (24). Often, these complex mechanism-based models have been limited to *in silico* exploration, and their utility in generating patient-specific predictions remains to be investigated.

There is an opportunity to reverse the modeling approach. Instead of modeling cancer from first principles, models can be built to predict the changes in clinically-available tumor measurements. Models need not be "true" to be useful; as George Box famously noted, "all models are wrong, but some are useful" (25). Medical oncology is in need of a mathematical, mechanism-based modeling framework in order to leverage all available clinical information, spanning from tumor genetic to tumor imaging data, to make impactful changes on patient management (26). In this way, models can be used to make specific and measurable predictions of the response of an individual patient to an individualized therapeutic regimen. While these models will be "wrong," in that they will not explicitly consider all scales of biological interactions, they may be of practical utility by consolidating clinically-available data sources into a coherent understanding of tumor growth and treatment response.

The interaction of matter is governed by weak nuclear, strong nuclear, gravitational, and electromagnetic forces just as the behavior of cells is governed by genetics. However, for macroscopic objects traveling at speeds much less than the speed of light, $F = ma$ is an excellent approximation of the movement of those objects. While the understanding of fundamental physical laws is still being advanced, a complete understanding is not necessary to leverage classical mechanical models to engineer mechanical tools (such as a rocket to lift astronauts to the moon). There is an opportunity in oncology to develop an analogous "classical oncology" toolkit. We posit

that a complete understanding of cancer is not necessary to create tools that leverage clinical data to improve the treatment of cancer. This toolkit will likely consist of "simple" models that approximate the behavior and treatment response of tumors. Fortunately, the tools to make analogous force measurements in cancer already exist.

This perspective will highlight the utility of modeling and discuss opportunities for modeling in breast cancer treatment. We begin by reviewing the use of mathematical models in clinical oncology, including those used in radiation oncology. We draw parallels between dose planning in radiation therapy and chemotherapy and propose how mathematical modeling approaches can leverage current technologies to more precisely use anti-cancer chemotherapies. We then highlight opportunities for investigation in the clinical evaluation of response in the context of patient-specific modeling. To limit the scope of this perspective, we will focus on cytotoxic chemotherapeutics (defined below). It is the goal of this perspective to provide guidance and highlight opportunities for a classical oncology toolkit.

1.2 Models for Clinical Oncology

We now examine the use of mathematical models in both medical and radiation oncology. Specifically, we will focus on the theory and models used to define chemotherapy administration schedules and dose. While surgical oncology has incorporated mathematical modeling approaches, especially in image-guided surgical approaches (27), such discussion falls outside of the scope of this perspective. We review these concepts in the context of our definition of precision medicine: the use of the optimal dose of the optimal therapy on the optimal schedule for each patient.

1.2.1 Medical Oncology

Cytotoxic drugs, which are designed to inflict lethal insults on rapidly-dividing cells, were among the first pharmaceuticals used to treat breast cancer (the first clinical trial started in 1958 (28)), and they remain a critical component of current therapeutic regimens. The modern era of chemotherapy was born from the observation that mustard gas induced myelosuppressive states and was effective in treating hematologic malignancies (29). Dosing schemes with these agents all follow a common pattern: cycles of a high dose nearing the maximum tolerated dose followed by a recovery period. The goal of this strategy is to maximize tumor cell kill, while trying to minimize adverse effects *via* drug holidays between each cycle. While tumors often respond to these

4

therapies, there is a high rate of tumor recurrence. For example, the 5-year progression free survival rate for triple negative breast cancer (TNBC) patients is 61% (30). Furthermore, cytotoxic therapies often have lasting effects on survivors, adversely affecting their quality of life. For example, doxorubicin, a standard-of-care therapy for the treatment of TNBC, is associated with cardiomyopathy (31).

When cytotoxic therapy was first applied to cancer, few mathematical principles existed to guide its use (32). While the cytotoxic properties of these agents had clearly been demonstrated in animal models, the subsequent translation into a human population lagged behind. Skipper first observed the relationship between tumor size and treatment response when he discovered leukemia response to therapy to be proportional to the number of malignant cells (33). He hypothesized that each dose of treatment kills a fixed percentage of tumor cells. This necessitates repeated dosing strategies to increase the odds of tumor eradication. In essence, he defined the log-kill hypothesis. Specifically, the log-kill hypothesis is defined:

$$\log\left(N_{SF}\right) = \log\left(N_{T}\right) - k \quad,$$

where N_{SF} is the fraction of tumor that survives treatment, N_{T} is the tumor size at the time of treatment, and k is the efficacy of treatment. This model assumes the tumor is composed of a homogeneous mixture of cells equally sensitive to treatment, and a fixed fraction of those cells are killed with each treatment. Despite the relatively simplicity of the model, its practical implication was profound: chemotherapies should be delivered several times, even after the disappearance of macroscopic tumors, to eradicate all tumor cells. This was a departure from the current practice of the time, in which chemotherapeutic agents were given over a short course to treat solid tumors (28). Skipper's observation challenged this paradigm, and multi-dose treatment regimens were supported by subsequent clinical trials in the 1970's (34,35), forming the basis of modern adjuvant and neoadjuvant chemotherapy approaches. Subsequently, investigators sought to improve response through dose escalation. The dose escalation trials were met with limited success, as several agents demonstrated a saturated response curve at high doses (36,37).

Investigation into the scheduling of therapeutics was advanced when Norton and Simon hypothesized that tumors grow according to Gompertzian kinetics (38,39). Specifically, Gompertzian growth can be expressed:

$$\frac{dN\left(t\right)}{dt} = BN\left(t\right)I\left(t\right)$$

$$\frac{dI(t)}{dt} = \log\frac{N(t_\infty)}{N(t)} \; ,$$

Where $N(t)$ is the tumor volume at time t, B is the growth rate of the tumor, $I(t)$ is a function describing how the growth rate slows as the tumor volume approaches some maximum volume, $N(t_\infty)$, as t approaches infinity. Qualitatively, these equations indicate that tumors grow exponentially, with an exponentially decreasing growth rate. Treatment response was assumed proportional to tumor growth rate, with smaller, faster growing tumors responding more robustly to treatment than larger slower-growing tumors. In the context of Gompertzian growth, treatment at time t_{rx} can be modeled as:

$$\frac{dN(t)}{dt} = \left(1 - D_i(t)\right)BN(t)I(t)$$

$$D_i(t) = \begin{cases} 0, t < t_{rx} \\ > 0, t \geq t_{rx} \end{cases} ,$$

where D_i is the magnitude of the anti-tumor effect of treatment i, regardless of its functional form (radiotherapy, chemotherapy, immunotherapy, etc.). Norton and Simon noted that the functional form of D would be specific to the intervention (38). As this is a description of tumor volume, these parameters describe the multifactorial response to therapy, including the effects of cell death, removal of cells, attraction of leukocytes, etc. For tumors treated with multiple doses of chemotherapy, the treatment term, $D(t)$, is proportional to the integrated drug concentration, C, and the sensitivity of the tumor to the current therapy, k: $D(t) \approx k\int_{t_0}^{t} C(\tau)d\tau$ (40). Similar to the log-kill model, the Norton-Simon hypothesis is relatively simple yet impactful. The model indicates that chemotherapy is best delivered to small, fast-growing tumors on a dose-dense schedule, minimizing the time between treatments. This approach limits the regrowth of tumors between treatments, meaning smaller tumors are being treated. Per the model, smaller tumors grow more quickly, rendering them increasingly responsive to treatment thereby maximizing therapeutic effect. This approach was validated in a clinical trial (11).

Multi-agent regimens were introduced in order to address tumor heterogeneity, in the hopes of eliminating tumor cells resistant to single agent therapy. Following the Goldie-Coldman hypothesis, which proposes that multi-agent chemotherapies should be delivered in alternating courses (e.g., ABABAB instead of AAABBB) to minimize the probability of developing

resistance (41), empiric schedules of administration for these multi-agent regimens were tested in clinical trials (42). While multi-agent regimens demonstrate improved efficacy relative to single-agent treatments, the scheduling of therapeutics remains an open question. For example, in trials investigating the reordering of treatments to avoid development of resistance according to the Goldie-Coldman hypothesis, the schedules that delivered therapy most quickly (regardless of order) were found to be superior (42). While different schedules have been hypothesized to significantly impact response (13,43,44), empiric schedules remain as a matter of practicality as there exist innumerable combinations of drugs and schedules that cannot be tested clinically.

While several more complicated models of tumor growth and treatment response have been proposed in the literature (45), the models highlighted have been the only to penetrate clinical practice. We suppose these have gained traction because each provided a precise, clinically-testable hypothesis for improved cancer treatment. However, these models are limited to making general predictions for the use of chemotherapy. Further, the above hypotheses were developed to maximize the rate of tumor cell kill, which is assumed to improve long-term, disease-free survival; however, growing evidence suggests this may not be the optimal therapeutic approach (46).

The dosing of chemotherapeutics also has a mathematical basis. Doses of chemotherapeutic agents are often personalized through use of patient body surface area (BSA) (47,48). BSA was first proposed as a guide for chemotherapy dosing by Pinkel, noting that the accepted cytotoxic dose for pediatric and adult patients, and the dose used in laboratory animals correlated with BSA across those scales (49). This approach has been advocated by the Food and Drug Administration, recommending BSA be used to scale preclinical *in vivo* doses to patients in phase I clinical trials (50). Several BSA models have been developed over time, primarily differing in the coefficients used in their calculation. For example, a common formulation, which was proposed by Gehan and George (51), defines BSA as:

$$BSA = 0.02350 \times \text{height}^{0.422246} \times \text{weight}^{0.51456} ,$$

where the coefficients in this function are derived from BSA measurements from 401 individuals. While a BSA-based dosing strategy is of great practical utility for calculating doses for each patient, BSA correlates poorly with the underlying physiological processes that affect drug pharmacology (e.g., liver metabolism and glomerular filtration rate) (52). Specifically, BSA has been found to correlate poorly with patient pharmacokinetic properties for several chemotherapies (53). For example, in a study of 110 patients receiving doxorubicin therapy,

doxorubicin clearance was found to weakly correlate with BSA ($r = 0.34$). Further, the reduction in variance in doxorubicin clearance when normalized by BSA was only 0.8%, meaning that only a small fraction of the variance in clearance can be attributed to BSA (9). Despite the weak relationship between BSA and pharmacokinetics for several therapeutics, BSA remains widely used to guide dosing in the clinic.

1.2.2 Radiation Oncology

Similar to chemotherapy, radiation therapy was once delivered in a single, high dose (54). Contrary to chemotherapy, in which a theory of treatment response was established prior to changes in therapeutic application, radiation doses were quickly fractionated to account for excessive toxicities in healthy tissue. Briefly, radiation therapy leverages ionizing radiation to damage the DNA of tumor cells (although recent research suggests lower-dose radiotherapy may primarily target the cell membrane or cytoplasm) (55). The DNA damage induced by radiation can lead to immediate cell death *via* apoptosis, senescence, autophagy, or necrosis or a delayed cell death *via* mitotic catastrophe (56).

The interaction of photons with DNA can be physically modeled as a stochastic process. The probability of the number of photon-tissue interactions can be described using Poisson statistics:

$$P(n) = \frac{e^{-D}D^n}{n!},$$

where $P(n)$ is the probability of n interactions, and D is radiation dose in units of Gray (defined to be one joule of energy absorbed per kilogram of matter). If a single interaction is assumed to result in cell death, the probability of survival ($n = 0$) is simply e^{-D}. For viruses, bacteria, and very sensitive human cells, it is an appropriate model of survival (57). However, this model fails to describe survival in other human cell types. For these tissues, the linear-quadratic (LQ) model was found to be the most parsimonious model that fit the observed survival curves (57,58). The LQ model is expressed as:

$$P(survival) = e^{-\alpha D - \beta D^2},$$

where α and β are radiosensitivity parameters, and D is dose. As β approaches zero, the LQ model approaches the Poisson model of cell survival. The LQ model can be used to characterize the radiosensitivity of different tissues with two parameters (α and β). One potential biological

interpretation of the linear-quadratic model is offered by the lethal-potentially lethal damage (LPL) model (59). The LPL model posits that the linear portion of the LQ model are cells that receive non-repairable lethal lesions after a single hit (radiation dose). The quadratic portion is representative of repairable lesions that may eventually die to subsequent lesions or misrepair.

The LQ formalism can be used to explain why fractionated radiotherapy was superior to single doses (there are additional biological rationales for the use of fractionated therapy (60), but these have yet to be formalized into a mathematical modeling framework). Fractionation approaches leverage differential radiosensitivities of tissues (i.e., tumor and healthy tissues) to maximize efficacy while minimizing off-target toxicities. In planning treatment schedules, the effect of therapy on the tumor (generally high α/β ratios) must be balanced with both the acute and long-term toxicities of surrounding, healthy tissue (lower α/β ratios). For a fixed duration of treatment, the isoeffect doses (i.e., doses that have an equivalent biological effect) of different fractionation schedules can be compared (61):

$$\frac{D_2}{D_1} = \frac{d_1 + (\alpha/\beta)}{d_2 + (\alpha/\beta)},$$

where D_i is the total dose for each fractionation scheme, d_i is the dose per fraction, and α/β is a measure of tissue-specific radiosensitivity. For late-responding healthy tissues (i.e., for tissue with low α/β), the total isoeffective dose increases more quickly than acutely-responding tissue (i.e., high α/β) when doses are hyperfractionated (i.e., smaller doses with more fractions). This means that fractionation schedules allow for higher isoeffective doses in tumor tissues compared to surrounding healthy tissue. For this reason, radiotherapy is typically given at low doses over several sessions to maximize tumor dose and to minimize damage to healthy tissue. For example, in head and neck cancer with high α/β ratios (>7 Gy) (62), a hyperfractioned schedule has been shown to be superior to conventional schedules with fewer fractions (63). While patient-specific biology underlies the α/β parameters for tumors and surrounding tissue, interpatient variability in parameters is often not considered in clinical practice, yielding a single schedule for many patients receiving radiotherapy. For example, some tumors demonstrate similar α/β ratios to the surrounding healthy tissue. Specifically, breast cancers have relatively smaller α/β ratios (4 Gy) (62). In this case, a schedule using higher doses and fewer treatment sessions (hypofractionation) may be superior (64).

In addition to its explicit consideration of off-target toxicities, radiation therapy differs from chemotherapy in dose planning. As noted above, in radiation therapy, dose is defined as the energy absorbed per unit mass. This differs from the use of "dose" in chemotherapy as the amount of drug given to the patient (not necessarily the amount of drug delivered to tissue). Radiation dose planning involves leveraging patient-specific anatomy to maximize dose delivered to the tumor while minimizing off-target effects (65). As the physics governing tissue irradiation are well-characterized, physical models can be defined to estimate spatially-resolved radiation dose prior to treatment. Several algorithms have been developed to efficiently calculate dose distribution for each patient (66). Generally, these methods model photon interactions (e.g., photoelectric effect and Compton scattering) to simulate the energy absorbed by tissue. Several of these methods leverage a Monte Carlo approach to estimate spatially-resolved dose estimates, simulating the path of each photon through tissue probabilistically with a random number generator (67). Briefly, the probability that a photon will travel a distance l without undergoing any interactions can be defined:

$$P(l) = 1 - e^{-\mu l},$$

where μ is the attenuation coefficient, which is a function of photon energy (E) and the physical properties of the material the photon encounters:

$$\mu(E) = \rho N_A \sum_i \left(\frac{w_i}{A_i} \sigma_i(E) \right),$$

where ρ is the mass density, N_A is the Avogadro constant, w_i the elemental weight (i.e., fractional composition) of element i in the material, A_i is the atomic mass of element i, and σ_i is the total cross section for element i (which is a value describing element-photon interactions such as Compton scattering) (68–70). By modeling these interactions, spatially-resolved dose maps and the corresponding uncertainty in those estimates can be calculated. Importantly, the uncertainty in radiation dose translates into uncertainty in tumor control probability (71). While this relationship depends on tumor-specific dose response curves, Boyer and Schulteiss estimated that the cure of early stage patients increases 2% for every 1% improvement in accuracy of dose delivery (i.e., spatially-resolved dose deposition) (72).

Critically, X-ray computed tomography images, which generate spatially-resolved μ values, can be used to estimate the tissue parameters needed for Monte Carlo simulation of dose distribution (70). This modeling framework allows for the use of *patient-specific* imaging data to

design *patient-specific* dose plans. Indeed, Rockne and colleagues demonstrated how imaging data can be used to estimate radiation response parameters to design treatment schedules that maximize tumor response in glioblastoma (17,73).

1.3 Current Opportunities in Modeling Systemic Therapies

A key step in the evolution of precision cancer therapy will be understanding interpatient variability in drug delivery and drug response and using those differences to personalize drug dosing and administration schedules (74). Mathematical models can be used to explore these relationships. However, model behavior is reliant on the parameter values used in model evaluation, and many of the variables in proposed models are difficult to measure clinically (19). This presents a fundamental hurdle in the translation of these approaches into clinical practice. If these models are dependent on un-observable data, the utility of these models in making patient-specific measurements and predictions is greatly reduced.

There is a need to develop methods to measure the biological processes underlying treatment response variability. These measurements can then be used to parameterize predictive mathematical models to optimize treatment plans. Just as the linear-quadratic model can be used to characterize the radio-sensitivity of tissue, models can be applied to clinically-available data to derive measurements of tumor behavior. Below, we reimagine the use of cytotoxic chemotherapies in breast cancer considering this interpatient variability, applying lessons learned from radiation oncology to the technologies available clinically.

While the differences in chemotherapy and radiotherapy are apparent, we note fundamental similarities between these modalities. First, several commonly-used chemotherapeutics, such as doxorubicin and cisplatin, are DNA-damaging agents. The response to these therapies can reasonably be compared to the DNA damage of photon therapy. Second, both chemotherapy and radiation therapy share a fractionated dosing schedule. While there exists a formalism for dose fractionation in radiation therapy with the linear-quadratic model, chemotherapies lack a widely-adopted quantitative approach to dose scheduling that balances tumor efficacy with off-target effects.

In our opinion, one of the more prominent discrepancies in these treatment modalities is their respective definitions of dose. There may exist practical reasons for this difference. An external radiation beam can be accurately tuned and targeted, and the physics of photon

interactions are well-understood. Alternatively, medical oncologists must leverage patients' circulatory systems to delivery therapeutics to tumors. While the pharmacokinetic properties of patients can be measured, this delivery method is inherently more imprecise. However, as we highlight below, the technology to estimate patient-specific pharmacokinetic and pharmacodynamic (PK/PD) properties may already be available clinically.

1.3.1 Therapeutic drug monitoring

Therapeutic drug monitoring (TDM) is the concept of adjusting therapeutic doses on a patient-specific basis to maximize drug efficacy. Paci *et al*. reviewed the relevance of TDM in the use of cytotoxic anticancer drugs (75). They argue that the use of cytotoxic drugs meet the prerequisites for TDM, specifically: 1) a large variance in inter-patient PK parameters, 2) a defined relationships between PK and PD parameters, and 3) a delay between PD end-point and time of measurement of plasma concentration. For several cytotoxic agents dosed by BSA, pharmacokinetic measurements among patients may vary over an order of magnitude (53). Given the high variability in PK properties and the narrow therapeutic window (i.e., the range of drug doses that can effectively treat a disease process without having toxic effects) for cytotoxic agents, this variability may be a cause for treatment failures (76,77). For example, significantly better outcomes were observed in children with B-lineage acute lymphoblastic leukemia when chemotherapy was dosed to reflect patient-specific clearance rates instead of BSA (78).

The concentration of drug in blood plasma can be measured *via* a variety of clinical chemistry techniques (e.g., immunoassays or chromatography (79)), and these measurements can be used to parameterize pharmacokinetic models that describe the absorption, distribution, metabolism, and excretion of a therapeutic agent (80). Compartment models are often employed as pharmacokinetic models. In the context of pharmacokinetics, compartment models separate the body into physiologically-defined volumes (e.g., blood plasma, liver, kidney) that are each assumed to be homogenous with respect to drug concentration. These compartments are defined to communicate with each other with a set of rate constants. Such physiology-based pharmacokinetic models have been leveraged to describe the pharmacokinetics of several anti-cancer agents including doxorubicin (81). For example, a simple pharmacokinetic model that describes transfer of drug between the blood plasma and tissue can be defined:

$$\frac{dC_B}{dt} = -k_{BT}C_B + \frac{V_B k_{TB} C_T}{V_T} - k_e C_B \ ,$$

where C_B and C_T are the concentrations in the blood plasma and tissue, V_B and V_T are the volumes of the blood and tissue compartments, respectively, k_{BT} is the rate constant describing the movement of drug from the blood into tissue, k_{TB} is the rate of drug movement from tissue back into blood, and k_e is rate at which drug is eliminated from the tissue.

Measurements of plasma drug concentrations offer an alternative to BSA to more precisely account for inter-patient variability in drug pharmacokinetics. For example, Bayesian methods have been employed to leverage limited blood plasma samples to estimate an individual's pharmacokinetic properties (82). These *a posteriori* estimates can be used to guide future dosing of therapeutics. Indeed, some clinical trials have leveraged simple PK/PD models to optimize therapy for patients (83,84). Alternatively, *a priori* dose adjustments can be made leveraging covarying patient properties. For example, carboplatin clearance was found to strongly correlate with kidney function, allowing for an empiric formula based on glomerular filtration rate (a measure of kidney function) to be derived for dosing (85). Using these approaches to populate pharmacokinetic models will help reduce inter-patient variability and will play a role in the realization of personalized drug treatment schedules (80,86).

1.3.2 Tumor-specific drug distribution

Inducing and sustaining angiogenesis is a hallmark of cancer (87). Tumor vasculature is often morphologically and functionally immature. Relative to a healthy vasculature, tumor vasculature is tortuous and leaky with numerous blind endings and arteriovenous shunts. This impairs delivery of nutrients causing local microenvironmental changes that alter the response to therapy (6,88,89). Further, significant heterogeneity in perfusion exists within a tumor, impacting both tumor growth and drug delivery (90). Differences in treatment response may arise due to variability in tumor perfusion.

Tumor vasculature can be assessed with dynamic contrast enhanced magnetic resonance imaging (DCE-MRI). In DCE-MRI, a series of images are collected before and after a contrast agent is injected into a peripheral vein. Each image represents a snapshot of the tumor in time. Each voxel in the image set gives rise to its own time course which can be analyzed with a pharmacokinetic model to estimate physiological parameters such as the contrast agent transfer

rate (K^{trans}, related to vessel perfusion and permeability), the extravascular extracellular volume fraction (v_e), and the plasma volume (v_p):

$$C_t(t) = v_p C_p(t) + K^{trans} \int_0^t C_p(\tau) e^{-k_{ep}(t-\tau)} d\tau,$$

where $C_t(t)$ is the timecourse of the concentration of contrast agent in the tissue of interest, and $C_p(t)$ is the timecourse of the concentration of contrast agent in the blood plasma (91).

DCE-MRI parameters have been shown to be predictive of tumor response to therapy (92). DCE-MRI data have been used in mechanistic models to estimate local nutrient and drug gradients within tumors. For example, in a model of treatment response in breast cancer, increased heterogeneity on DCE-MRI was identified to be a predictor of poor treatment outcomes. The increased transport heterogeneity was found to be associated with increased tumor growth and poor drug response (93). In theory, DCE-MRI data could be coupled with patient-specific PK measures (i.e., plasma drug concentration timecourses) to create tumor-specific drug distribution maps. Tagami *et al*. realized the goal of estimating intratumoral drug distribution through a related MRI approach which employed drug encapsulated with an MRI contrast agent. Changes in MR T_1 relaxation time were measured and correlated with distribution of drug within tumors (94). Coupling measurements of tumor vasculature with mathematical models of drug diffusion through tissue (95) will allow for the modeling the response of tumor cells to therapy to be decoupled from the tumor vasculature, thereby removing a source of variability in patient response.

1.3.3 Tumor-Specific PD Modeling

The efficacy of cytotoxic agents is defined by their ability to induce tumor cell death. Even within a clinically-defined grouping of tumors (e.g., triple negative breast cancer), there exists significant differences in tumor sensitivity to treatment (96). The assessment of tumor pharmacodynamics is limited to unidimensional tumor changes as defined by the Response Evaluation Criteria in Solid Tumors (RECIST (97)). Briefly, RECIST focuses on changes in the sum of the longest dimension of tumors to assess response to treatment. These changes in tumor size are temporally downstream effects of therapy, limiting the utility of this approach to adapt treatments based on patient-specific tumor measurements. The ability to assess tumor response to treatment in real time is needed to adapt therapy schedules to maximize the odds of treatment success. We now describe three technologies that have been used to monitor treatment response

upstream of tumor volume changes: diffusion-weighted magnetic resonance imaging (DW-MRI), fluoro-deoxyglucose positron emission tomography (FDG-PET), and circulating tumor DNA (ctDNA) samples.

Cellular changes within the tumor precede tumor volume changes. In DW-MRI, the diffusion of water molecules through tissue is measured and described by the apparent diffusion coefficient (ADC). This modality relies on the thermally-induced random movement of water molecules (known as Brownian motion). In tissue, this movement is not entirely random as water molecules encounter a number of barriers to diffusion (e.g., cell membranes and extracellular matrix), and the observed diffusion largely depends on the number and separation of barriers that a water molecule encounters. DW-MRI methods have been developed to measure the ADC at the voxel level, and in well-controlled situations the variations in ADC have been shown to correlate inversely with tissue cellularity:

$$N\left(\bar{x},t\right)=\theta\left(\frac{ADC_{\text{water}}-ADC\left(\bar{x},t\right)}{ADC_{\text{water}}-ADC_{\text{min}}}\right),$$

where $N\left(\bar{x},t\right)$ is the number of tumor cells at position $\bar{x}$ and time t, ADC_{water} is the ADC of water at 37° C and ADC_{min} is the minimum observed value that corresponds with θ, the carrying capacity of each voxel (98). Changes in tumor ADC precede tumor volume changes, providing an early biomarker of treatment response (99).

Changes in tumor metabolism can precede tumor morphology changes and may be predictive of treatment response in breast cancer (100). FDG-PET provides a measure of glucose metabolism in tumors. In FDG-PET, ^{18}F-FDG is injected into a peripheral vein. As it circulates, the FDG is transported into cells and phosphorylated, trapping the FDG within cells. As ^{18}F-FDG decays, it emits positrons, which annihilate with nearby electrons. Each annihilation yields two (nearly) antiparallel 511 kEV photons, which are detected and used to map FDG distribution. FDG-PET data are summarized by the standardized uptake value (SUV), which normalizes for patient weight and injected dose as follows:

$$\text{SUV}=\frac{r}{a'/w},$$

where r is the measured radioactivity activity concentration in a region of interest, a' is the decay-corrected amount of injected radiolabeled FDG, and w is the weight of the subject (101).

Tumors continually shed DNA into the bloodstream during the course of tumor development. These circulating tumor DNA (ctDNA) samples potentially may serve as "liquid biopsies," providing measurements on the mutational status of tumors, assessment of treatment response, and guidance for therapy selection (102–104). Notably, these data have been shown to be an early predictor of relapse in breast cancer patients (105).

Taken together, these measurements of tumor pharmacodynamics can be leveraged to parameterize models to describe the tumor response to treatment. For example, since ADC changes following treatment are predictive of ultimate treatment response (106), our group has demonstrated how ADC values can be used to estimate response rates of tumors:

$$N\left(\overline{x},t\right)=\theta\left(\frac{\theta N\left(\overline{x},t_0\right)}{N\left(\overline{x},t_0\right)+\left(\theta-N\left(\overline{x},t_0\right)\right)e^{-k\left(\overline{x}\right)t}}\right),$$

where $N\left(\overline{x},t\right)$ is the number of tumor cells at position $\overline{x}$ and time t and k is the spatially-dependent growth rate (21). This measure of tumor response can be combined with the assessment of off-target hematologic toxicities, providing a pathway to personalize chemotherapy schedules through PK/PD optimization (107). Similarly, Liu and colleagues have incorporated SUV measurements derived from FDG-PET imaging into a predictive tumor growth model (108). ctDNA data can be used to track tumor genetic changes and populate evolutionary dynamics models to predict treatment response (18). The above technologies present independent means to assess tumor response to therapy. With appropriate mathematical models incorporating the data from these modalities, real-time adjustment of therapeutic schedules in response to tumor changes may be possible.

1.4 Vision for Systemic Chemotherapy

Given the goal of delivering the optimal therapy on the optimal schedule for each patient, we highlighted some potential tools for realizing that goal in Section 1.3. As noted above, overly complex models, which require several parameters to be estimated for each patient, present a difficult task in translation to a clinical population. Radiation oncology relies on a relatively simplistic approximation of dose response to develop treatment schedules. Potentially, such simple models may improve the use of chemotherapy by integrating currently available measurements of treatment response. It is our vision that a classical oncology toolkit be available to clinicians, to

16

leverage measurable patient data to not only select appropriate treatments but also optimize the schedule on which those therapies are given (Figure 1.1).

Figure 1.1: Vision for systemic chemotherapy. Following diagnosis and staging of a cancer, a patient is evaluated clinically with a panel of imaging tests and bloodwork. These data that quantify various tumor properties, drug pharmacokinetics, and off-target toxicities are used to parameterize a mathematical model of treatment response. This model can then be leveraged to identify optimal treatment plans. This process is repeated throughout the course of treatment to yield treatment plans that co-evolve with the patient's tumor.
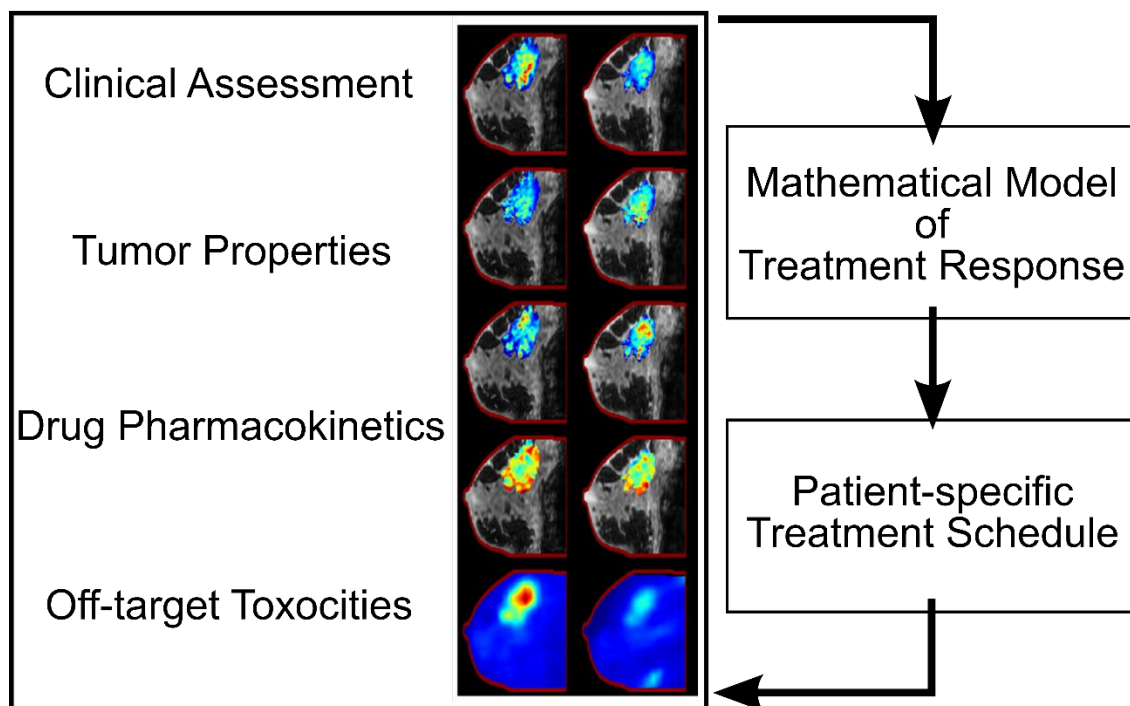
Following diagnosis and staging of tumors, the patient would be evaluated with a panel of imaging tests and bloodwork. Following an initial round of therapy (and, on occasion, through the course of therapy), the testing is repeated, providing data to initialize and constrain predictive models of treatment response. A pre-defined objective function that balances tumor efficacy with off-target toxicities is then parameterized with the patient-specific data and optimized to identify a patient-specific treatment schedule. Simply, the objective of cancer therapy is to maximize survival while minimizing morbidity. Formally, we define:

$$\max_{x} Survival = f\left(Tumor\left(x\right)\right) + g\left(\sum_{organs} Toxicity\left(x\right)\right),$$

$$\text{subject to } \sum_{organs} Toxicity\left(x\right) \leq Toxicity_{max,organ}$$

where x is the therapy schedule, f is the functional relationship between tumor behavior and survival, and g is the functional relationship between off-target toxicities and survival. Fortunately, the toxicity limits of various tissues have been defined, and clinical assays have been developed to monitor those toxicities. For example, hematologic toxicities can be measured through blood sampling. Cardiotoxicity can be assessed through electro- and echocardiography. Thus, the function g can be defined. However, *Tumor*(x), how a tumor responds to treatment plan x, and f, the relationship between survival and tumor behavior, must be defined. If these functions can be defined, a robust literature for optimization problems already exists (109). Thus, the question becomes, "How can we use (for example) the technologies highlighted above to define and parameterize these functions?"

1.5 Next Steps

Medical oncology is in need of a mathematical modeling toolkit that can leverage clinically-available measurements to optimize treatment selection and schedules in the same way radiation oncologists use clinically-available imaging data for treatment planning. Just as the therapeutic choice has been optimized to match tumor genetics, the delivery of those therapeutics can be optimized based on patient-specific PK/PD properties.

Under the current approach to breast cancer therapy, there does not exist an efficient method to consolidate biomarker changes into a holistic understanding of treatment response. While the majority of research on chemotherapy resistance focus on cellular and genetic mechanisms of this resistance, there are numerous patient-specific and tumor-specific measures that contribute to resistance. New approaches that consolidate multimodal information into actionable data are needed. Mathematical modeling offers a solution to this problem. As highlighted above in Section 1.2, mathematical models have already shaped the current approaches to treatment, and mathematical models will continue to push cancer therapy in the era of precision medicine. We emphasize that this approach leveraging a host of patient-specific data is entirely complementary to genetics-based approaches and merits the same attention.

Traditionally, dose and schedules have been optimized to maximize tumor kill rate. There are new theories for the design of chemotherapy. For example, in the adaptive dosing approach, the objective of therapy is to maintain tumor volume (20). In metronomic therapy, the goal of therapy is to normalize tumor vasculature to enhance therapeutic effects (12). The dose schedules needed to realize these approaches will rely on patient-specific PK/PD measurements. By developing the tools to estimate PK/PD parameters, these hypotheses for chemotherapy use may be evaluated more efficiently. Further, it is reasonable to envision improvements in maximum tolerated dosing schemes with patient-specific treatment regimens.

The Cancer Moonshot Initiative (110) highlights the opportunity that exists by adopting screening and treatment plans known to work on a wide-scale basis. There is a need for such implementation science in the development and deployment of cancer therapeutics. While tumor genotype most likely plays an outsized role in determining response, other *measurable* factors such as tumor microenviroment and patient pharmacokinetics also influence response. The extensive characterization of tumor genetics has yielded an arsenal of therapeutics that can more precisely target cancer cells. An equally focused approach to the science of deploying these therapeutics on an optimal schedule is now needed. In the dosing and scheduling domains, we are in a similar position to cancer therapy prior to the advent of genotyping technologies. Advances in clinical chemistry and imaging sciences offer platforms to develop biologically-driven, treatment response models while maintaining the ability to translate those models to a clinical population. These tools will provide the measurements needed to test various dose and scheduling hypotheses. Mathematical models will form the foundation of this approach, and they will hasten the implementation and maximize the benefit of current (and future) therapeutics.

1.6 Thesis proposal

Much work remains to define the models that describe the relationship between delivered therapeutic and subsequent response – both at the tumor and off-target tissues. Specifically, models are needed to describe how changes in clinically-available measurements relate to tumor (and healthy tissue) response to therapy. Revisiting our earlier analogy, what is the $F = ma$ for cancer? We have the means to measure tumor "mass" and "acceleration" (i.e., the multifactorial response of a tumor to therapy). Further, we can measure treatment "force" (i.e., drug pharmacokinetics). A modeling framework that relates these variables would offer the opportunity to adjust and optimize

treatment regimens to maximize response. Clinically, assessment of response is limited to imaging data evaluated *via* RECIST or histopathological evaluation at the time of surgery. Neither of these approaches considers the dynamics of therapy response. Accordingly, the conclusions drawn from single observations are limited. Ideally, the assessment of tumors should integrate the entire history of tumor measurements to draw the most precise insight into tumor behavior. Developing the knowledge basis needed to integrate temporal changes requires a new experimental paradigm – one with an emphasis on time-resolved experiments. Motivated by these fundamental questions, we propose to develop a mechanistic model of treatment response of triple negative breast cancer to doxorubicin therapy. We identify the following Specific Aims to achieve this goal:

Aim 1: Development and validation of an *in vitro* model of doxorubicin treatment response in TNBC. The goal of Aim 1 is to establish a computational model of doxorubicin treatment response in TNBC using *in vitro* data. Tumor response to therapy is dynamic; therapy triggers a cascade of responses that result in temporally downstream changes in tumor status. However, measurements of treatment response are often limited cell survival assays at a single time point following a constant application of therapy (111). In Aim 1, we propose an experimental-mathematical modeling paradigm that incorporates both the dynamics of therapy (pharmacokinetics) as well as the dynamics of cellular response (pharmacodynamics). The proposed model establishes a robust, mechanistic relationship between doxorubicin pharmacokinetics and pharmacodynamics and allows for *prediction* of response to a specified treatment.

Aim 2: Extension of the model to incorporate agents that alter doxorubicin pharmacology. In Aim 2, we leverage the mechanistic PK/PD model to quantify the effects of agents that alter cellular pharmacological properties. Specifically, we investigate the effects of small molecule inhibitors (i.e., sensitizers) that target cellular pharmacokinetics and pharmacodynamics to enhance the response to doxorubicin. We assess treatment response under co-treatment with sensitizing agents and doxorubicin, and we demonstrate the utility of the mechanistic modeling approach which consolidates contributions of pharmacokinetics and pharmacodynamics into a holistic understanding of treatment response. We propose the equivalent dose metric as a means to summarize the effects of combination therapy and serve as a more robust means of comparing treatment response among cell lines. We hypothesize that the proposed modeling framework can be used to identify more effective strategies for dosing and assessing

these sensitizing therapeutics, which have often failed clinically due to toxicity or inactivity despite preclinical promise (112–116).

Aim 3: **Incorporation of cell population heterogeneity into model**. In Aim 3, we leverage the proposed PK/PD model to quantify the effect of cell population heterogeneity on treatment response. Tumors are composed of heterogeneous populations of tumor cells that demonstrate a range of sensitivities to treatment (117). This intratumoral heterogeneity drives the response of tumors to therapy (118), and it has significant consequences in precision medicine approaches which seek to match treatment protocols to biopsy data (119). We study heterogeneity in the context of multi-drug resistant breast cancer in which resistance is mediated through expression of the multi-drug resistant 1 protein (120). We demonstrate that the response of a heterogeneous cell population to doxorubicin is nonlinear, and intercellular pharmacokinetic variability must be considered in analyzing treatment response in heterogeneous cell populations.

Goal: The primary goal of this Dissertation to establish a robust mathematical model of doxorubicin treatment response in an *in vitro* model of triple negative breast cancer. We propose a modular mathematical framework that is easily extended to capture increasing levels of experimental complexity. Finally, we will demonstrate how coupled experimental-mathematical modeling approaches lead to a more precise understanding of treatment response.

1.7 Outline

In this Dissertation, we detail the development of predictive model of treatment response in triple negative breast cancer. This chapter has provided the background and motivation for the work. In Chapter 2, we detail development and validation of the coupled PK/PD model of doxorubicin treatment response proposed in Aim 1. In Chapter 3, the model is extended to incorporate approaches that modulate cellular PK/PD properties to sensitize cells to doxorubicin therapy. In Chapter 4, the model is once again extended to describe treatment response in a heterogeneous cell population. In Chapter 5, we summarize the major findings in this Dissertation and provide recommendations for future model development. Finally, we include an Appendix that details the preliminary data collected to scale the proposed model *in vivo*.

CHAPTER 2

A PREDICTIVE MATHEMATICAL MODELING APPROACH FOR THE STUDY OF DOXORUBICIN TREATMENT IN TRIPLE NEGATIVE BREAST CANCER

2.1 Introduction and Contribution of Study

This chapter focuses on the development of a coupled pharmacodynamics/pharmacokinetic (PK/PD) model that can be leveraged to predict cell population response to doxorubicin therapy. While doxorubicin has been in clinical use for several decades, to our knowledge, measurements of its cellular effects have not previously been coupled to intracellular concentrations and drug exposure times in a predictive framework. Model development was achieved through a data-driven approach, leveraging several cell lines. A biophysical model was constructed to describe the collected data, and predictions were possible by the effective description of treatment conditions by the PK model.

These studies address a fundamental limitation in the current understanding of the pharmacokinetic and pharmacodynamic properties of cytotoxic agents. While the potency, efficacy, and mechanism of action of these agents have been the target of study for years, these pharmacologic properties are inherently insufficient to predict the spatiotemporal response of individual tumors to treatment, limiting the ability to realize a host of theoretical dosing schedules. We show here that a combined PK/PD modeling approach allows for prediction of the *in vitro* response of a panel of TNBC cell lines to doxorubicin therapy. This work enables cell-line specific model parameters to be estimated from experimental data, revealing phenotypic heterogeneity in PK/PD properties not previously quantified. Further, the PD properties were found to vary as a function of $C_{B,max}$ and AUC, summary statistics of doxorubicin PK. More generally, this work provides a template for studies quantitatively investigating treatment response and a scalable approach toward predictions of tumor response *in vivo*. This work was published in *Scientific Reports* in July, 2017, and text in this chapter is adapted from:

Matthew T. McKenna, Jared A. Weis, Stephanie L. Barnes, Darren R. Tyson, Michael I. Miga, Vito Quaranta, Thomas E. Yankeelov. "A Mathematical Modeling Approach for Predicting the Response of Triple Negative Breast Cancer to Doxorubicin." Scientific Reports (2017).

2.2 Abstract

Doxorubicin forms the basis of chemotherapy regimens for several malignancies, including triple negative breast cancer (TNBC). Here, we present a coupled experimental/modeling approach to establish an *in vitro* pharmacokinetic/pharmacodynamic model to describe how the concentration and duration of doxorubicin therapy shape subsequent cell population dynamics. This work features a series of longitudinal fluorescence microscopy experiments that characterize 1) doxorubicin uptake dynamics in a panel of TNBC cell lines, and 2) cell population response to doxorubicin over 30 days. We propose a treatment response model, fully parameterized with experimental imaging data, to describe doxorubicin uptake and predict subsequent population dynamics. We found that a three compartment model can describe doxorubicin pharmacokinetics, and pharmacokinetic parameters vary significantly among the cell lines investigated. The proposed model effectively captures population dynamics and translates well to a predictive framework. In a representative cell line (SUM-149PT) treated for 12 hours with doxorubicin, the mean percent errors of the best-fit and predicted models were 14% ($\pm$10%) and 16% ($\pm$12%), which are notable considering these statistics represent errors over 30 days following treatment. More generally, this work provides both a template for studies quantitatively investigating treatment response and a scalable approach toward predictions of tumor response *in vivo*.

2.3 Introduction

When cytotoxic therapy was first applied to cancer, few principles existed to guide its use (121). Skipper provided a framework through the formulation of the log-kill hypothesis, postulating that a given dose of chemotherapy would kill a fixed fraction of tumor cells regardless of tumor size (33). Based on this framework, a systemic chemotherapy paradigm was established, in which cytotoxic agents were administered several times, even after disease could no longer be detected. Following this, investigators sought to improve response through dose escalation, but their efforts were met with limited improvement in tumor response (36,37). Dosing paradigms were updated after Norton and colleagues hypothesized that tumor kill is proportional to tumor growth rate (39). This led to development of dose-dense schedules, which decrease the time between doses to target smaller, faster-growing tumors. These dose-dense schedules resulted in a significant improvement over previous treatment protocols (122) and remain the standard-of-care

for triple negative breast cancer (TNBC) treatment. In recent years, several theoretical models have been developed to further refine treatment regimens (80). Of note, Gatenby and colleagues proposed an adaptive model which adjusts doses based on tumor volume changes (20,123). Metronomic dosing schedules advocate smaller, more frequent dosing (12,124). These new dosing approaches are predicated on both the timing of therapy administration and response evaluation (125) but have revealed a fundamental limitation in the current understanding of the pharmacokinetic (PK) and pharmacodynamic (PD) properties of cytotoxic agents. While the potency, efficacy, and mechanism of action of these agents have been the target of study for years, these pharmacologic properties are inherently insufficient to predict the spatiotemporal response of individual tumors to treatment, limiting the ability to realize these theoretical dosing schedules.

In this contribution, we propose a scalable experimental/modeling framework that incorporates the dynamics of therapy and response. In this way, we hope to complement theoretical dosing models with a precise approach to scale *in vitro* observations to *in vivo* experiments. The utility of this framework is demonstrated in the context of doxorubicin treatment in TNBC. Doxorubicin is a standard-of-care, DNA-damaging agent used in the treatment of a host of malignancies, including TNBC (126–128). As we review below, the current approaches to the study of doxorubicin are insufficient to generate temporally-resolved predictions of TNBC response to time-varying doxorubicin treatments.

Cellular response to a given therapeutic is often evaluated by one of a variety of *in vitro* assays and generally interpreted using dose-response curves. In these assays, drug is typically applied to a cell population over a wide range of concentrations. Following a predefined treatment time (usually 72 hours) drug effect is quantified with one of many end-point assays that measure the number of viable cells (often indirectly). These data are then analyzed with the Hill equation, a sigmoidal function that is used to describe the relationship between drug concentration and drug effect (129). The Hill equation contains a number of free parameters including: the maximal drug effect (E_{max}), the concentration of drug that yields a half-maximal effect (EC_{50}), the effect in the absence of drug (E_0), and the Hill coefficient (h), which describes the slope of the dose response curve. The parameters that result from the best fit of the model to the dose-response curves are specific to each cell line, and those data are used to guide drug dosing for subsequent *in vivo* experiments. While this approach has great merit in evaluating drug efficacy and identifying new therapeutics, it necessarily overlooks the importance of the relative timing of treatments and

response measurement. Further, slight changes in experimental duration or growth conditions have been shown to significantly impact estimation of model parameters (130,131). Even proposed metrics that analyze population rates of change to correct for varying cell line behaviors and experimental protocols assume a constant population rate of change following application of therapy (130,131). Consequently, the predictive potential of such approaches is fundamentally limited, particularly in the setting of cytotoxic agent use *in vivo*, in which agents are applied as impulses and resilient populations, which demonstrate temporally-varying population growth rates following therapy, are often observed.

Relative to the efficacy studies above, the temporal relationship between cytotoxic treatment and its effects has received little attention. Eichholtz-Wirth and colleagues first demonstrated the dependence of cell survival on doxorubicin exposure time, deriving an empirical relationship between surviving fraction of cells (*SF*), drug concentration (*c*), and length of exposure (*t*), through a sensitivity constant (*k*): $SF = e^{-ktc}$ (132). Others have proposed modifications to the classic Hill function to incorporate drug exposure times (133,134). To resolve the temporal dynamics of the cellular response to therapy, Lobo and Balthazar proposed a transit compartment model to describe the relationship between drug application and the time lag until drug effects were realized (135). These models were all built utilizing end-point assays evaluating the percent survival following various exposure times. Lankelma employed a host of clonogenic assays following treatment with various concentrations of doxorubicin for multiple exposure times (136,137). They quantified cell population size over time and constructed a model relating treatment parameters to these cell population dynamics. However, a model of therapy response that incorporates both the dynamics of therapy (pharmacokinetics) as well as the dynamics of cellular response (pharmacodynamics) has remained elusive. Such modeling would represent a critical advance, as it would allow more precise measurements of response and customization of treatment protocols following estimation of PK parameters.

This work focuses on the construction of a mathematical model to predict TNBC cell population dynamics in response to time-varying doxorubicin treatments. The approach outlined below incorporates a series of experiments in a panel of four TNBC cell lines designed to measure both the *in vitro* pharmacokinetics (PK) and pharmacodynamics (PD) of doxorubicin therapy. The PK/PD parameters are quantified through time-resolved fluorescent microscopy, and these data are used to drive the development of a treatment response model. This approach yields a

mathematical model of doxorubicin therapy with distinct parameter value sets for each TNBC cell line. This model can generate hypotheses that are directly testable in both the *in vitro* and *in vivo* settings. Thus, the objectives of this contribution are to: 1) establish a model that describes *in vitro* doxorubicin pharmacokinetics, 2) establish a model relating treatment variables (concentration and duration) to subsequent cell population dynamics, and 3) propose a prediction scheme leveraging doxorubicin pharmacokinetic and pharmacodynamic data to predict response to various doxorubicin treatments (Figure 2.1).

2.4 Materials and Methods

2.4.1 Cell culture

TNBC is a subgroup of invasive cancers that lack significant expression of the estrogen receptor, progesterone receptor, and human epidermal growth factor receptor 2 (138). Lacking specific receptor targets, the current approach to adjuvant and neoadjuvant therapy (NAT) for locally advanced TNBC utilizes a combination of cytotoxic drugs with a particular emphasis on doxorubicin, cyclophosphamide, and docetaxel (126–128). Lehmann and colleagues identified six subtypes of TNBC: two basal-like subtypes, an immunomodulatory subtype, a mesenchymal subtype, a mesenchymal stem cell-like subtype, and a luminal subtype expressing androgen receptor (96,139). One cell line from four of these groups was selected for the current studies: MDA-MB-468 (basal-like 1), SUM-149PT (basal-like 2), MDA-MB-231 (mesenchymal), and MDA-MB-453 (luminal expressing androgen receptor). In selecting cell lines in this way, the proposed model of doxorubicin response can be assessed across a heterogeneous spectrum of TNBC cell lines.

All cell lines were obtained through American Type Culture Collection (ATCC, http://www.atcc.org) and maintained in culture according to ATCC recommendations. All cell lines were tested for mycoplasma after thawing using a PCR-based method (MycoAlert, Lonza, Allendale, NJ), and any positive cultures were immediately discarded. To facilitate automated image analysis for identifying and quantifying individual nuclei in the time-lapsed fluorescent microscopy experiments (described below), each of the four cell lines was modified to express a histone H2B conjugated to monomeric red fluorescent protein (H2BmRFP; Addgene Plasmid 18982) as previously described (130,140,141). Briefly, this plasmid was transduced into each cell line with replication-incompetent lentiviral particles. Following transduction, each cell line was

Figure 2.1: Overview of cell-line specific modeling framework for doxorubicin treatment response prediction. A series of time-resolved fluorescence microscopy experiments were performed to quantify both the uptake of doxorubicin into TNBC cell lines (a) as well as the response of those cell lines to various doxorubicin treatments (b). Data from these experiments were used to fit the model (i.e., Eqs. (2.1) - (2.5)) of treatment response in TNBC (c). After training the model on observed data, the model can be initialized with a cell count and a prescribed treatment timecourse to predict cell population dynamics following the proposed treatment (d). These predictions can then be compared to experimental results.
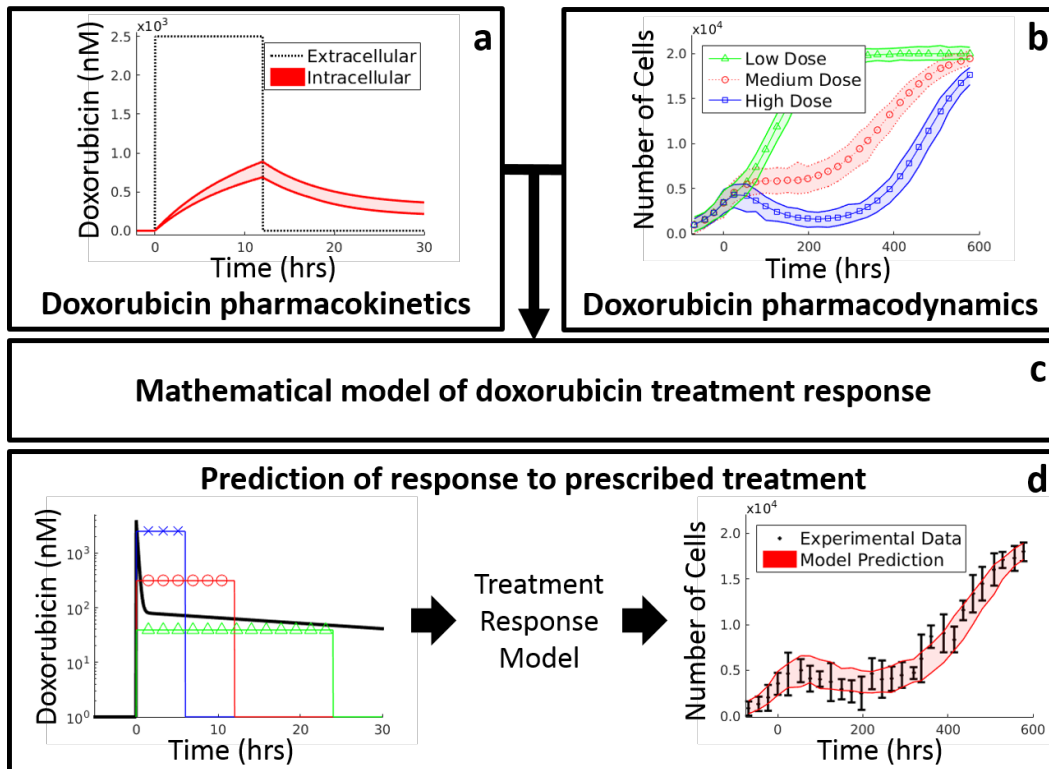
sorted via flow cytometry by label intensity to collect the brightest 20% of the respective cell populations. Modified cells were grown in the same manner as their respective parental strains. Cell lines were passaged no more than 30 times before being discarded.

2.4.2 Doxorubicin Imaging and Image processing

Time resolved fluorescent microscopy was employed to characterize the uptake of doxorubicin by each cell line. Doxorubicin is naturally fluorescent with excitation and emission peaks near 470 nm and 570 nm, respectively (142). The intrinsic fluorescence of doxorubicin was leveraged to quantify the movement of doxorubicin from the extracellular space into cells. Each parental cell line was introduced into 96-well microtiter plates at ~10,000 cells per well. Each well was imaged at ~15 minute intervals *via* brightfield and fluorescent microscopy with a 20× objective in 2×2 image montages on a BD Pathway 855 Bioimager (BD Biosciences, San Jose, CA). Imaging began one hour prior to application of doxorubicin and continued for approximately 24 hours following doxorubicin application. An 8-fold range of doxorubicin concentrations, from 2500 nM to 312 nM, were applied to cells using a two-fold dilution series. After 6 or 12 hours, drug was removed *via* media replacement. Each of the ten conditions (i.e., four concentrations plus a control each at two exposure times) were collected in duplicate. These treatment conditions were designed to approximate drug exposure of human tumors *in vivo* as measured by the area under the doxorubicin concentration-time curve (a range of 1875 to 30000 nM·hr was used experimentally to approximate the 4427±418 nM·hr observed *in vivo* (143)) and peak doxorubicin concentration (312 to 2500 nM experimentally to approximate the 1000 to 5000 nM observed *in vivo* (143)).

Digital images were segmented into extracellular and intracellular compartments through a hybrid, semi-automated process. Prior to doxorubicin application, segmentation was performed exclusively on the brightfield images to identify cell boundaries. For each cell line, a single cell image was manually cropped, and the normalized cross-correlation was calculated between that cell and the entire image. Local maxima of the cross correlation were used to identify cells. The images were then manually reviewed to remove any false positives and to ensure all cells were identified. The initial cell segmentation mask, which consisted of circles centered on each cell identified *via* cross-correlation, were refined through an active contour model (Figure 2.2b).

Following application of doxorubicin, segmentation was performed on the fluorescent images with a threshold-based approach. Briefly, the background was subtracted by taking the difference between the image and a cell-free well with the same doxorubicin concentration. An adaptive histogram approach was used to enhance the contrast of this difference image, and the image was finally de-noised with a Wiener filter. The threshold was automatically selected for each image with Otsu's method, and this threshold was applied to generate the segmentation mask. The mask was refined using an active contour model (Figure 2.2c). Finally, the mask was overlaid on brightfield images, and the segmentation result was manually reviewed.

2.4.3 Doxorubicin Compartment Modeling

A three compartment model was employed to describe the uptake and binding of doxorubicin in cancer cells. Briefly, doxorubicin is thought to enter cells *via* diffusion, possibly through a saturable carrier-mediated process (144,145). Once in the cell, doxorubicin is translocated to the nucleus where it intercalates DNA and stabilizes the topoisomerase II complex (146,147). Doxorubicin may also be actively effluxed from the cell *via* p-glycoprotein (148). This process is modeled *via* mass conservation in Eqs. (2.1) - (2.3):

$$\frac{dC_E(t)}{dt} = k_{FE}\frac{v_I}{v_E}C_F(t) - k_{EF}C_E(t) \tag{2.1}$$

$$\frac{dC_F(t)}{dt} = k_{EF}\frac{v_E}{v_I}C_E(t) - k_{FE}C_F(t) - k_{FB}C_F(t) \tag{2.2}$$

$$\frac{dC_B(t)}{dt} = k_{FB}C_F(t) \tag{2.3}$$

where $C_E(t)$, $C_F(t)$, and $C_B(t)$ are the concentrations of doxorubicin in the extracellular, free, and bound compartments, respectively, at time t. Both the free and bound compartments were defined to share the same physical space (intracellular). The free compartment represents drug that has diffused into the cell, while the bound compartment represents drug that has bound to the DNA. The k_{ij} parameters are rate constants that describe the movement of doxorubicin between each of these compartments; for example, k_{FE} describes the rate of drug transfer from the free, intracellular compartment to the extracellular compartment. Similar definitions apply to k_{EF} and k_{FB}. The volumes of the intracellular and extracellular compartments are denoted with v_I and v_E, respectively. The model is illustrated in Figure 2.2a. Of note, each cell line is assumed to have a

single set of compartment model parameters (i.e., k_{EF}, k_{FE}, and k_{FB}), and those parameters are assumed to be independent of drug concentration and drug exposure time. Further, to simplify the model, saturation kinetics for doxorubicin transport are not explicitly included.

The extracellular and intracellular compartments were defined from the cell segmentation. To create fluorescent intensity timecourses for the intracellular and extracellular compartments, fluorescence signal was averaged within the respective (segmented) compartments on each image. These two intensity timecourses (extracellular and intracellular) were converted to concentration, as doxorubicin concentration is proportional to observed fluorescence intensity (Figure 2.2d). The volume of the extracellular compartment, $\underline{v_E}$, was set to 250 µL, the volume of media in each well. The intracellular volume, v_I, was estimated by multiplying the number of cells seeded (10,000) by an estimate of cell volume (an ellipsoid model was fit to cell segmentation results).

A nonlinear least squares approach implemented in MATLAB (Natick, MA) was used to fit Eqs. (2.1) - (2.3) to the concentration timecourses for each treatment condition to generate estimates for k_{EF}, k_{FE}, and k_{FB}. Note that the extracellular compartment was treated as a well-defined, experimentally-controlled input function and was not fit by the model. For example, to generate the extracellular compartment timecourse illustrated in Figure 2.2e, a bolus of doxorubicin was added to the experimental well $t = 0$ hours. At $t = 6$ hours, the drug was removed *via* media replacement; i.e., all drug-containing media is removed from the well, and fresh, drug-free media was added. This input function was used to perturb the system to measure the underlying cell line-specific compartment model parameters. As model parameters were assumed to be invariant of doxorubicin concentration and exposure time, all treatment conditions were fit simultaneously to yield a single estimate of k_{EF}, k_{FE}, and k_{FB} for each cell line. The area under the doxorubicin curve in the extracellular compartment ($AUC_{c,t}$) was introduced to the objective function, $G(x)$, to normalize for treatment conditions as follows:

$$\min_{x} G(x) = \sum_{c=c_i}^{c_f} \left(\sum_{t=t_i}^{t_f} \frac{\left(Y_{t,c} - \hat{Y}_{t,c}(x)\right)^2}{AUC_{c,t}} \right),$$

where x is the set of parameters, $Y_{t,c}$ is the measured concentration at time t and concentration c, $\hat{Y}_{t,c}(x)$ is the model-estimated concentration at time t and concentration c when the model is evaluated with parameters x, c_i and c_f are the minimum and maximum drug concentrations respectively, and t_i and t_f are the initial and final timepoints, respectively. Without AUC

Figure 2.2: Overview of doxorubicin compartment modeling. Doxorubicin pharmacokinetics is described with a three compartment model, illustrated in (a) and described by Eqs. (2.1) - (2.3). To parameterize this model, each cell line is serially imaged *via* brightfield (b) and fluorescent microscopy (c) to monitor doxorubicin concentration over time. Images are separated into extracellular and intracellular (red overlay) compartments. As fluorescence intensity is proportional to doxorubicin concentration (d), the image intensities are converted into concentration, and extracellular and intracellular concentration timecourses are extracted from these images (e). Finally, the model is fit to these timecourses (e), and the model fit with 95% confidence interval are overlaid on the data. Experimentally-derived model parameter values with 95% CIs are reported for each TNBC cell line investigated (f-h).
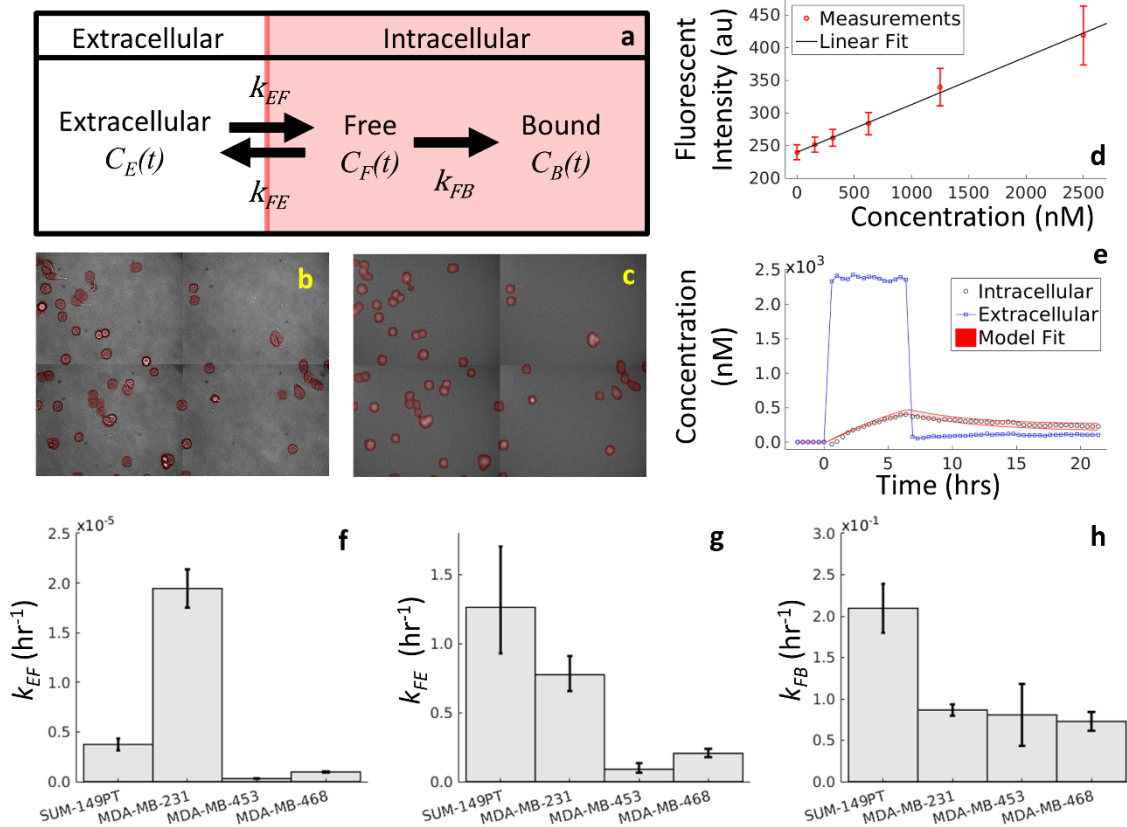
normalization, the residuals at high concentrations and exposure times would drive model fits at the expense of lower concentrations and exposure times. The compartment modeling approach is outlined in Figure 2.2.

Of note, three compartment models of varying complexity were initially proposed to describe doxorubicin pharmacokinetics. Model selection was performed using the Akaike information criterion, which is a measure of model likelihood that balances goodness of fit with the number of free parameters (149).

2.4.4 Treatment Response Monitoring

Each H2B-labeled TNBC cell line was added to 96-well microtiter plates at ~2,500 cells per well. Cells were grown for at least three days to allow for a pre-treatment proliferation rate to be estimated. Doxorubicin was then introduced at concentrations ranging from 2500 to 10 nM with a two-fold dilution series and subsequently removed *via* media replacement after 6, 12, or 24 hours (areas under doxorubicin concentration-time curve ranging from 60 to 60000 nM·hr). These experimental conditions were designed such that the areas under the doxorubicin curves overlapped those observed *in vivo* (143). These cells were imaged daily *via* fluorescent microscopy for at least 30 days following application of doxorubicin. For these treatment response studies, fluorescence microscopy images were collected using a Synentec Cellavista High End platform (SynenTec Bio Services, Münster, Germany) with a 20× objective and tiling of 21 images. Exposure times with 570 nm light were optimized for each cell line to account for varying label strength and ranged from 600-650 ms. Nuclei were segmented and counted in ImageJ (http://imagej.nih.gov/ij/) using a previously-described method (150) to quantify cell population. Six replicates of each of the 30 treatment conditions (nine concentrations plus a control for each drug exposure time) were collected for each cell line. Media was refreshed every 3 days for the duration of each experiment to ensure sufficient growth conditions for surviving cells.

2.4.5 Treatment Response Model

Doxorubicin canonically induces DNA damage by intercalating DNA bases, stabilizing the topoisomerase II complex, and inducing DNA damage *via* free radical formation (147). At high doses (here, dose is defined as a summary statistic of a treatment condition, consolidating drug concentration and drug exposure time, and is denoted *D*), extensive DNA damage often results in

cell death *via* apoptosis. Low to moderate doses of doxorubicin induce cell senescence, and cell death occurs primarily *via* mitotic catastrophe (151,152). Whereas apoptosis is immediate (on the order of hours to days), mitotic catastrophe is a relatively protracted process (on the order of several days). This is likely due to the fact that cells must progress through the cell cycle to reach mitosis for this mode of death to occur, and doxorubicin is known to cause cell cycle arrest. These processes were modeled by a logistic growth model, Eq. (2.4), modified by either one of two time-dependent response functions, Eqs. (2.5) and (2.6), reflecting the distinct forms of cell death, as follows:

$$\frac{dN_{TC}(t)}{dt} = \left(k_p - k_d(t, D)\right) N_{TC}(t) \left(1 - \frac{N_{TC}(t)}{\theta(D)}\right) \tag{2.4}$$

$$k_d(t, D) = \begin{cases} 0 & t < 0 \\ k_{d,A}(D) & t \geq 0 \end{cases} \tag{2.5}$$

$$k_d(t, D) = \begin{cases} 0 & t < 0 \\ k_{d,B}(D) r(D) t e^{1 - r(D)t} & t \geq 0 \end{cases}, \tag{2.6}$$

where k_p and k_d are the proliferation and dose-specific death rates, respectively, r is a dose-specific constant describing the rate at which treatment induces an effect, θ is the dose-specific carrying capacity describing the maximum number of cells that can be supported by the experimental system, and $N_{TC}(t)$ is the number of tumor cells at time t. Prior to treatment (i.e., $t < 0$), cells are modeled to have a constant proliferation rate, k_p. Following treatment at $t = 0$, Eq. (2.5), assumed an immediate transition from the pre-treatment growth rate to a stable, post-treatment rate. Eq. (2.6), allowed for a smooth induction of drug effect following treatment, while ultimately allowing for recovery of the cell population. A weighted averaging approach, detailed below, was used to incorporate both Eqs. (2.5) and (2.6) in the treatment response model. Cell populations are assumed to be homogeneous in that the average behavior of the population is used to describe population dynamics. Of note, an analytic solution of Eqs. (2.4) – (2.5) was derived to improve computational speed.

For each cell line, Eq. (2.4) was first fit to pre-treatment and untreated control data, yielding a single, cell-line specific estimate for the proliferation rate, k_p, and carrying capacity, θ. Fixing k_p for each cell line, the treatment response models, Eqs. (2.5) and (2.6), were then fit to the post-treatment data. For each cell line, all data from a single doxorubicin exposure time experiment

were considered simultaneously in the parameter optimization. Separate parameter estimates were made for each doxorubicin concentration in each exposure time dataset. Specifically, parameter estimates and the corresponding 95% confidence intervals were obtained for $k_{d,A}$ and θ in Eq. (2.5), and $k_{d,B}$, r, and θ in Eq. (2.6) from the post-treatment cell counts. To perform this estimation, a nonlinear least squares approach was implemented in MATLAB, utilizing the trust-region reflective algorithm. Notably, in fitting each model, a regularization term was introduced to the objective function, $G(x)$, to penalize non-smooth variation in parameter values with respect to treatment conditions as follows:

$$\min_{x} G(x) = \sum_{c=c_i}^{c_f} \left(\sum_{t=t_i}^{t_f} \left(\frac{Y_{t,c} - \hat{Y}_{t,c}(x)}{Y_{t,c}} \right)^2 + \alpha D_c(x)^2 \right),$$

where x is the set of parameters, $Y_{t,c}$ is the measured cell counts at time t and concentration c, $\hat{Y}_{t,c}(x)$ is the model-estimated cell counts at time t and concentration c when the model is evaluated with parameters x, c_i and c_f are the minimum and maximum drug concentrations respectively, t_i and t_f are the initial and final timepoints respectively, and α is an empirically-determined positive constant that weights the contribution of the regularization term, $D_c(x)$, which is a first derivative operator that estimates the local derivative of the parameters with respect to treatment condition (as described below). The regularization term provides structure to parameter estimates that are otherwise unable to be resolved with the treatment response data. In turn, the regularization term improves performance of the local regression approach used for predictions in Section 2.4.6, which is sensitive to local variance in parameter estimates.

The model was initialized with the cell count at the timepoint following treatment for each individual replicate, and all subsequent timepoints were considered in the model fit. To avoid local minima, the fitting process was initialized with 50 sets of parameter estimates selected randomly from expected distributions for each parameter. k_d values were initialized by sampling a uniform distribution from $[-2k_p, 5k_p]$. r was bounded within $[0.001, 0.05]$ hr^{-1}. These bounds correspond to observing the maximal death rate at 1000 and 20 hours respectively, reflecting the duration of the experiment (~700 hours) and the sampling rate (24 hours). The experiments, as constructed, are unable to resolve estimates beyond these boundaries. Further, θ was bounded between $[0.7\theta, 1.3\theta]$, where θ is the carrying capacity observed in the control data for each cell line. Notably, θ cannot

be resolved at high doses that induced population regression. In these cases, in which population size is much lower than θ, the logistic growth term has little influence on model behavior.

A cross-validation approach was used to tune the regularization parameter α. For each cell line, the other three cell lines were used as a training set to determine α for the held-out cell line. Each model (i.e., Eqs. (2.5) – (2.6)) was fit to each cell line in the training set using α values uniformly sampled from 0 to 10. The prediction scheme outlined in Section 2.4.6 was then run for each cell line. The α value yielding the best predictions as measured by mean percent error across the cell lines in the training set, were used in fitting the held-out cell line.

The maximum bound concentration of doxorubicin ($C_{B,max}$) and the area under the curve of the extracellular concentration timecourse (AUC) were both used to summarize each treatment condition (D in Eqs. (2.4) - (2.5)) (147). We hypothesized that the $C_{B,max}$ metric would sufficiently describe both the topoisomerase-II mechanism of doxorubicin as well as doxorubicin's free-radical mechanism, due to redox cycling of doxorubicin that persists within cells (153). To calculate $C_{B,max}$, the compartment model (i.e., Eqs. (2.1) - (2.3)) was populated by cell-line-specific parameters and run forward in time using the specified extracellular concentration timecourse for each treatment condition. $C_{B,max}$ was defined to be the maximal concentration in the bound compartment during the model evaluation. As doxorubicin is hypothesized to also have an extracellular effect (134,154), the AUC was also used as a descriptor of treatment condition. AUC was defined as the integral of the extracellular concentration timecourse with respect to time (simply (doxorubicin concentration) × (exposure time) in the pulsed treatments used in this study). To generate a single best-fit model, a weighted averaging approach was employed. Model weights were calculated from the Akaike information criterion (AIC) for each $k_d(t)$ model (i.e., Eqs. (2.5) and (2.6)) (149). The AIC for model i can be calculated with the following equation:

$$AIC_i = n \ln \frac{RSS}{n} + 2p \ ,$$

where n is the number of data samples, RSS is the residual sum of squares of the fit-optimized model, and p is the number of model parameters. The normalized probability of model i being the best model, w_i, among all proposed models can then be calculated:

$$w_i = \frac{e^{-\frac{1}{2}\Delta_i}}{\sum\limits_{j=1}^{R} e^{-\frac{1}{2}\Delta_j}} \ ,$$

where Δ_i is the difference in AIC values between model i and the model with the minimal AIC value and R is the total number of models(155,156). The best-fit model, $N_{TC}(t)$, can then be calculated by weighting Eqs. (2.4) - (2.5) as follows:

$$N_{TC}(t) = w_A N_{TC,A}(t) + w_B N_{TC,B}(t) \ ,$$

where $N_{TC,A}(t)$ and $N_{TC,B}(t)$ are the solutions to Eq. (2.4) populated with Eqs. (2.5) and (2.6) respectively, and w_A and w_B are the respective weights for those models.

Confidence intervals on the best-fit timecourses were constructed through a bootstrap approach. The six replicates for each treatment condition were resampled with replacement, and the fitting process described above was used to generate timecourses for each resampled dataset. This resampling was repeated 500 times, and the 95% confidence intervals on these fits were recorded.

This fitting approach was validated on a synthetic dataset to ensure that parameter estimation routines successfully returned true model values. The dataset was constructed through forward evaluations of the proposed models with five levels of additive noise drawn from a normal distribution with a standard deviations of 0%, 5%, 10%, 15%, and 20% of the simulated cell count. Notably, the cell counting technique employed in this work has been shown to be highly accurate; when compared to manual counting, the automated counts are highly correlated ($R^2 = 0.99$) (150). 22,500 simulations were run under each noise condition, and the model was fit to each simulated dataset.

To determine the effect of parameter variance on model behavior, the sensitivity of model predictions at the end of the experiment to each parameter was measured using the extended Fourier Amplitude Sensitivity Test (157). The total-order sensitivity index, S_{TI}, is reported. This metric is scaled from 0 to 1 and represents the fraction of model output variance that can be apportioned to variance in the parameter under investigation.

2.4.6 Prediction of Treatment Response

The proposed model, as constructed, can accommodate a range of treatment times and concentrations. While this model is intended as a more general predictive framework, to demonstrate the utility of the modeling approach, the ability of the model to predict population changes following treatment at new concentrations and exposure times was evaluated. In this

Figure 2.3: Prediction approach. Model parameters ($k_{d,A}$, θ in Eq. (2.5) and $k_{d,B}$, r, θ in Eq. (2.6)) were fit to each treatment condition in the training set (a, red X's). These parameter fits were then described by a local regression model (a, black line) to generate parameter estimates for treatments in the test set (a, blue O's). Model weights from the training set (b, red x's) were described by a logistic model (b, black line) to generated weights for the test set (b, blue circles). Final predictions represent a weighted average of each model, and a bootstrap analysis was used to generate a 95% confidence interval for these predictions (red overlay in c).

a) Local regression to generate parameter estimates

b) Logistic regression to estimate model weights

c) Weighted average of models to generate prediction
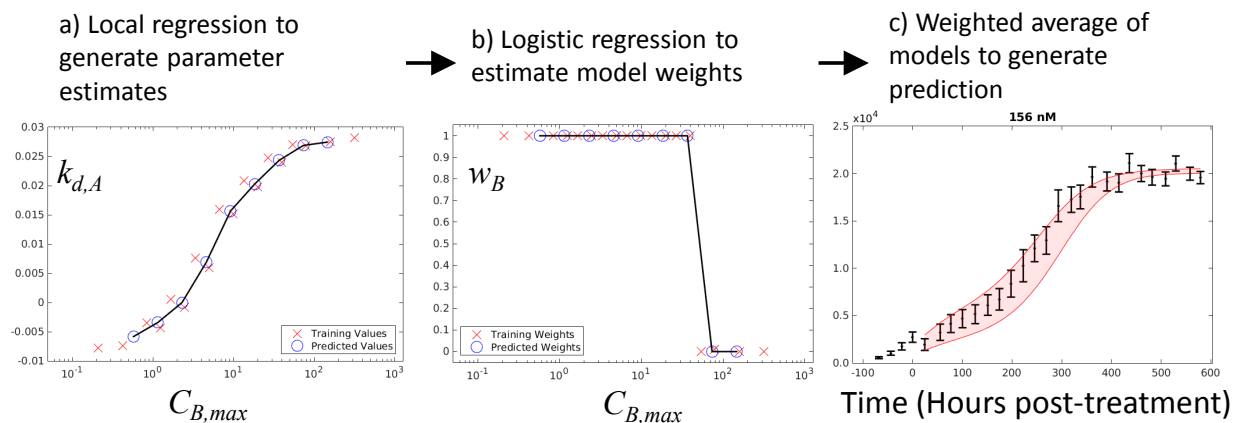
example, data from a single exposure time (12 hours; i.e., the 'training set') is used to train the model (i.e., Eqs. (2.4) – (2.5)) to predict cell counts following treatments for 6 and 24 hours (i.e., the 'test set'). This analysis was repeated using each exposure time dataset as a training set (e.g., 6-hour dataset used to predict cell counts following 12- and 24-hour treatments).

Model parameters and weights first were fit to the treatment response data in the training set as described in Section 2.4.5. Next, each treatment condition in the test set was described by its $C_{B,max}$ and AUC values. As these values in the test set may not overlap exactly with those values in the training data, localized linear regression models were used to interpolate parameter space to generate parameter estimates at the specified $C_{B,max}$ and AUC values (158). This approach fits a linear model to training data near the $C_{B,max}$ and AUC of interest. Model weights (i.e., w_A and w_B) for the test set then were estimated through a binomial logistic model. This logistic function was trained to define the relationship between estimated model weights in the training set and the corresponding $C_{B,max}$, AUC, and model parameter values. Finally, models were initialized with the first post-treatment measurements in the test set and run forward using the estimated parameter values to produce cell count predictions. This approach is outlined in Figure 2.3.

The mean percent error across all timepoints and mean percent error at the end of the experiment are reported for the predicted models and corresponding best fit models. Confidence intervals on the predicted timecourses were constructed through a bootstrap analysis in which the six replicates for each treatment condition in the training set were resampled with replacement. This resampled training set was used to generate predictions. The resampling procedure was repeated 500 times, and the 95% confidence intervals on these predictions were computed.

2.5 Results

2.5.1 Doxorubicin uptake

The three models initially proposed to describe doxorubicin PK are illustrated in Figure 2.4. The model used in this work (Figure 2.4b, Eqs. (2.1) – (2.3)) was selected because, relative to the other models, it best balanced model parameter parsimony with goodness of fit as measured by the AIC (i.e., it was found to have the smallest AIC value among evaluated models).

A three compartment model was sufficient to describe doxorubicin uptake in all cell lines. The mean percent errors of the model fit across all treatment conditions were 31.8%, 34.6%, 23.5%, and 26.8% for the SUM-149PT, MDA-MB-231, MDA-MB-453, and MDA-MB-468 cell

Figure 2.4: Compartment model selection. Each of the models (a-c) were fit to the concentration timecourses as described in Section 2.4.3. The Akaike information criterion (AIC) was calculated for each of the models. The AIC is a measure of model likelihood that balances goodness of fit with the number of free parameters. Smaller AIC values indicate a more likely model. Model b is more likely than Model a for all cell lines (d). Model c results in a marginal improvement on Model b in two of the cell lines. Model b was selected to describe doxorubicin pharmacokinetics.
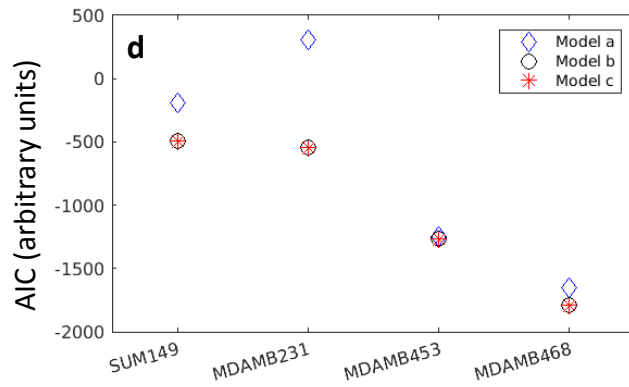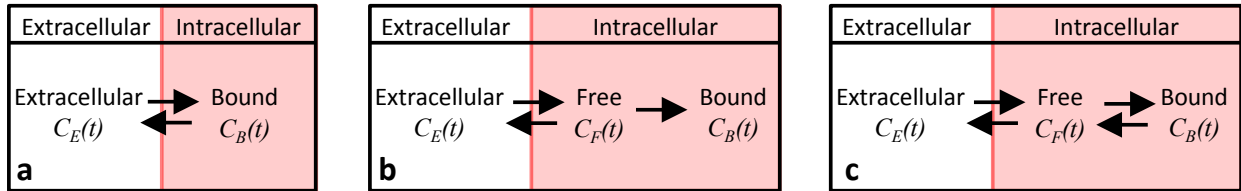
Figure 2.5: Residuals from compartment model fit. The doxorubicin concentration timecourses are fit to Eqs. (2.1) – (2.3) as described Section 2.4.3. Residuals, normalized by the area under the doxorubicin curve in the extracellular compartment (AUC), are shown below. Each column corresponds to an individual cell line and each row to a given drug concentration. The red and black points represent residuals from the 6-hour and 12-hour exposure time datasets, respectively. While no significant violations of model assumptions are seen, it is difficult to rigorously test the assumption that parameters are independent of concentration and exposure time in the current dataset, which only contains four doxorubicin concentrations and two exposure times. Notably, higher errors are observed at low doxorubicin concentrations and low exposure times. In these cases, the low concentrations of doxorubicin in the intracellular compartment result in a low signal to noise ratio of the measurements.
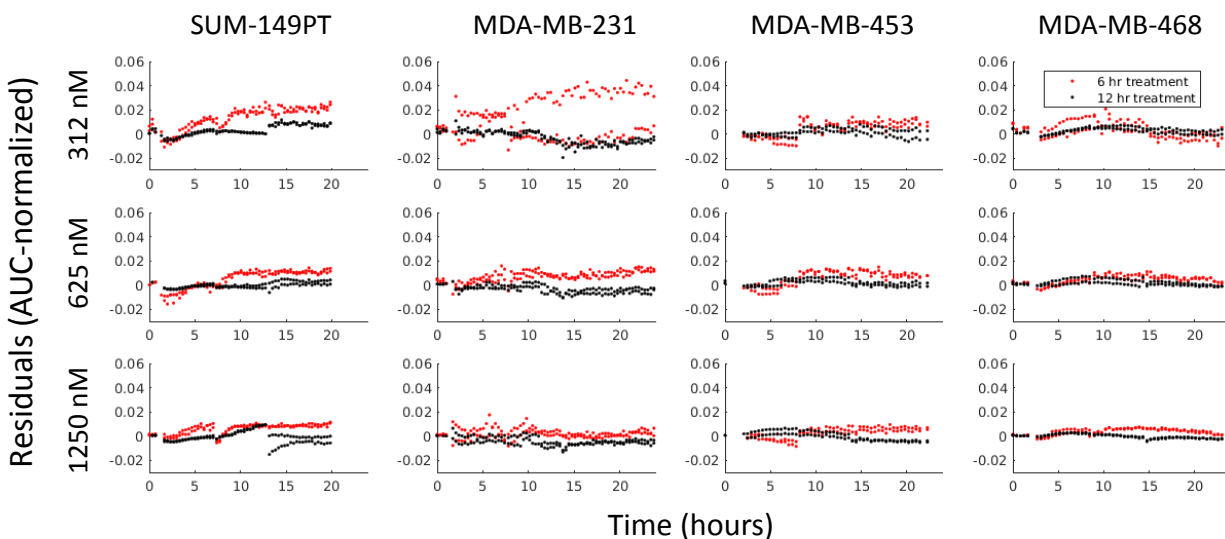
lines, respectively. Model residuals are shown in Figure 2.5. A sample doxorubicin uptake curve is displayed in Figure 2.2e along with compartment model parameter fits for each cell line with 95% confidence intervals. Significant differences were observed when comparing parameter fits from different cell lines. For example, k_{EF} is significantly greater in the MDA-MB-231 line than in the MDA-MB-468 line, indicating that doxorubicin diffuses more quickly into MDA-MB-231 cells ($p < 0.05$).

2.5.2 Validation of Optimization Routine

The optimization routine described in Section 2.4.5 was used to recover parameter estimates from simulated data. As illustrated in Figures 2.6 and 2.7, the optimization routine was able to return accurate estimates of $k_{d,A}$, $k_{d,B}$, and r. Of note, high variance in parameter estimates was observed as values of r approached 0.05 hr^{-1} and values of $k_{d,B}$ approached 0 hr^{-1}. There exists intrinsic uncertainty at this limit as those rapid dynamics coupled with small $k_{d,B}$ effects cannot be resolved by the current data.

2.5.3 Sensitivity Analysis

The eFAST was implemented to study the effect of model parameters on model predictions. The sensitivity of model predictions to parameter variations was evaluated at 1, 2, and 4 weeks post-treatment and quantified by S_{TI}. S_{TI} is reported in Figure 2.8. The proliferation rate, k_p, is the most sensitive parameter over the early timepoints. Additionally, model behavior is insensitive to θ at early timepoints and high $k_{d,B}$ values as the cells counts in these conditions are much lower than the carrying capacity, limiting the effect of the logistic growth term in Eq. (2.4). Additionally, model behavior is insensitive to r for low values of $k_{d,B}$. Accordingly, the high variance in parameter estimates in this range noted in 2.5.2 does not affect model predictions.

2.5.4 Doxorubicin Treatment Response

Experimentally, all cell lines demonstrated a graded concentration-dependent and time-dependent response to doxorubicin treatment. Prior to treatment with doxorubicin at $t = 0$, each cell line displayed exponential growth. The proliferation rate (k_p) of the SUM-149PT, MDA-MB-231, MDA-MB-453, and MDA-MB-468 cell lines were 2.69×10^{-2} hr^{-1}, 2.23×10^{-2} hr^{-1}, 1.64×10^{-2} hr^{-1}, and 1.18×10^{-2} hr^{-1}, respectively. In untreated controls, each cell line demonstrated

Figure 2.6: Eq. (2.4) was populated with Eq. (2.5) and simulated with five levels of additive noise (0, 5, 10, 15, 20%). Parameters were recovered from those simulations, and the fit parameter value ($k_{d,A}$) is compared to its true value. The average value and 95% confidence interval of parameter fits are shown. The fitting procedure can recover parameter values across all simulated conditions.
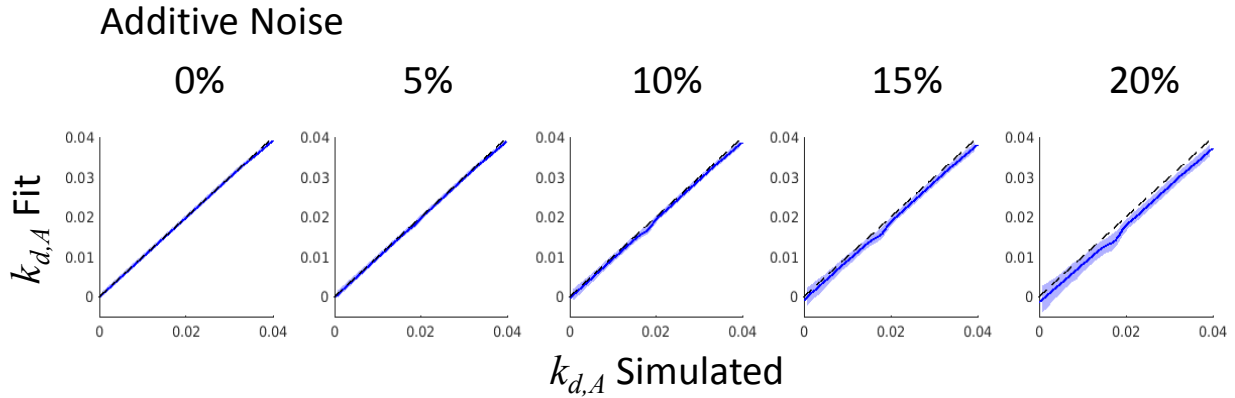
Figure 2.7: Eq. (2.4) was populated with Eq. (2.6) and simulated with five levels of additive noise (0, 5, 10, 15, 20%). Parameters were recovered from those simulations, and the relative percent error of the fit parameters ($k_{d,B}$ and r) are reported. While the fitting procedure can recover parameter values across all simulated conditions, consistently high error rates in r estimates were observed at low values of $k_{d,B}$. The uncertainty in r for small $k_{d,B}$ does not affect model predictions as demonstrated by the sensitivity analysis in Figure 2.8.
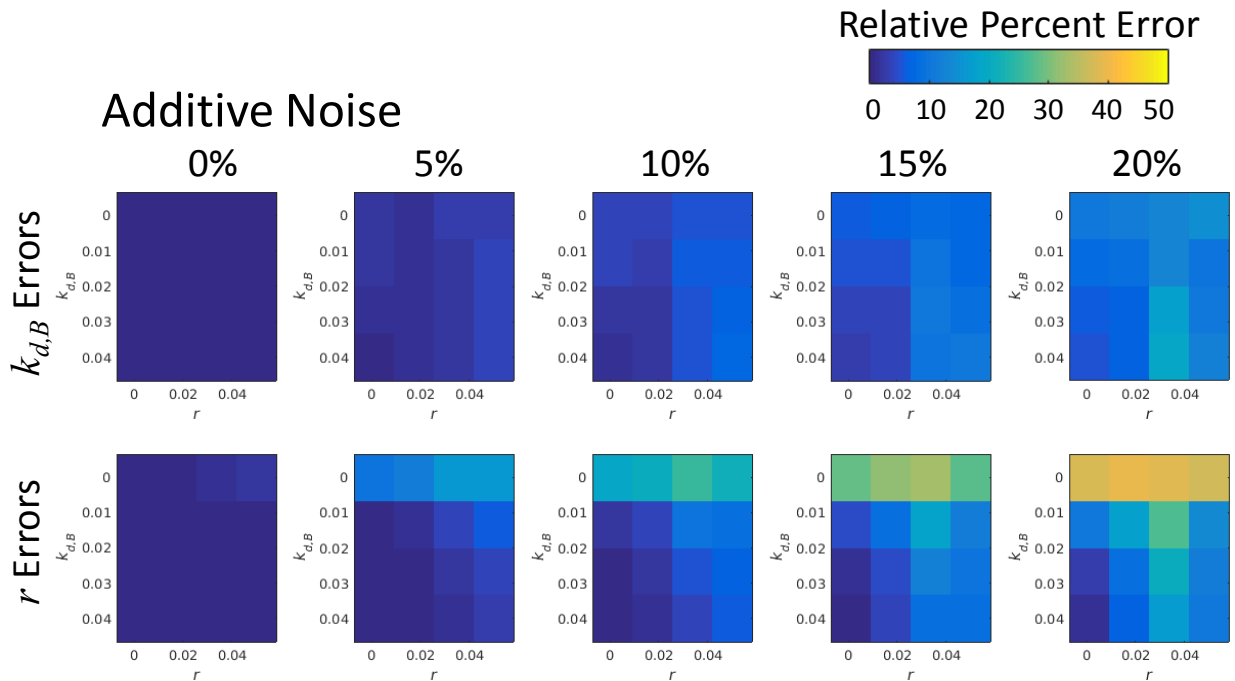
Figure 2.8: The sensitivity of model behavior to parameter variation was measured *via* the extended Fourier Amplitude Sensitivity Test (eFAST (157)) and reported with S_{TI}, the total-order sensitivity index. S_{TI} represents the fraction of model output variance that can be apportioned to variance in the parameter under investigation and is scaled from 0 (insensitive) to 1 (sensitive). The sensitivity of model behavior 7, 14, and 28 days following treatment are reported in (a-c) as a function of $k_{d,B}$. The errorbars represent one standard deviation. A *dummy* parameter is included for reference. This parameter is not in the model and thus the model should be insensitive to its variation. Notably, model behavior is insensitive to r for low values of $k_{d,B}$. Additionally, model behavior is insensitive to θ at early timepoints and high $k_{d,B}$ values as the cells counts are much lower than the carrying capacity in these conditions, limiting the effect of the logistic growth term.
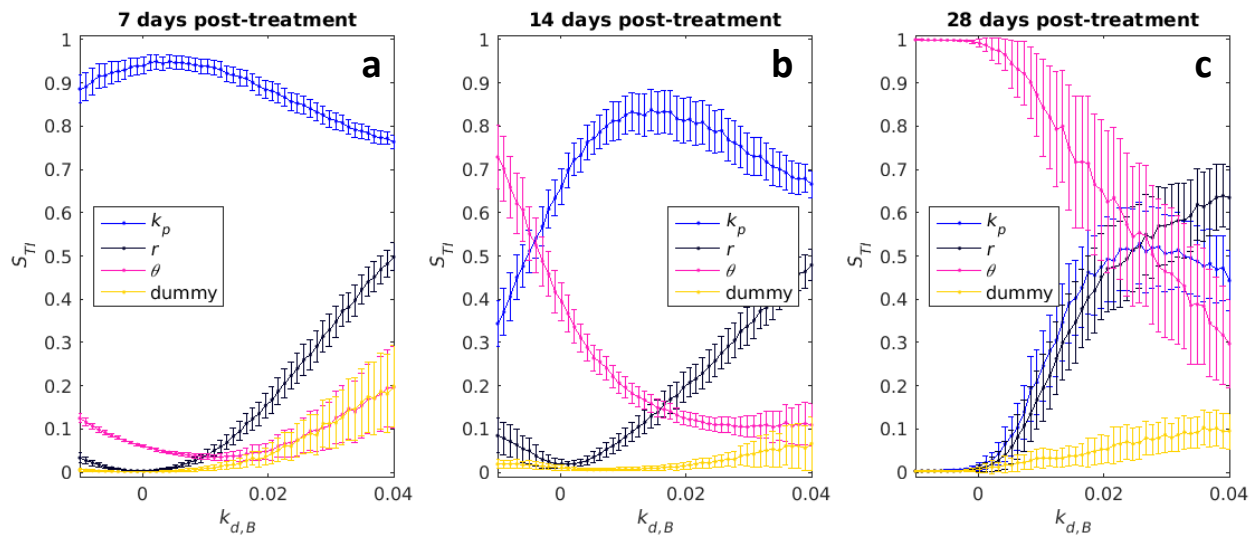
logistic growth with cell-line specific carrying capacities (θ) of 3.81×10^4, 1.86×10^4, 2.21×10^4, and 1.64×10^4 for the SUM-149PT, MDA-MB-231, MDA-MB-453, and MDA-MB-468 cell lines (Figure 2.9).

Following treatment, responses varied from continued, positive growth up to immediate population regression. This spectrum of responses is illustrated by the SUM-149PT response data in Figure 2.10. At low doses ($AUC < 480$ nM·hr) doxorubicin has little effect, and cell populations continue to grow exponentially up to a carrying capacity (2.10a-2.10c). As concentration and exposure time increase, the population growth rate appears to slow (2.10d). Eventually, a nonlinear response defined by a protracted slowing of population growth rate with a recovery back to pre-treatment growth rate is observed (2.10e-2.10h). At high doses ($AUC > 25 \times 10^3$ nM·hr), the cell population rapidly declines ($k_{d,A} \geq 2.9 \times 10^{-2}$ hr^{-1}), and no population rebound is observed during the experiment (2.10i).

The dose levels that correspond to the effects described above were specific to each cell line. In Figure 2.11, cell counts from each cell line following doxorubicin treatment for six hours at three concentrations are shown. The SUM-149PT line is relatively insensitive to doxorubicin therapies, demonstrating continued growth in all treatment conditions shown in Figure 2.11. Comparatively, the MDA-MB-468 line is very sensitive to doxorubicin therapy, demonstrating complete population regression at low doxorubicin doses ($AUC \geq 186$ nM·hr). The MDA-MB-231 and MDA-MB-453 cell lines displayed intermediate sensitivity. Despite the differential sensitivities, each of these cell lines followed the same general pattern described above.

2.5.5 Model Fits

As described in Section 2.4.5, the treatment response model was fit to each treatment condition. These model fits and 95% confidence intervals are superimposed on the cell counts in Figures 2.10 and 2.11. The α values used to generate the fits in Figures 2.9-2.14 were (α for Eq. (2.5), α for Eq. (2.6)): (10,1) for SUM-149PT, (6,1) for MDA-MB-231, (6,2) for MDA-MB-453, and (4,3) for MDA-MB-468. The mean percent error across all timepoints and mean percent error at the end of experiment (EoE) for the best-fit model to the SUM-149PT cell line after 6 and 24 hours of doxorubicin treatment are reported in Table 2.1. As shown in Table 2.1, the model was able to accurately capture a wide range of treatment conditions very accurately

Figure 2.9: Control data from dose-response experiments in a panel of TNBC cell lines. Each cell line was plated and serially imaged *via* fluorescence microscopy for 30 days. Nuclear counts from these images are displayed below in black with error bars representing the 95% CI from the six experimental replicates. Each column corresponds to an individual cell line. Data are truncated when cell populations reached carrying capacity. These counts are fit to Eq. (2.4) with $k_d = 0$ as described Section 2.4.5. Model fits with 95% CI are superimposed on the cell counts. Each cell line demonstrates a characteristic growth rate (k_p) and carrying capacity (θ).
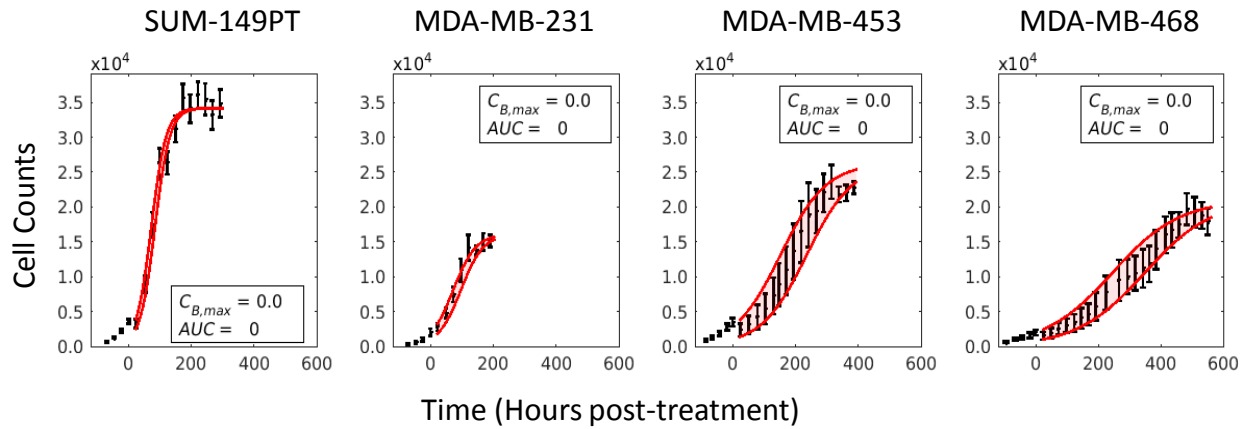
Figure 2.10: Impact of doxorubicin concentration and exposure time on response of SUM-149PT cells. The SUM-149PT cell line was plated and serially imaged *via* fluorescence microscopy for 30 days following time-resolved doxorubicin treatments. Nuclear counts from these images are displayed below in black with error bars representing the 95% CI from the six experimental replicates. These counts are fit to Eqs. (2.4) - (2.5) as described Section 2.4.5. Model fits with 95% CI are superimposed on the cell counts. The SUM-149PT cell line demonstrated a graded dose-dependent and time-dependent response to doxorubicin treatment. At low concentrations, no appreciable treatment effect is noted regardless of exposure time (a-c). At higher concentrations and exposure times, the population growth rate slows (d-e), eventually demonstrating a prolonged response to therapy with subsequent regrowth of the population (f-h). At very high concentrations and exposure times, no population regrowth is observed (i).
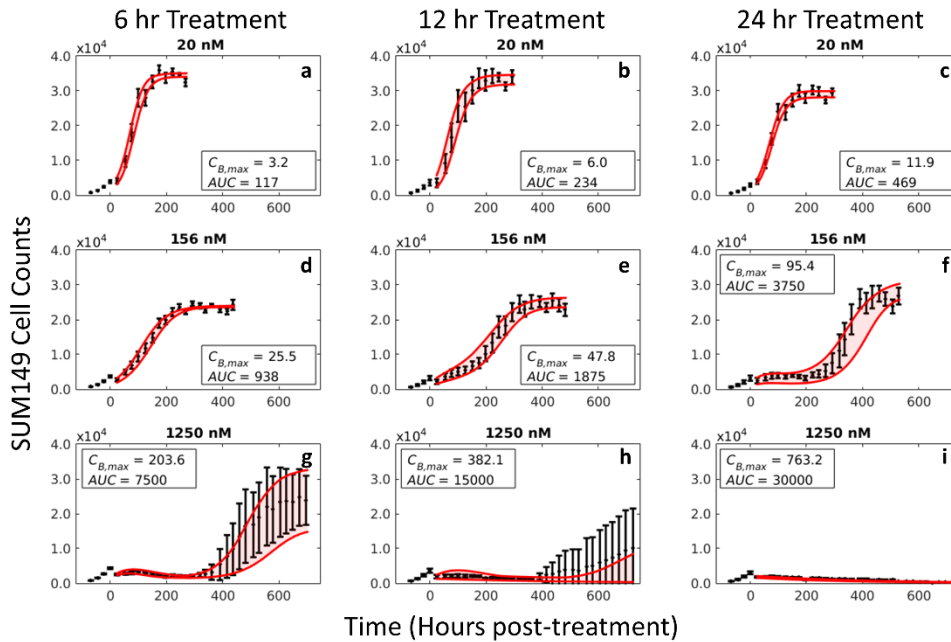
Figure 2.11: Dose-response curves in a panel of TNBC cell lines. Each cell line was plated and serially imaged *via* fluorescence microscopy for 30 days following a 6-hour doxorubicin treatment. Nuclear counts from these images are displayed below in black with error bars representing the 95% CI from the six experimental replicates. Each column corresponds to an individual cell line, and each row corresponds to a doxorubicin concentration. These counts are fit to Eqs. (2.4) - (2.5) as described Section 2.4.5. Model fits with 95% CI are superimposed on the cell counts. While there is significant variability in cell line sensitivity to doxorubicin treatment, the dynamics of each cell line follows a similar pattern: following treatment the population growth rate slows as a function of treatment, and depending on the concentration duration and concentration, a rebound in population growth rate is observed.
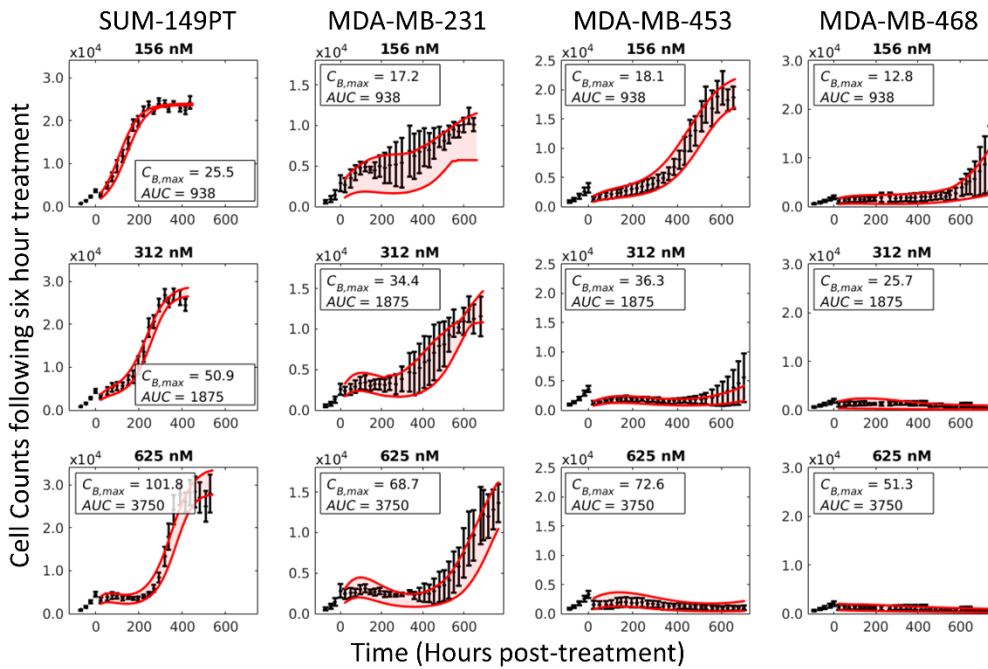
Table 2.1: Model fit statistics for SUM-149PT cell line following 6 and 24 hours of treatment with doxorubicin.

	SUM-149PT							
	6 hour Doxorubicin Treatment				24 hour Doxorubicin Treatment			
	Average % Error		Mean % Difference EoE		Average % Error		Mean % Difference EoE	
Concentration (nM)	Best-fit	Predicted	Best-fit	Predicted	Best-fit	Predicted	Best-fit	Predicted
10	5.3	5.5	3.8	4.7	6.4	7.1	5.7	5.7
20	5.3	5.6	3.0	3.6	5.6	9.5	4.3	7.0
39	6.1	6.6	4.6	6.3	5.5	10.2	4.9	8.1
78	6.1	7.1	5.0	6.6	10.3	10.5	8.7	9.1
156	4.6	5.3	4.5	4.0	22.7	22.5	12.0	9.9
312	9.4	13.6	6.8	5.9	31.4	32.5	25.2	26.9
625	15.0	16.9	13.1	11.9	50.8	53.6	120.3	150.9
1250	34.0	37.3	34.3	34.2	30.2	40.6	23.1	101.0
2500	24.4	42.5	61.1	159.9	40.0	59.0	32.0	117.3
Average Errors	12.2	15.6	15.1	26.3	22.5	27.3	26.2	48.4

Table 2.2: Table of model statistics for SUM-149PT, MDA-MB-231, MDA-MB-453, and MDA-MB-468 cell lines following 12 hour doxorubicin treatment.

	Average % Error of Best-Fit Model (12 hour dataset)			
Concentration (nM)	SUM-149PT	MDA-MB-231	MDA-MB-453	MDA-MB-468
10	7.1	10.3	7.7	7.6
20	7.2	8.3	10.2	6.9
39	5.9	12.1	9.0	11.1
78	5.5	19.1	15.0	21.6
156	10.3	19.4	20.2	35.9
312	19.0	33.1	22.6	32.4
625	31.4	36.9	26.2	34.2
1250	46.6	41.8	30.0	30.2
2500	47.6	32.3	48.9	30.1

with mean percent errors of $\leq 15\%$ for concentrations less than 625 nM after 6 hours of treatment. At higher concentrations, the model appears to perform poorly with mean errors $>25\%$. However, in these cases, the small number of cells results in noisier measurements at all timepoints. Corresponding statistics for MDA-MB-231, MDA-MB-468, and MDA-MB-453 cell lines can be found in Table 2.2.

Model parameter values changed with respect to treatment conditions within a given cell line. In Figure 2.12, the parameter values with corresponding 95% confidence intervals extracted from experiments with the SUM-149PT cell line are reported. Note that the parameter values extracted across all exposure-time experiments for all investigated cell lines appear to collapse to a single curve for each parameter when plotted as a function of $C_{B,max}$. Similarly, the carrying capacity (θ) appears to change slightly as a function of treatment condition (Figure 2.13). However, θ was unable to be estimated for high doxorubicin doses that induce population regression. Further, different models are selected over the range of treatments. Eq. (2.6) is favored at lower $C_{B,max}$ values ($w_B \approx 1$) for the SUM-149PT cell line, while Eq. (2.5) is selected at higher values ($w_B \approx 0$) (Figure 2.14). Of note, the model is relatively insensitive to values of r at low $C_{B,max}$ with $S_{TI} \leq 0.3$ (meaning that other parameters account for 70% of model variation in this range).

2.5.6 Model Predictions

The prediction scheme in Section 2.4.6 was trained on the 12-hour exposure time dataset in the SUM-149PT cell line to generate predictions of population dynamics following 6- and 24-hour doxorubicin treatments. A set of model predictions is shown in Figure 2.15 overlaid on experimental data, and predictions appear to qualitatively match experimental data. Table 2.1 reports the mean percent error across all timepoints and mean percent error at the EoE of the predictions for the SUM-149PT cell line at each concentration. As shown in Table 2.1, the error rates of the predicted model compare favorably to those of the best fit model, with the average percent error differing by 3.4% between the groups, on average. Further, the predictive model performs very well according to average error at concentrations up to 625 nM with an average error of 8.7% across those concentrations. The predictions degrade along with the best-fit model at higher concentrations. Similar results were obtained when the prediction scheme was trained with the 6-hour and 24-hour datasets (Table 2.3 and 2.4 respectively). The average percent error differed by 4.1% between the best fit and predicted models on average in these experiments.

Figure 2.12: Parameter fits from Eq. (2.5) in a panel of TNBC cell lines as a function of $C_{B,max}$. The parameters in Eq. (2.5) are fit to each treatment condition as described in Section 2.4.5 and plotted with 95% confidence intervals against the cell-line specific simulated $C_{B,max}$ from Eqs. (2.1) – (2.3). The blue **X**'s, red **O**'s, and green **Δ**'s represent the parameter fits extracted from the 6, 12, and 24 hour exposure time datasets respectively. Model parameters estimated from each exposure time appear to collapse on each other, when described by $C_{B,max}$ – a summary statistic of each treatment condition. This indicates that the compartment model is effective at describing the treatments. Further, given that each cell line appears to follow a single trajectory for each parameter, this model can be used to predict cell population response to any predefined input function. The gray areas for parameter r represent treatment ranges where the total-order sensitivity index (S_{TI}), which describes the effect of parameter variation on model prediction variation, is ≤0.3. Thus the large variance in parameter estimates here has a limited impact on model predictions.
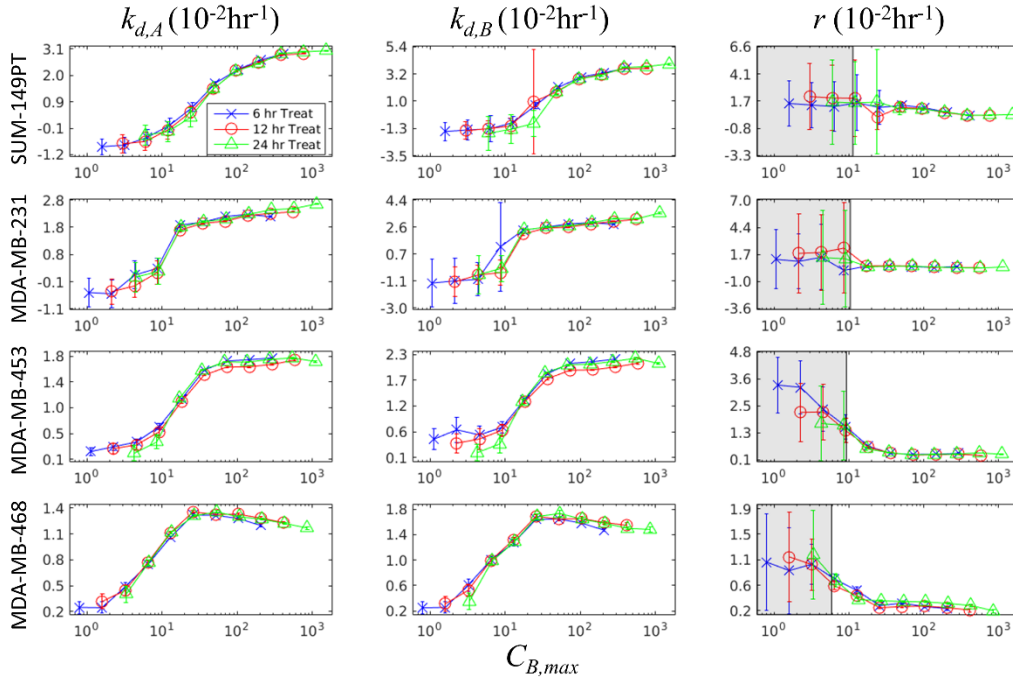
Figure 2.13: θ fits in a panel of TNBC cell lines as a function of $C_{B,max}$. θ's under Eqs. (2.5) – (2.6) are fit to each treatment condition as described in Section 2.4.5 and plotted with 95% confidence intervals against the cell-line specific simulated $C_{B,max}$ from Eqs. (2.1) – (2.3). The blue X's, red O's, and green Δ's represent the parameter fits extracted from the 6, 12, and 24 hour exposure time datasets respectively. Model parameters estimated from each exposure time appear to collapse on each other, when described by $C_{B,max}$ – a summary statistic of each treatment condition. Notably, the carrying capacity appears to vary slightly as a function of treatment condition. Additionally, large error bars are observed for high values of $C_{B,max}$. Under these treatment conditions, the cell population does not approach carrying capacity, and the parameter is unable to be resolved.
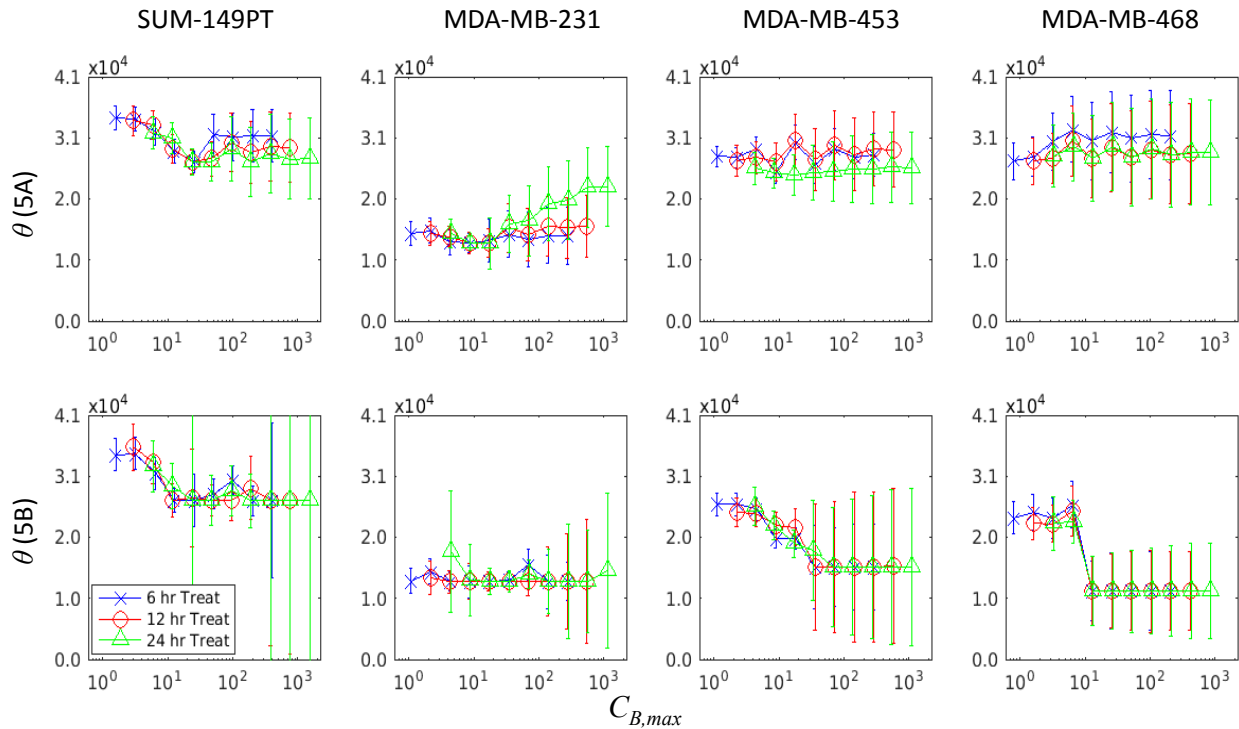
Figure 2.14: Model weights vary across dose range. Each model (i.e., Eq. (2.5) and (2.6)) was fit to each treatment condition in the training set. The AIC was calculated for each model fit, and the models were weighted as described in Section 2.4.5. The blue X's, red O's, and green Δ's represent the parameter fits extracted from the 6-, 12-, and 24-hour exposure time datasets respectively. Note that the model fit transitions from Eq. (2.6) ($w_B = 1$) to Eq. (2.5) ($w_B = 0$) as doxorubicin dose increases.
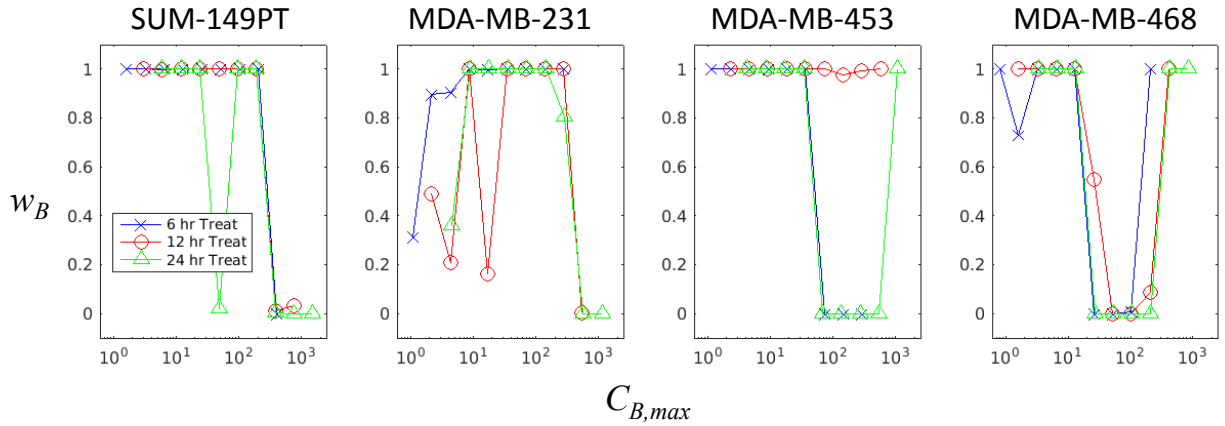
2.6 Discussion

A modeling approach has been introduced that can be used to summarize the PK/PD properties of doxorubicin in TNBC cell lines. Cell-line specific model parameters can be estimated from experimental data, revealing phenotypic heterogeneity in PK/PD properties not previously quantified. Further, the PD properties were found to vary as a function of $C_{B,max}$ and AUC, summary statistics of doxorubicin PK. This allows for accurate prediction of cell population behavior for up to one month following prescribed doxorubicin treatments *in vitro*.

The pharmacokinetics of doxorubicin binding in a panel of cell lines can be characterized by a three compartment model. Similar to findings by Shin *et al.*, there are significant differences in doxorubicin pharmacokinetics among TNBC cell lines (144). Interestingly, these parameters are only loosely correlated with response. For example, the MDA-MB-231 has a greater uptake of doxorubicin (as estimated by $C_{B,max}$) than the MDA-MB-468 line; however, the MDA-MB-468 line is more sensitive to doxorubicin therapy. This suggests that each cell line has an intrinsic sensitivity to stress by doxorubicin. More generally, this model can be leveraged to isolate and normalize for variable uptake dynamics in the context of doxorubicin resistance. This could help refine approaches to identify mechanisms of resistance and subsequently develop targeted agents to address those mechanisms.

The model relating treatment variables (concentration and duration) to subsequent cell population size dynamics proposed in this work captures behavior across a range of TNBC cell lines. While each cell line can be described by a specific set of parameters, there is an underlying behavior common to all cell lines that is described by the model: an apparent continuum of responses from exponential growth to population regression as doxorubicin concentration and exposure time are increased. Further, TNBC response to doxorubicin therapy generally appears to be a deterministic process. Over a wide range of treatment conditions, cell populations responded consistently, as evidenced by the confidence intervals on the cell count data in Figures 2.10, 2.11, and 2.15, the overlapping parameter curves in Figure 2.12, and the accuracy of predictions in Table 2.1. Several models in the literature have assumed a direct relationship between treatment variables and cellular response – either immediate (159) or following some fixed delay (135,160). Consistent with those delay models, the data presented in this work indicate that drug effects occur on a slower timescale relative to drug binding. Characterizing and reporting on these dynamic

Figure 2.15: Model prediction results in SUM-149PT cell line. As described in Section 2.4.6, model parameters ($k_{d,A}$, θ in Eq. (2.5) and $k_{d,B}$, r, θ in Eq. (2.6)) were fit to each treatment condition in the training set (12-hour exposure dataset). These parameter fits were then described by local regression models to generate model parameter estimates for treatments in the test set (6- and 24-hour exposure datasets). Final predictions represent a weighted average of Eqs. (2.5) and (2.6), and a bootstrap analysis was used to generate a 95% confidence interval for these predictions (red overlay). A series of predictions in the SUM-149PT cell line following 6- and 24-hour doxorubicin treatments at three doxorubicin concentrations are shown. Nuclear counts from these experiments are displayed in black with error bars representing the 95% CI from the six experimental replicates. Each column corresponds to an exposure time. The response of a TNBC cell line can be predicted using experimentally-derived PK and PD parameters.
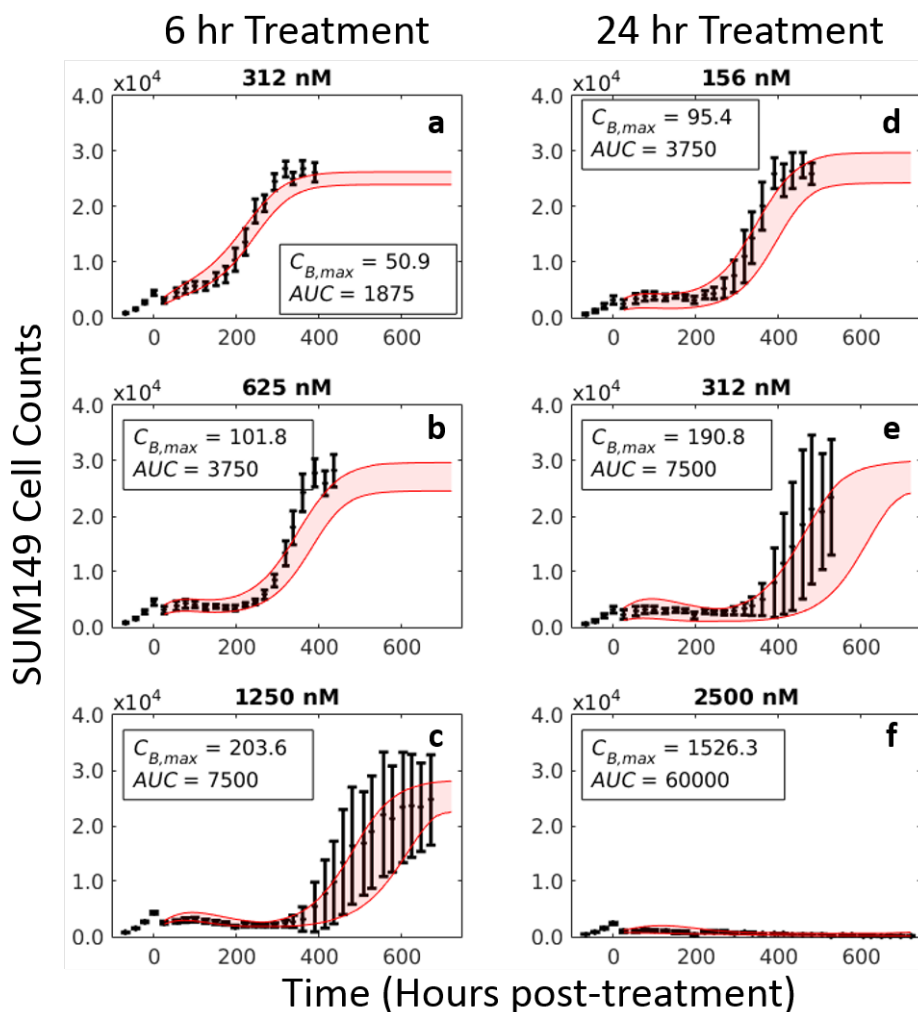
measures would enhance information from traditional potency-based assays. Understanding the dynamics of therapeutic administration and treatment response can inform drug treatment schedules and will provide guidance to optimize response monitoring.

Interestingly, there appears to be an upper threshold on doxorubicin treatment above which all cells die. As that concentration threshold is approached, increased variance is observed in population dynamics, especially at later timepoints. For example, in this range of therapy, one or two experimental replicates would regrow while no growth was observed in the other replicates (e.g., Figure 2.10h). This contributes partly to the high error rates at high concentrations in Table 2.1. In these cases, the heterogeneity of the cell population or stochastic cell fate decisions may likely have an increased influence on population dynamics (161). We emphasize that such increases in variance are more often observed as this treatment threshold is approached. This observation questions the use of maximum tolerated dosing schemes, which operate in this high-variance range (162,163). Considering the data presented in this work in the context of proposed adaptive dosing and metronomic dosing approaches (12,20,123,124), there may exist a framework in which drug schedules can be customized for each patient to generate predictable changes in tumors. Indeed, the PK/PD modeling framework proposed in this work provides a means to more precisely test those alternative therapeutic approaches. Even in the current state of TNBC therapy, doxorubicin is often delivered on a predefined schedule for all patients with only doses adjusted for patient body-surface area. The demonstrated heterogeneity among TNBC cell lines, both in their uptake of doxorubicin and the effect of doxorubicin on those cell behaviors, suggests that additional metrics are needed for proper dosing of doxorubicin in TNBC. Tumor-specific PK properties may be required to normalize tumor response measurements to delivered doxorubicin dose.

This work is further distinguished through its use of a model averaging approach; i.e., the best-fit PD model is a weighted average of two distinct treatment response models (Eqs. (2.5) and (2.6)). Fundamentally, different cellular processes dominate over the dose range investigated (apoptosis at high doses, mitotic catastrophe at low to intermediate doses) (151,152). These disparate behaviors are observed in the data, and the model was constructed to account for these behaviors. Notably, Eq. (2.5) is unable to explain the regrowth seen at low doses, and Eq. (2.6) is unable to describe permanent population regression seen at high doses. The model averaging approach demonstrated here can be used to summarize the behavior of cell populations over the

entire range of doses investigated. Further, this approach can be used to gain biological insight into the behavior of cell lines. Apoptosis is commonly treated as a switch-like process, which commits a cell to death at some biologically-defined threshold (164). Similarly, a switch in model weights towards Eq. (2.5) (apoptosis) is observed for each cell line as doxorubicin dose increases (Figure 2.14). Model averaging approaches can limit the insight gained from modeling as different models can be selected over the range of experimental conditions without an apparent pattern. However, explicitly incorporating biologically-motivated models into a model averaging framework may improve both model accuracy and expand the insight derived from modeling approaches.

As demonstrated in Figure 2.15 and Table 2.1, the prediction framework proposed in this paper performs well across the range of treatments and cell lines investigated. This predictive modeling framework is dependent on: 1) the observation that model parameters are functions of treatment variables, and 2) these treatment variables can be summarized by $C_{B,max}$ and AUC. Despite the relative simplicity of the models proposed in this work and the pharmacokinetic features used to predict parameter values, this framework is able to generate relatively accurate predictions to all experimental treatments in the SUM-149PT cell line, regardless of the training set used. While doxorubicin has been in clinical use for several decades, to our knowledge, measurements of its cellular effects have not previously been coupled to intracellular concentrations in a predictive framework. More broadly, this framework is readily amendable to predict response to other cytotoxic therapies. Although it is nearly certain that other cytotoxic therapies will require different parameter sets or, even, mathematical models, the coupled experimental-modeling approach presented in this work can be used to generate predictions following construction of those drug-specific models.

While the results of this study are promising, several limitations exist in the current approach. With respect to the compartment model proposed to describe doxorubicin pharmacokinetics, model parameters may change as a function of treatment concentration and duration, as suggested by the distribution of residuals seen in Figure 2.5. Characterization of such variation through more extensive experiments may be possible, but doxorubicin exerts an effect on the cells over the course of the experiments – inherently changing the values of the compartment model. For example, cell size was observed to shrink during doxorubicin exposure. This reduced volume would enhance the fluorescent signal measured from intracellular space in these

Table 2.3: Model fit statistics for SUM-149PT cell line following 12 and 24 hours of treatment with doxorubicin.

	SUM-149PT							
	12 hour Doxorubicin Treatment				24 hour Doxorubicin Treatment			
	Average % Error		Mean % Difference EoE		Average % Error		Mean % Difference EoE	
Concentration (nM)	Best-fit	Predicted	Best-fit	Predicted	Best-fit	Predicted	Best-fit	Predicted
10	7.1	7.6	5.8	5.5	6.4	8.1	5.7	6.2
20	7.2	8.1	5.5	5.7	5.6	12.4	4.3	9.3
39	5.9	7.0	3.7	4.2	5.5	12.6	4.9	12.1
78	5.5	7.1	4.6	6.1	10.3	13.3	8.7	13.7
156	10.3	13.0	9.0	15.1	22.7	23.7	12.0	12.6
312	19.0	21.0	21.1	21.7	31.4	35.7	25.2	37.4
625	31.4	33.6	23.0	33.3	50.8	42.7	120.3	89.5
1250	46.6	40.8	125.0	78.8	30.2	34.3	23.1	66.8
2500	47.6	47.7	82.2	75.3	40.0	49.6	32.0	74.6
Average Errors	20.1	20.7	31.1	27.3	22.5	25.8	26.2	35.8

Table 2.4: Model fit statistics for SUM-149PT cell line following 6 and 12 hours of treatment with doxorubicin.

	SUM-149PT							
	6 hour Doxorubicin Treatment				12 hour Doxorubicin Treatment			
	Average % Error		Mean % Difference EoE		Average % Error		Mean % Difference EoE	
Concentration (nM)	Best-fit	Predicted	Best-fit	Predicted	Best-fit	Predicted	Best-fit	Predicted
10	5.3	7.6	3.8	7.1	7.1	9.9	5.8	8.9
20	5.3	7.7	3.0	7.2	7.2	7.3	5.5	5.3
39	6.1	7.2	4.6	5.9	5.9	9.8	3.7	8.7
78	6.1	13.7	5.0	5.5	5.5	11.5	4.6	6.3
156	4.6	13.9	4.5	10.3	10.3	10.9	9.0	8.6
312	9.4	15.9	6.8	19.0	19.0	19.2	21.1	22.7
625	15.0	18.8	13.1	31.4	31.4	33.1	23.0	22.1
1250	34.0	41.7	34.3	46.6	46.6	49.0	125.0	112.8
2500	24.4	46.4	61.1	47.6	47.6	50.7	82.2	62.1
Average Errors	12.2	19.2	15.1	20.1	20.1	22.4	31.1	28.6

experiments. While the compartment model explicitly incorporated the volume of these compartments with estimates of cell volume, additional parameters would be needed to account for the time-dependent variation in compartment volumes. Indeed, when each treatment condition in the compartment modeling experiment was fit independently, the value of k_{FB} appeared to increase with concentration and duration of therapy. While no significant violations of model assumptions are seen, it is difficult to rigorously test the assumption that parameters are independent of concentration and exposure time in the current dataset, which only contains four doxorubicin concentrations and two exposure times. Further, heterogeneity in the uptake of doxorubicin was observed. Within the field of view of the experiment, variation was noted from one cell to the next (Figure 2.2c). As the modeling approach collapsed all cells into a single drug uptake timecourse, this heterogeneity was not considered. It would be of interest to track these cells over time to determine cell-specific parameters in relation to drug administration (165). Further, this model does not explicitly include saturation kinetics for doxorubicin transport, which may contribute to the observed error rates. However, incorporating this heterogeneity would significantly increase the complexity of the proposed model, requiring additional equations and additional experimental data to describe each compartment model rate. Despite these limiting assumptions, the $C_{B,max}$ term calculated with the three compartment model allowed for prediction of pharmacodynamic properties.

The treatment response model was inspired by observations of treatment response in these cell lines. While the treatment conditions were designed to replicate those observed *in vivo*, it remains unknown how the proposed model would respond to more complex treatment curves; e.g., biexponential decay curves observed *in vivo* (143). Such dynamics should, in theory, be captured by the proposed doxorubicin PK model, but work remains to validate that assumption. Application of the model to an *in vivo* system will also require spatial considerations. For example, significant heterogeneity in perfusion exists within a tumor, impacting both tumor growth and drug delivery (90). The variable and immature vasculature may induce local microenvironmental changes (hypoxia, acidic extracellular pH) that alter the response to therapy (6,88). This modeling framework may need to be expanded to account for such spatial heterogeneity which can be characterized by (for example) quantitative imaging data (19). However, the translation of the logistic growth formulation has already been realized in several *in vivo* models (21,73,108,166,167).

2.7 Conclusion

In summary, these time-resolved treatment protocols sought to replicate the clinically observed pharmacokinetics of doxorubicin therapy more closely than the constant concentrations in previous dose-response assays. The proposed model, initialized with cell-line specific parameters, can describe the response to doxorubicin across a range of TNBC cell lines and treatment conditions. Further, within each cell line, the behavior collapses into a single path through parameter space as a function of treatment conditions. This observation allows for the *in vitro* response of each cell line to doxorubicin treatment to be predicted. Through the development of a mathematical model that explicitly considers both doxorubicin pharmacokinetics and pharmacodynamics, exploration of a wide range of treatment protocols that would be intractable experimentally is now possible. Specifically, this model provides an imminently scalable approach to predicting tumor changes in response to doxorubicin pharmacokinetics *in vivo*. This approach should allow for further refinement of biological models of doxorubicin treatment response, scalable predictions of tumor response in animal models, and, eventually, personalized, computationally-optimized treatment regimens that maximize tumor control with doxorubicin.

CHAPTER 3

EQUIVALENT DOSE: LEVERAGING MATHEMATICAL MODELING TO QUANTIFY PHARMACOKINETIC AND PHARMACODYNAMIC PROPERTIES

3.1 Introduction and Contribution of Study

Conventionally, drug response assays are summarized *via* sigmoidal functions that describe cell survival data at a single timepoint with respect to applied drug concentration. Such analysis has a limited biophysical basis. Notably, drug pharmacokinetic and pharmacodynamic properties are conflated in describing cell response to therapy, fundamentally limiting the biological insight to be gained from the analysis. In this chapter, we build on the experimental-mathematical modeling approach developed in Chapter 2 and propose a new metric, termed the "equivalent dose" as a more precise means for quantifying treatment response assays. Specifically, we demonstrate the utility of the proposed metric in comparing cell lines and quantifying the effect of agents that modulate cellular pharmacologic properties. In this way, we aim to demonstrate that the response to doxorubicin is predictable and can be summarized in a relatively parsimonious mathematical model.

3.2 Abstract

Treatment response assays are often summarized *via* sigmoidal functions comparing cell survival to applied drug concentration. This approach has a limited a biophysical basis, thereby reducing the biological insight to be gained from such analysis. Notably, drug pharmacokinetic and pharmacodynamics properties are overlooked in developing treatment response assays, and the accompanying summary statistics conflate these processes. Here, we present a coupled experimental/modeling approach specifically designed to account for variable cellular pharmacokinetics and pharmacodynamics. We propose the equivalent dose metric, a value derived from a mechanistic pharmacokinetic/pharmacodynamic model that explicitly accounts for variable cell line pharmacological properties, to more precisely summarize treatment response assays. The equivalent dose is calculated with cell line specific PK/PD properties, allowing for treatment response in different cell lines to be more accurately compared. Further, the approach can incorporate the effect of agents that modulate cellular pharmacokinetics and pharmacodynamics,

precisely quantifying the effect of those agents. This data can be used to identify novel drivers of treatment response and potentially modulate dosing of combination agents.

3.3 Introduction

The parameterization of *in vitro* treatment response data is central to biomarker and drug discovery and to the quantitative study of cancer therapies. With recent exceptions (130,131), investigation of treatment response *in vitro* has been limited to end-point cell survival assays that assess cell viability after a pre-determined time period following treatment with a constant concentration of drug. These assays are conventionally summarized by Hill function parameters, which compare cell survival to applied drug concentration. While this approach has yielded significant insights into cancer biology, it is fundamentally limited by the parameters used to summarize treatment response. These parameters do not explicitly characterize the dynamics of treatment and subsequent response. Further, response metrics are compared to the extracellular concentration of drug in the assay, overlooking drug exposure times and variable cell line pharmacologic properties. This not only impairs analysis of treatment response data, but also presents a challenge in translating these therapies *in vivo*.

There are a host of biochemical processes that can modulate a tumor cell's response to therapy. For example, the accumulation of drug within cells can be altered by several mechanisms, including differential drug metabolism or modification of surface proteins that regulate drug flux through the membrane (168,169). Indeed, the multi-drug resistance protein 1 (MDR1) is a well-studied mechanism of resistance to cytotoxic therapies (170). This ATP-dependent pump actively effluxes drug from cells, decreases drug accumulation within cells, and confers resistance to anthracyclines, taxanes, and several other agents (120). Similarly, pharmacodynamic response to therapies can be altered through modulation of signaling pathways downstream of the therapeutic target. With respect to DNA-damaging agents, changes in DNA repair pathways, which are activated in response to treatment, can alter sensitivity to those agents (171,172). For example, DNA-dependent protein kinase (DNA-PK) plays a major role in the repair of double strand DNA breaks *via* non-homologous end joining (173). Increased expression of DNA-PK has been shown to confer resistance to doxorubicin, an anthracycline commonly used clinically (174).

Fundamentally, the cell line-specific pharmacokinetic and pharmacodynamic properties described above drive observed survival responses. Using conventional methods, these processes

are conflated by the parameters used to summarize *in vitro* dose response data, such as the EC_{50}, which describes the applied concentration of drug that elicits a half-maximal effect (175,176). The result is an imprecise measure of drug efficacy, which limits the biological insights to be gained from the data. While a pair of recent approaches have proposed normalizing for cellular proliferation rate in the analysis of cell survival data (130,131), these still overlook the fundamental pharmacologic properties that determine response.

More precise metrics are required to advance systems approaches to studying cellular response to therapy (22). New assays are needed that integrate previous biological insights to more effectively advance the study of anticancer therapeutics and identify the biological drivers of treatment response. We posit that a mechanistic, mathematical modeling framework is essential to maximize the knowledge gained through treatment response studies. In this paradigm, biologically-motivated mathematical models are constructed to describe observed behaviors of the system under investigation. The model is then fit to experimental data, yielding a set of parameter values that provide mechanistic insight into observed data. Recently, we proposed and validated a coupled pharmacokinetic/pharmacodynamic (PK/PD) model of doxorubicin treatment response *in vitro* (177). The model incorporates measured doxorubicin pharmacokinetics and pharmacodynamics and allows for *prediction* of response following a specified treatment timecourse on a cell-line specific basis. Specifically, we observed that the concentration of doxorubicin bound to the nucleus, which is estimated with the PK model, is predictive of cell line pharmacodynamics. The model behaves consistently across a wide spectrum of treatment protocols and cell lines thereby demonstrating that the dynamics of the response of cancer cell lines to doxorubicin is predictable. We further noted a mismatch of drug uptake and response among the investigated cell lines, suggesting that each cell line has an intrinsic sensitivity to stress induced by doxorubicin. By explicitly modeling both drug uptake and subsequent effect, these processes can be precisely quantified to study each component of treatment response.

It is the goal of the present effort to demonstrate the utility of a mechanistic, mathematical framework for quantitatively investigating treatment response. We propose to extend the radiobiology concept of equivalent dose to account for variable cell line pharmacokinetics and pharmacodynamics in the study of chemotherapy. In radiobiology, the equivalent dose is the total radiation dose weighted by the sensitivity of tissue to the applied dose, and it is commonly used to compare radiation fractionation schedules (178). Similarly, in the context of chemotherapy, we

define equivalent dose as a mixed measure of absorbed drug mass and the biological effect of the absorbed drug. We further specify that a cell line's response to therapy be constant for a delivered equivalent dose. We posit that this approach will account for varying cellular properties, allowing for more precise comparisons to be made among cell lines relative to extracellular drug concentration. Finally, we hypothesize that the mechanistic modeling approach will allow for more precise application of targeted agents that modulate pharmacologic properties.

In this work, we demonstrate the utility of the equivalent dose metric by independently perturbing cell-line specific doxorubicin pharmacokinetics and pharmacodynamics through the use of chemical inhibitors of each process. Specifically, we modulate pharmacokinetics in an MDR1 over-expressing cell line and modulate pharmacodynamics *via* DNA-PK in a BRCA1-mutated cell line. In this way, we aim to demonstrate that a host of previous knowledge of doxorubicin treatment response can be summarized in a relatively parsimonious mathematical model. We demonstrate how various pharmacological properties that contribute to observed responses can be quantified to provide more precise biological insight into treatment response.

3.4 Materials and Methods

3.4.1 Mathematical Model of Doxorubicin Treatment Response

Doxorubicin is an anthracycline that remains standard-of-care therapy for several cancers (146). Ultimately, doxorubicin induces a host of cellular stress responses, which either inhibit further DNA synthesis allowing for cellular recovery or initiate a cascade leading to cell death (147). At high doxorubicin concentrations, extensive DNA damage often results in cell death *via* apoptosis. Low to moderate concentrations of doxorubicin induce cell senescence, and cell death occurs primarily *via* mitotic catastrophe (151,152). Whereas apoptosis is immediate (on the order of hours to days), mitotic catastrophe is a relatively protracted process (on the order of several days).

We previously developed and validated a parsimonious treatment response model to describe doxorubicin pharmacokinetics and pharmacodynamics. Briefly, a three-compartment model was employed to describe the uptake and binding of doxorubicin in cancer cells. This process is modeled *via* mass conservation through Eqs. (3.1) - (3.3):

$$\frac{dC_E(t)}{dt} = k_{FE}\frac{v_I}{v_E}C_F(t) - k_{EF}C_E(t) \tag{3.1}$$

$$\frac{dC_F(t)}{dt} = k_{EF} \frac{v_E}{v_I} C_E(t) - k_{FE} C_F(t) - k_{FB} C_F(t) \tag{3.2}$$

$$\frac{dC_B(t)}{dt} = k_{FB} C_F(t) \tag{3.3}$$

where $C_E(t)$, $C_F(t)$, and $C_B(t)$ are the concentrations of doxorubicin in the extracellular, free, and bound compartments, respectively, at time t. The free compartment represents drug that has diffused into the cell, while the bound compartment represents drug that has bound to the DNA. The k_{ij} parameters are rate constants that describe the movement of doxorubicin between each of these compartments; for example, k_{FE} describes the rate of drug transfer from the free, intracellular compartment to the extracellular compartment. Similar definitions apply to k_{EF} and k_{FB}. The volumes of the extracellular and intracellular compartments are denoted with v_I and v_E, respectively.

A logistic growth model, Eq. (3.4), modified by either of two time-dependent response functions, Eqs. (3.5) and (3.6), reflecting distinct mechanisms of cell death, was proposed to describe population level response to doxorubicin therapy as follows:

$$\frac{dN_{TC}(t)}{dt} = \left(k_p - k_d(t,D)\right) N_{TC}(t)\left(1 - \frac{N_{TC}(t)}{\theta(D)}\right) \tag{3.4}$$

$$k_d(t,D) = \begin{cases} 0 & t < 0 \\ k_{d,a}(D) & t \geq 0 \end{cases} \tag{3.5}$$

$$k_d(t,D) = \begin{cases} 0 & t < 0 \\ k_{d,b}(D)r(D)te^{1-r(D)t} & t \geq 0 \end{cases}, \tag{3.6}$$

where k_p and k_d are the proliferation and dose-specific death rates, respectively, D is the delivered dose (defined to be the bound concentration of drug calculated with Eqs. (3.1) – (3.3)), r is a dose-specific constant describing the rate at which treatment induces an effect, θ is the dose-specific carrying capacity describing the maximum number of cells that can be observed in the experimental system, and $N_{TC}(t)$ is the number of tumor cells at time t. Prior to treatment (i.e., $t < 0$), cells are modeled to have a constant proliferation rate, k_p. Following treatment at $t = 0$, Eq. (3.5) assumes an immediate induction of a stable, post-treatment death rate ($k_{d,a}$). Eq. (3.6) allows for a smooth induction of drug effect following treatment to a maximum death rate of $k_{d,b}$, while ultimately allowing for recovery of the cell population. The dynamics of this induction and decay

is governed by *r*. A weighted averaging approach is used to incorporate both Eqs. (3.5) and (3.6) in the treatment response model. Further details on the model can be found in previous work (177).

3.4.2 Equivalent Dose

We define equivalent dose as a mixed measure of absorbed drug mass and the biological effect of the absorbed drug. We further specify that a cell line's response to therapy (e.g., the response modeled by Eqs. (3.4) – (3.6)) be constant for a delivered equivalent dose. A target equivalent dose can be achieved in a variety of ways. For example, the extracellular drug concentration timecourse can be tuned to reach a specified equivalent dose. Alternatively, the same equivalent dose can be achieved by altering cell line pharmacologic properties with concomitant changes in the extracellular drug timecourse.

In the context of doxorubicin therapy, we define equivalent dose (D_{eq}) as the functional concentration of drug that is bound to the nucleus following therapy. As described above, doxorubicin diffuses into the cell, where it subsequently binds to the nucleus to exert its effect. Notably, in proposing the equivalent dose, we lump pharmacodynamic effects into the k_{FB} term. Specifically, k_{FB} is a mixed measure of doxorubicin binding and DNA repair. The equivalent dose is illustrated in Figure 3.1.

To calculate D_{eq} for a specified treatment condition (i.e., extracellular drug concentration timecourse), Eqs. (3.1) – (3.3) are populated by cell-line- and treatment-specific k_{EF}, k_{FE}, and k_{FB} parameters derived from experimental data (described below). The model is then run forward in time using the experimentally-defined extracellular doxorubicin concentration timecourse. D_{eq} is the maximum concentration of bound drug (C_B) as predicted by the simulation. We have previously shown that this metric can summarize doxorubicin treatment timecourses and is predictive of doxorubicin treatment response (177). We hypothesize that the equivalent dose metric will account for variable cell line pharmacologic properties through its explicit consideration of k_{EF}, k_{FE}, and k_{FB} rates, and it will be able to describe the effect of agents that modulate those properties.

3.4.3 Cell Lines

The MDA-MB-468 and SUM-149PT cell lines were obtained through American Type Culture Collection (ATCC, http://www.atcc.org) and maintained in culture according to ATCC recommendations. Cell lines were passaged no more than 30 times before being discarded.

Figure 3.1: Overview of equivalent dose metric. The response to therapy is determined by the applied drug concentration and cell-specific pharmacologic properties. Traditionally, therapeutic response is summarized relative to the applied extracellular concentration of drug. We propose the equivalent dose metric, D_{eq}, to summarize the contributions of various pharmacologic properties in shaping treatment response. We define equivalent dose as a mixed measure of absorbed drug mass and the biological effect of the absorbed drug. We further specify that a cell line's response to therapy be constant for a delivered equivalent dose. The equivalent dose is calculated through a mechanistic biophysical model that considers several sources of variability in shaping treatment response. The metric consolidates variable drug uptake (quantified with k_{EF}), efflux (quantified with k_{FE}), and binding (quantified with k_{FB}) into a single descriptor of treatment. The equivalent dose allows for more precise comparison of cell lines and provides a quantification of pharmacologic properties to provide biological insight into treatment response.
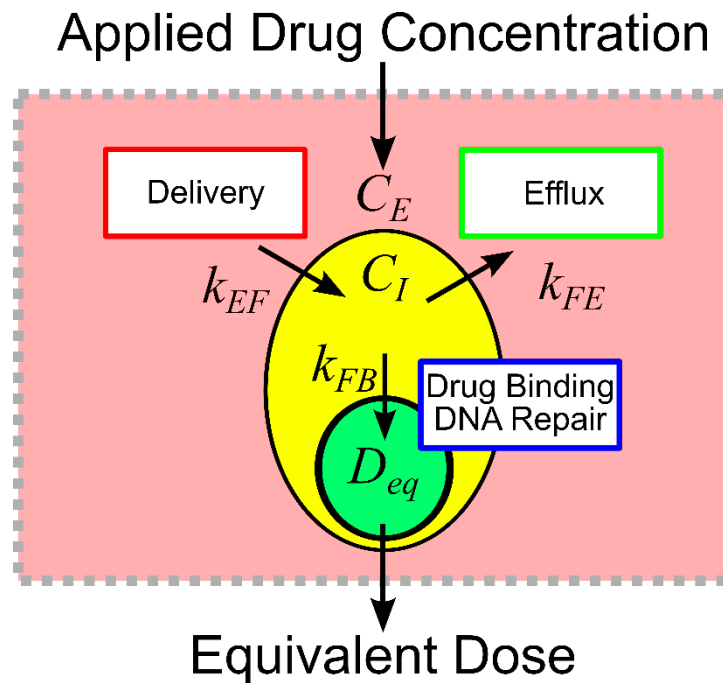
To facilitate automated image analysis for identifying and quantifying individual nuclei in the time-lapsed fluorescent microscopy experiments (described below), each cell line was modified to express a histone H2B conjugated to monomeric red fluorescent protein (H2BmRFP; Addgene Plasmid 18982) as previously described (140,141).

To specifically modulate pharmacokinetics, the H2BmRFP-expressing MDA-MB-468 cell line (MDA-MB-468$_{H2B}$) was transduced to express a green fluorescent protein (GFP)-tagged MDR1 protein (ABCB1 gene, Origene Technologies, Rockville, MD). Following transduction, the cell line was cultured in 100 nM doxorubicin for two weeks to select a doxorubicin-resistant phenotype (MDA-MB-468$_{MDR1}$). These cells were subsequently serially imaged to ensure that all surviving cells expressed GFP, and the expression of the GFP-MDR1 was stable.

To specifically modulate cellular pharmacodynamics, the DNA damage repair pathway in the SUM-149PT cell line was targeted. The SUM-149PT cell line possesses a BRCA1 2288delT mutation (179). BRCA1 is involved in maintaining genome stability through its role in repairing double strand DNA-breaks *via* homologous recombination (180). The BRCA1 mutation causes an increased reliance on alternate DNA damage repair pathways, such as non-homologous end joining (181).

Table 3.1: Model parameter definitions

Model Parameter	Units	Definition
k_{EF}	hr^{-1}	Rate of drug influx into cell
k_{FE}	hr^{-1}	Rate of drug efflux from cell
k_{FB}	hr^{-1}	Mixed rate of drug binding and DNA repair
C_E	nM	Extracellular doxorubicin concentration
C_I	nM	Intracellular, extranuclear doxorubicin concentration
C_B	nM	Concentration of doxorubicin bound to the nucleus
D_{eq}	nM	Equivalent dose
N_{TC}	Count	Number of cells
k_p	hr^{-1}	Proliferation rate of cells
θ	Count	Carrying capacity of experimental system
$k_{d,a}$	hr^{-1}	Death rate assumed in Eq. (3.5)
$k_{d,b}$	hr^{-1}	Death rate assumed in Eq. (3.6)
r	hr^{-1}	Rate of induction and decay of death rate in Eq. (3.6)

3.4.4 Chemicals

Doxorubicin was purchased from Sigma Aldrich (St. Louis, MO) and dissolved to a 1 mM stock concentration in sterile saline for subsequent experiments. Tariquidar (TQR) is a third-generation MDR1 inhibitor that non-competitively inhibits MDR1 function (182). TQR is leveraged to modulate doxorubicin pharmacokinetics in the MDA-MB-468$_{MDR1}$ cell line. NU7441 is a DNA-PK inhibitor that has been investigated as a means to improve treatment response to DNA-damaging agents (116,183). NU7441 is used to modulate doxorubicin pharmacodynamics in the SUM-149PT cell line. TQR and NU7441 were both purchased from Selleckchem (Boston, MA). Each was dissolved to a 1 mM stock concentration in DMSO. We subsequently refer to these therapies (TQR and NU7441) as sensitizers. All solutions were stored in 250 µL aliquots at -80 °C.

3.4.5 Doxorubicin Uptake Imaging and Image Processing

Time resolved fluorescent microscopy was employed to characterize the uptake of doxorubicin by each cell line (MDA-MB-468$_{H2B}$, MDA-MB-468$_{MDR1}$, and SUM-149PT) using a modification of the previously-published drug uptake assay (177). The method leverages the intrinsic fluorescence of doxorubicin to quantify the movement of doxorubicin from the extracellular space into cells. Briefly, each cell line was introduced into 96-well microtiter plates at ~10,000 cells per well. Each well was imaged at 20-25 minute intervals *via* fluorescent microscopy (at several wavelengths as described below) with a 20× objective in 2×2 image montages on a BD Pathway 855 Bioimager (BD Biosciences, San Jose, CA). Imaging began one hour prior to and continued for approximately 24 hours following application of 1 µM of doxorubicin. After eight hours, doxorubicin was removed *via* media replacement. To measure the effect of TQR and NU7441 on drug uptake kinetics in the MDA-MB-468$_{MDR1}$ and the SUM-149PT cell lines, respectively, each modulator was applied over a range of concentrations (250 – 2 nM for TQR and 2 µM - 16 nM for NU7441 both *via* a two-fold dilution series) one hour prior to doxorubicin application. At least three replicates of each treatment condition were collected.

To correct for uneven background illumination, the illumination function for each image was first estimated (184). The image is defined:

$$I = L(C + b) ,$$

where I is the image, L is the illumination function, C is signal from cells, and b is the background. The signal from cells is removed from each image through use of a median disc filter with a radius of 50, isolating b. To estimate L, the background-only images in each well are averaged over all timepoints. A smooth surface is fit to this averaged image, and the surface is normalized to a maximum value of 1. Each image in the time series is divided by this surface (L) to correct for uneven illumination. The result of the correction approach is illustrated in Figure 3.2. A threshold-based approach is used to segment each cell. An example segmentation is illustrated in Figure 3.2.

To account for the various fluorophores in the experiment (H2BRFP, MDR1GFP, and doxorubicin), a linear unmixing approach was employed to isolate the signal from each fluorophore to more precisely quantify doxorubicin accumulation (185). The approach leverages spectral imaging data collected at multiple excitation and emission wavelengths to isolate the signal from each fluorophore. This method can also be used for background subtraction by modeling the background (here, the signal from cell culture media) as an additional fluorophore. For these experiments, we define four fluorophores of interest: MDR1GFP, doxorubicin, H2BRFP, and background. The observed images are modeled as a linear combination of the signals from each of these fluorophores:

$$\begin{bmatrix} S_{H2B} & S_{MDR} & S_{Dox} & S_{background} \end{bmatrix} T_{4 \times n} = \begin{bmatrix} I_1 & I_2 & ... & I_n \end{bmatrix},$$

where S_{H2B} is the signal from the H2BRFP, S_{MDR} is the signal from the GFP-tagged MDR1, S_{Dox} is the signal from doxorubicin, and $S_{background}$ is the background signal from cell culture media. T is the transformation matrix that estimates the contribution from each fluorophore in creating each image I. In this work, five images ($n=5$) were collected at each timepoint. The excitation, dichroic, and emission filters for each image are listed in Table 3.2.

Table 3.2. Filter settings

Image	Excitation (nm)	Dichroic (nm)	Emission (nm)
I_1	470/40	515, longpass	515, longpass
I_2	470/40	515, longpass	570, longpass
I_3	470/40	515, longpass	575/25
I_4	470/40	515, longpass	540/50
I_5	548/20	595, longpass	645/75

To construct *T*, images of each fluorophore are collected from control samples. Specifically, control images of GFP, H2BRFP-positive cells, doxorubicin, and background are collected. For each fluorophore, the image with the highest intensity is assumed to be the true image; i.e., the corresponding entry in *T* is set to 1. The relative intensity of the other four images with respect to the true image are then estimated. This normalized spectrum is deposited into the row of *T* corresponding to the current fluorophore. *T* is estimated at each timepoint to compensate for any temporal changes in fluorophore intensity.

With an estimate of *T* and a spectral image set for each well at each timepoint, the underlying signals (i.e., S_{H2B}, S_{MDR}, S_{Dox}, $S_{background}$) can be estimated using QR decomposition (implemented in MATLAB (Natick, MA)). This can be done on a per-pixel basis as shown in Figure 3.2. However, as we are only interested in intracellular and extracellular doxorubicin signals, the average value from each image in the intracellular and extracellular ($I_{i,I}$, $I_{i,E}$) space was calculated using a cell segmentation (as detailed above). Each signal can then be recovered:

$$\begin{bmatrix} S_{H2B,I} & S_{MDR,I} & S_{Dox,I} & S_{background,I} \\ S_{H2B,E} & S_{MDR,E} & S_{Dox,E} & S_{background,E} \end{bmatrix} T_{4 \times n} = \begin{bmatrix} I_{1,I} & \cdots & I_{5,I} \\ I_{1,E} & \cdots & I_{5,E} \end{bmatrix},$$

where $S_{Dox,I}$ and $S_{Dox,E}$ are the signals from doxorubicin in the intracellular and extracellular spaces, respectively. Similar definitions apply for the other signals *S*.

Finally, S_{Dox} is converted into doxorubicin concentration. We assume that doxorubicin signal is linearly proportional to its concentration, [*Dox*] (177):

$$S_{Dox} = a[Dox] + b \ .$$

To calibrate this model, images are collected on a series of wells containing a range of known doxorubicin concentrations. Estimates of *a* and *b* are obtained by fitting the doxorubicin signal equation to these control data.

3.4.6 Doxorubicin Treatment Response Imaging

Using the previously-published dose-response assay, each cell line was treated with a range of doxorubicin concentrations (5000 to 10 nM *via* a two-fold dilution series) for 24 hours as monotherapy. Additionally, the sensitizing effects of TQR and NU7441 in the MDA-MB-468$_{MDR1}$ and the SUM-149PT cell lines, respectively, were investigated by applying those therapies over a

Figure 3.2: Doxorubicin image processing pipeline. Five images of each well at each timepoint are collected. Sample images of I_4 and I_5 at a representative timepoint are shown in a and b, respectively. The uneven illumination of these images is corrected through use of the image illumination function. Corrected images of a and b are shown in c and d, respectively. A linear unmixing approach is employed to estimate the signal from each fluorophore present in the experimental system. Sample reconstructed signals (i.e., S_{Dox}, S_{MDR}, S_{H2B}, and $S_{background}$) are shown in e-h. Cells are segmented *via* a threshold approach (red outline in i and j). The doxorubicin signal in the intracellular space over time can then be extracted from these images (k) and converted into concentration timecourses (l) to be fit by Eqs. (3.1) – (3.3).
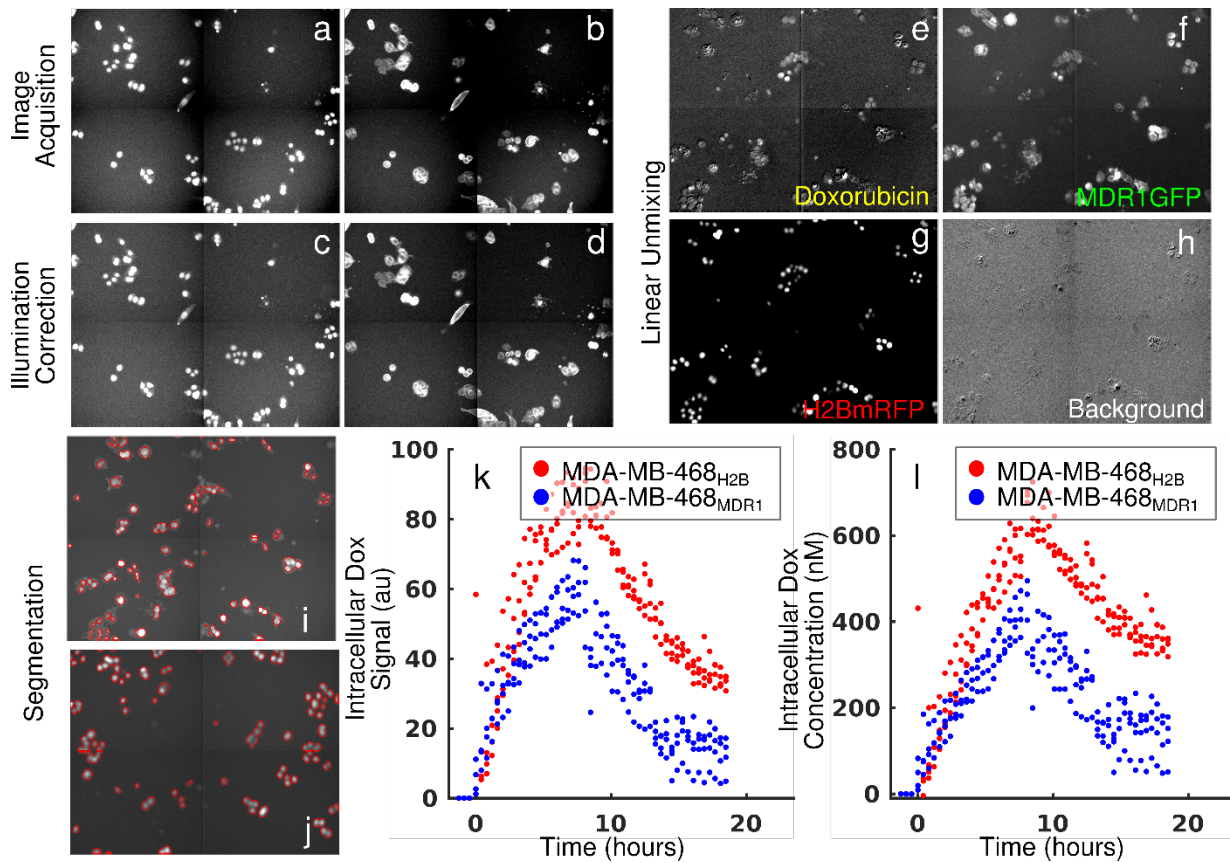
range of concentrations one hour prior to application of doxorubicin. TQR concentrations in a two-fold dilution series from 250 - 2 nM were used for the MDA-MB-468$_{MDR1}$ cell line, and NU7441 concentrations in a two-fold dilution series from 2 μM - 15 nM were used for the SUM-149PT cell line. These combination studies were each performed at three doxorubicin concentrations. All drug (doxorubicin and sensitizer) was removed from each well *via* media replacement at 24 hours. These cells were imaged daily *via* fluorescent microscopy for at least 15 days following treatment. For these studies, fluorescence microscopy images were collected using a Synentec Cellavista High End platform (SynenTec Bio Services, Münster, Germany) with a 20× objective and tiling of 25 images, each collected with 650 ms excitation with 529 nm light and emissions collected at 585 nm. Nuclei were segmented and counted in ImageJ (http://imagej.nih.gov/ij/) using a previously-described, threshold-based method (150) to quantify cell population. Six replicates of each treatment condition were collected. Media was refreshed every 3 days for the duration of each experiment to ensure sufficient growth conditions for surviving cells. Data are manually truncated when the cell population reaches carrying capacity. At this point, the signals from neighboring nuclei overlap, and the cell counting becomes unreliable.

3.4.7 Model Fits

The three-compartment model described in Eqs. (3.1) – (3.3) was fit to the uptake data under each treatment condition (doxorubicin monotherapy and doxorubicin combination with sensitizer) for each cell line using a nonlinear least squares optimization implemented in MATLAB. Of note, each cell line is assumed to have a single set of compartment model parameters (k_{EF}, k_{FE}, and k_{FB}) for each sensitizer concentration (i.e., a parameter set for doxorubicin monotherapy and a set for each sensitizer concentration). Mean errors of the best-fit model across all timepoints are reported.

Similarly, the response model described by Eqs. (3.4) – (3.6) was fit to the dose response data from all treatment conditions (i.e., doxorubicin monotherapy and doxorubicin combination with sensitizer) for each cell line. Each treatment condition in each cell line was fit independently, yielding cell line- and treatment condition-specific parameter values. This was accomplished through a nonlinear least squares optimization implemented in MATLAB. For additional details on the model fitting procedure see (177). We report on the mean percent errors of the best fit models across all timepoints.

Of note, in defining the equivalent dose statistic, the k_{FB} term is a mixed measure of doxorubicin binding and DNA repair. While doxorubicin binding can be measured in the uptake studies above, DNA repair cannot be directly observed in the course of the experiment (we note there exists several methods to assay DNA damage, but these are destructive assays that can only measure DNA damage at a single timepoint (186,187)). For doxorubicin monotherapy, we define k_{FB} as the binding rate of doxorubicin to the nucleus as measured in the uptake studies. To estimate k_{FB} for doxorubicin co-treatment with agents that modulate DNA repair (e.g., NU7441), we leverage the treatment response parameters (i.e., the parameters in Eqs. (3.4) – (3.6)) and the definition of equivalent dose as described below.

We assume, by definition, that a specified equivalent dose elicits a specific treatment response. Conversely, a specified treatment response is summarized by a specific equivalent dose. Accordingly, similar treatment responses should have similar equivalent doses. We use this relationship to estimate the equivalent dose for each co-treatment condition. Specifically, treatment response under all treatment conditions (i.e., doxorubicin monotherapy and co-treatment with a sensitizer) can by summarized by the parameters in Eqs. (3.4) – (3.6) (i.e., $p = [k_{d,a}, \underline{k}_{d,b}, r]$). For doxorubicin monotherapy conditions, the equivalent dose is calculated using the k_{FE}, k_{EF}, and k_{FB} values estimated from the uptake studies. Notably, per the definition of k_{FB} above, the equivalent doses calculated for these doxorubicin monotherapy conditions are perfectly known. The parameters (p) from these doxorubicin monotherapy experiments are then interpolated with respect to equivalent dose. This yields a continuous set of parameters (p^{est}) across all possible equivalent doses in the range from no treatment to maximal doxorubicin dose. The fit parameter values (p) for each of the m co-treatment conditions are then matched to the interpolated parameters from the doxorubicin-only treatment condition (p^{est}) to estimate the expected equivalent dose (D_{est}). Specifically, D_{est} is the set of equivalent doses corresponding to the interpolated parameter set (p^{est}) that best matches the fit parameter values from each co-treatment condition (i.e., $\min \left\| p^{est} - p \right\|_2$). This process is illustrated in Figure 3.3. The following constrained objective function, $G(k_{FB})$, can then be used to estimate k_{FB} for each of the n sensitizer concentrations:

$$\min_{k_{FB}} G\left(k_{FB}\right) = \sum_{i=1}^{m} \left(D_{est,i} - D_i\right)^2$$
$$s.t. \quad k_{FB,q+1} - k_{FB,q} \geq 0 \quad \forall \ q = [1,...,n] \tag{3.7}$$

Figure 3.3: Calculating D_{est}. The treatment response model is fit to all data (doxorubicin monotherapy and co-treatment), yielding a set of parameters, $p = [k_{d,a}, k_{d,b}, r]$, for each treatment condition. These parameters are plotted against equivalent dose (D_{eq}), as calculated with the k_{EF}, k_{FE}, and k_{FB} parameters derived from the uptake studies. The black points are taken from the doxorubicin monotherapy conditions. The data in red, blue, and green represent data from three experiments each with a unique, fixed doxorubicin concentration and variable sensitizer concentrations. To optimize k_{FB} for each sensitizer concentration, the equivalent dose for each co-treatment condition is first estimated using the doxorubicin-only treatment condition parameters (with perfectly-known D_{eq}) as follows. We hypothesize that the all treatment responses, as quantified by the parameters p, should fall along a smooth continuum. Accordingly, the parameter fits from co-treatment conditions are mapped to the doxorubicin-only treatment (right-facing arrows), and the estimated dose (D_{est}) is the equivalent dose that corresponds to the match (down-facing arrows). Notably, we assume a unique value for k_{FB} for each sensitizer concentration. Parameters from a single sensitizer concentration at multiple doxorubicin doses are circled below.
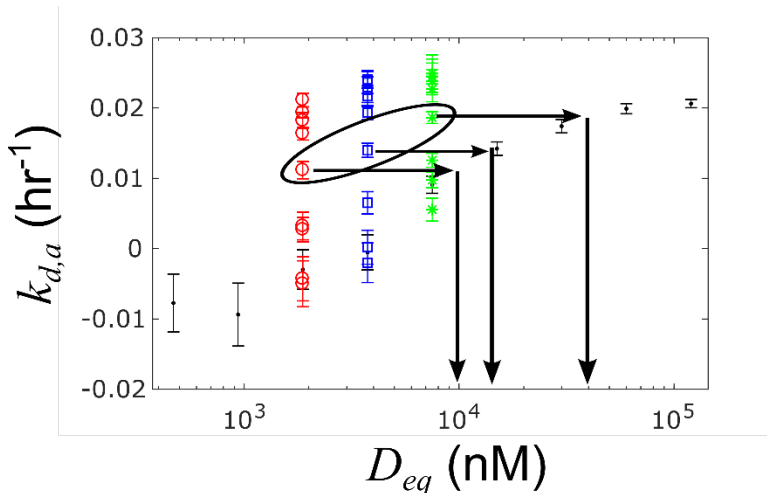
where the D_i is the equivalent dose for each co-treatment condition as described below and $D_{est,i}$ is the expected equivalent dose for each co-treatment condition as described above. The equivalent dose for each co-treatment condition, D_i, is calculated as described in Section 3.4.2. Specifically, in calculating D_i, we use the k_{EF} and k_{FE} values measured from uptake studies and the optimized k_{FB} value corresponding to the sensitizer concentration in the co-treatment condition. This objective function matches parameter fits from co-treatment conditions to those from doxorubicin-only treatments. The constraints in the objective function ensure that k_{FB} increases monotonically with sensitizer concentration. This objective function was minimized *via* a constrained optimization routine implemented in MATLAB.

To validate this approach of inferring cellular properties from population-level treatment response measurements, we repeat the above approach to estimate varying doxorubicin efflux parameters in the MDA-MB-468$_{MDR1}$ cell line under treatment with TQR. Specifically, we use values for k_{EF} and k_{FB} measured from the uptake assay, and we assume the k_{EF} value measured in the uptake study under doxorubicin monotherapy is perfectly known. Values of k_{FE} for each TQR concentration are then optimized in the same way as k_{FB}. The optimized values are compared to those experimentally measured in the uptake assay.

3.4.8 Comparison of Cell Lines with Equivalent Dose

As the MDA-MB-468$_{MDR1}$ line was engineered from the MDA-MB-468$_{H2B}$ line, we hypothesize that the response of these cell lines is not significantly different when compared *via* equivalent dose. Indeed, the proposed equivalent dose metric was developed to account for the differing pharmacokinetic properties between these cell lines to more precisely compare their respective responses to therapy. Specifically, cell survival 3 days following treatment of the parental MDA-MB-468$_{H2B}$ cell line is compared to that of the MDA-MB-468$_{MDR1}$ cell line when the varying pharmacokinetic properties are normalized using D_{eq} calculated with cell-line specific k_{EF}, k_{FE}, and k_{FB} values. For comparison with previous assays, we report the EC_{50} for each of these cell lines as measured *via* extracellular doxorubicin concentration and equivalent dose.

3.5 Results

3.5.1 Treatment Response in MDA-MB-468$_{MDR1}$ Line

The measured intracellular doxorubicin concentration timecourses for the MDA-MB-468$_{MDR1}$ cell line under doxorubicin monotherapy and combination therapy with TQR are shown in Figure 3.4. Intracellular doxorubicin increases with increases in TQR concentration. The average intracellular concentration over the last 10 timepoints is significantly different among the treatment groups (one-way ANOVA, $p < 1e-5$). Eqs. (3.1) – (3.3) are fit to these data, and the best fit model is overlaid on the timecourses. The mean error of the best fit pharmacokinetic model was 45.6 nM across all treatment conditions, and the corresponding model parameters are shown in Figure 3.4. Increasing TQR concentrations decrease doxorubicin efflux in the MDA-MB-468$_{MDR1}$ cell line in a dose-dependent manner. For example, the efflux rate is decreased from 0.216 ($\pm$0.028) hr^{-1} to 0.046 ($\pm$0.008) hr^{-1} as TQR increases from 2 nM to 250 nM (the bounds here and below correspond to the 95% confidence interval of the parameter estimates). Similar values of k_{EF} were observed across all TQR concentrations, ranging from [1.63, 3.46] $\times10^{-6}$ hr^{-1}.

Treatment response timecourses of the MDA-MB-468$_{MDR1}$ line to doxorubicin monotherapy are shown in Figure 3.5. Eqs. (3.4) – (3.6) are fit to these data, and the best fit models are overlaid on the observed cell counts. The mean percent error of the best fit model across all treatment conditions is 10.26%. The MDA-MB-468$_{MDR1}$ line demonstrated a proliferation rate (k_p) of 2.12 ($\pm$0.03) $\times10^{-2}$ hr^{-1}. A graded dose response to doxorubicin was observed, and this response is quantified by the parameters in Figure 3.5. Treatment response timecourses with accompanying best-fit model overlays under co-treatment with TQR are shown in Figure 3.6. For a fixed concentration of doxorubicin, increasing concentrations of TQR increases the sensitivity of the cell line to treatment. For example, at a fixed dose of 156 nM doxorubicin, increasing the TQR concentration from 0 to 250 nM increased the death rate ($k_{d,a}$) from -0.16 ($\pm$0.23) $\times10^{-2}$ hr^{-1} to 2.21 ($\pm$0.1) $\times10^{-2}$ hr^{-1}. TQR monotherapy did not affect the growth of these cells as shown in Figure 3.7. Notably, high variance in parameter estimates is observed as values of r approach 0.05 hr^{-1} and values of $k_{d,b}$ approach 0 hr^{-1}. There exists intrinsic uncertainty at this limit as the rapid dynamics (r) coupled with small $k_{d,b}$ effects cannot be resolved by the current data. This uncertainty in r for small $k_{d,b}$ does not affect model predictions as demonstrated by a sensitivity analysis in previous work (177).

As similar values of k_{EF} and k_{FB} were observed in fitting the TQR uptake curves and TQR is a specific inhibitor of MDR1, we hypothesized that its effects are limited to k_{FE}. The uptake data were re-analyzed fixing k_{EF} and k_{FB} across all TQR concentrations and allowing k_{FE} to vary as a

Figure 3.4: Doxorubicin uptake in MDA-MB-468$_{MDR1}$ under doxorubicin combination therapy with TQR. The mean intracellular concentrations with corresponding standard deviations are shown throughout the course of the uptake study for each treatment condition in a. Doxorubicin accumulation increases with increasing concentrations of TQR. Eqs. (3.1) – (3.3) were fit to the data, and the best fit models are overlaid on the data (smooth lines) in a. Model parameter fits corresponding to the best fits models are shown in b-d. The control data (0 nM TQR) is shown in red. Similar k_{EF} and k_{FB} vales are observed across all TQR concentrations. There is a trend of decreasing k_{FE} values with increasing TQR concentrations, consistent with MDR1 inhibition by TQR.
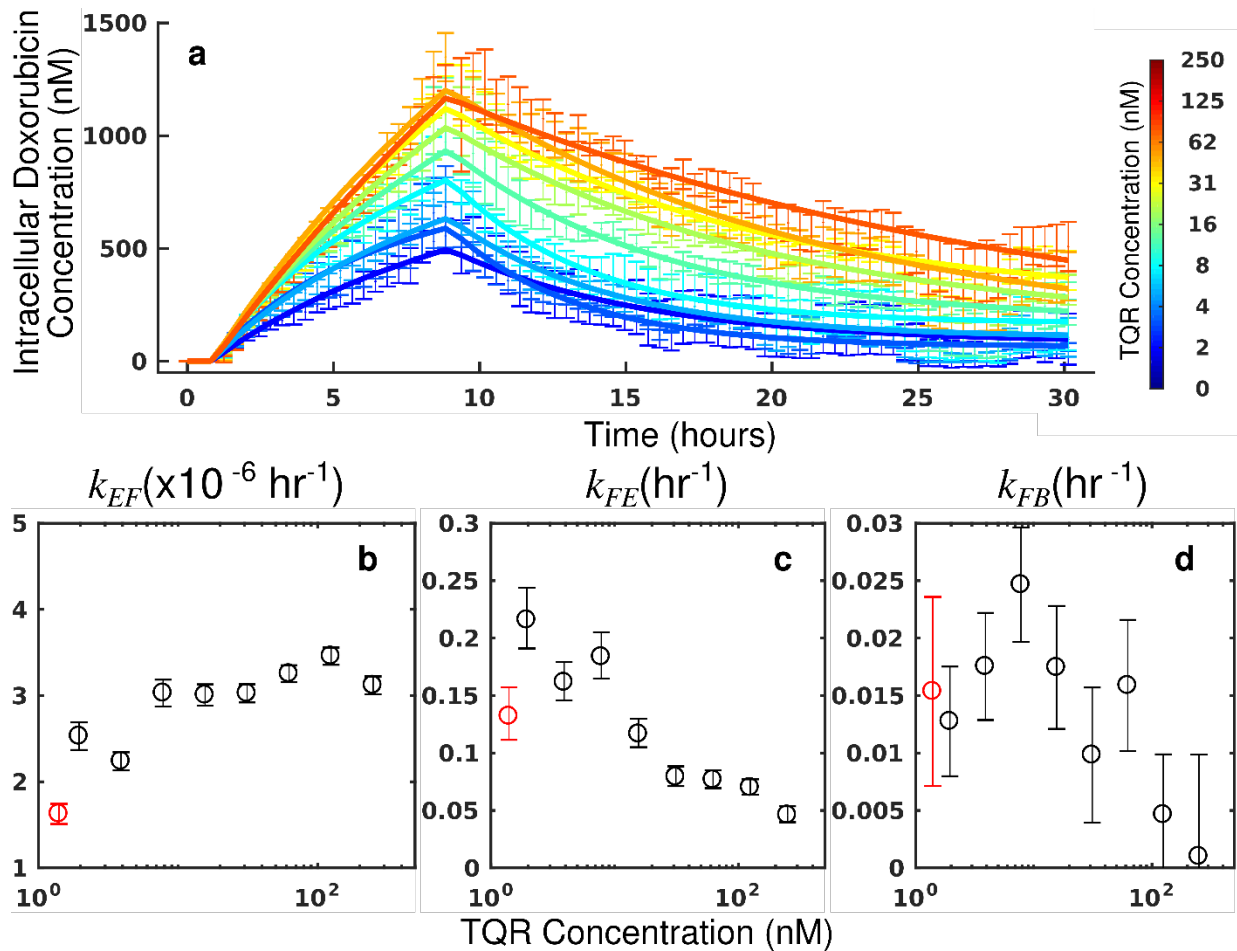
Figure 3.5: Treatment response in MDA-MB-468$_{MDR1}$ cell line under doxorubicin monotherapy. The top plot shows cell counts over time from treatment response studies. For these studies, cells were treated with a fixed concentration of doxorubicin for 24 hours. These counts are fit to Eqs. (3.4) - (3.6) as described in Section 3.4.7, and the best fit model is overlaid on the cell counts (smooth lines in top panel). The model fits and cell counts are color-coded to reflect the varying doxorubicin concentrations used. Error bars represent the 95% CI from six experimental replicates for each treatment condition. Model parameters with corresponding 95% CI are shown in the bottom row as a function of doxorubicin concentration. For each doxorubicin concentration, the death rate ($k_{d,a}$ and $k_{d,b}$) increased with increasing doxorubicin concentrations.
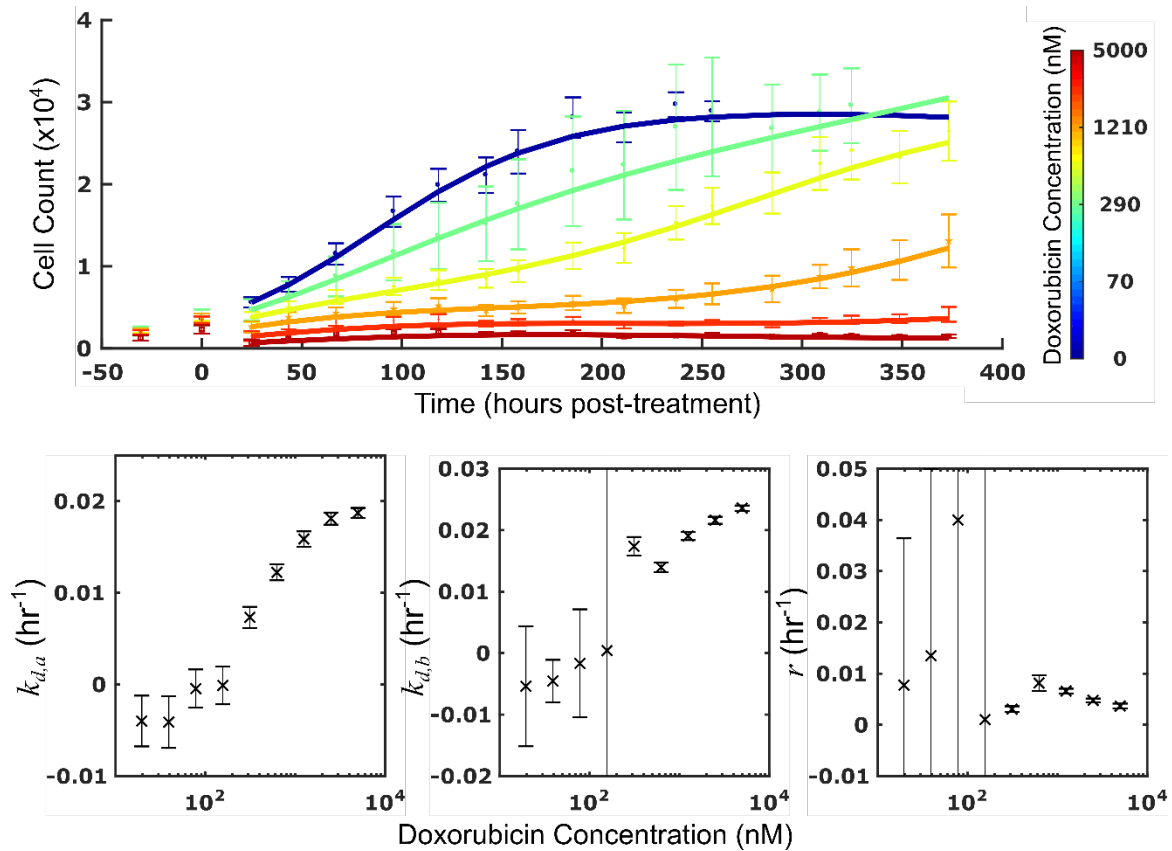
Figure 3.6: Treatment response in MDA-MB-468$_{MDR1}$ cell line under combination therapy with doxorubicin and TQR. The top row shows cell counts over time from treatment response studies. In each plot, a fixed concentration of doxorubicin is applied with variable TQR concentrations. These counts are fit to Eqs. (3.4) - (3.6) as described in Section 3.4.7, and the best fit model is overlaid on the cell counts (smooth lines in top panels). The model fits and cell counts are color-coded to reflect the varying TQR concentrations used. Error bars represent the 95% CI from six experimental replicates for each treatment condition. Model parameters with corresponding 95% CI are shown in the bottom row as a function of TQR concentration. Data are color-coded to reflect the doxorubicin concentration used. For each doxorubicin concentration, the death rate ($k_{d,a}$ and $k_{d,b}$) increased with increasing TQR concentrations.
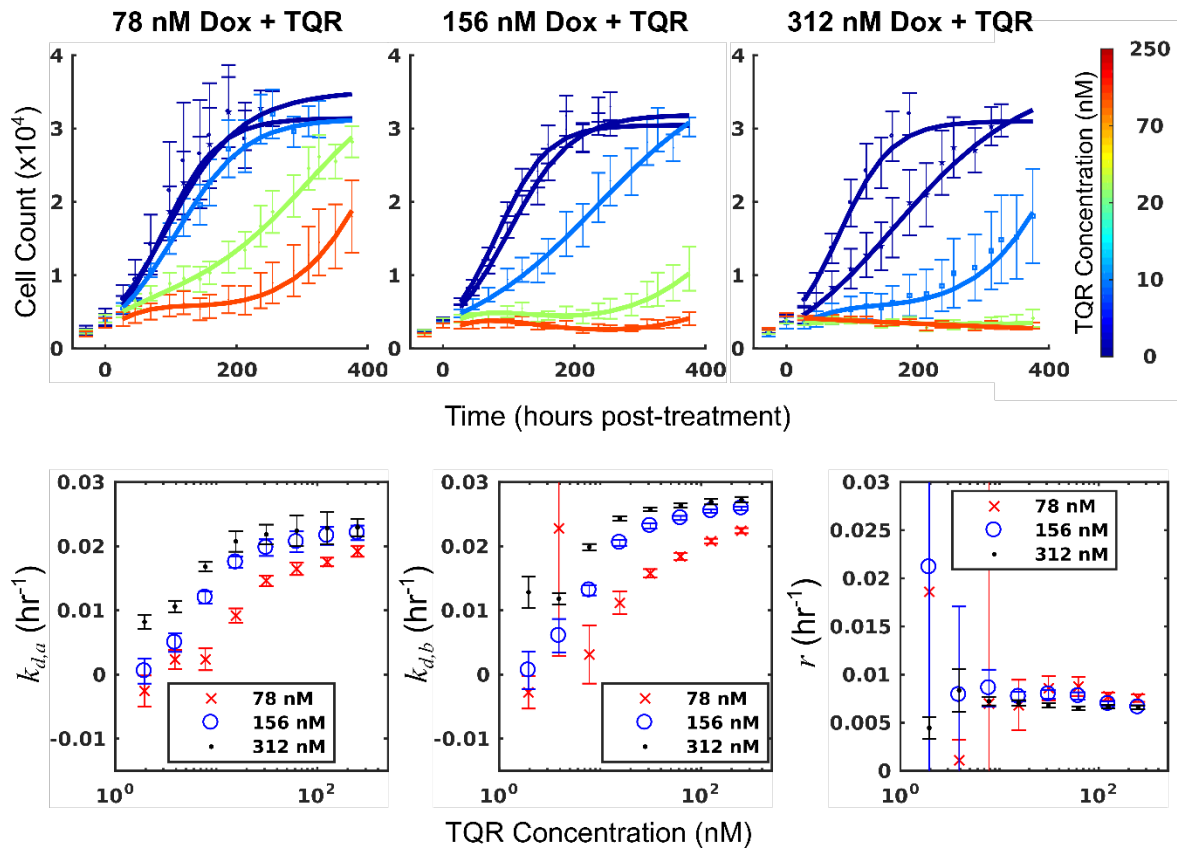
Figure 3.7: TQR-only and NU7441-only control data for the MDA-MB-468$_{MDR1}$ and SUM-149PT cell line, respectively. Cell count data with corresponding standard deviations over time under treatment with a range of TQR and NU7441 demonstrate that no significant difference in cell counts under monotherapy with either TQR or NU7441. The effect of these therapies is limited to co-treatment with doxorubicin.
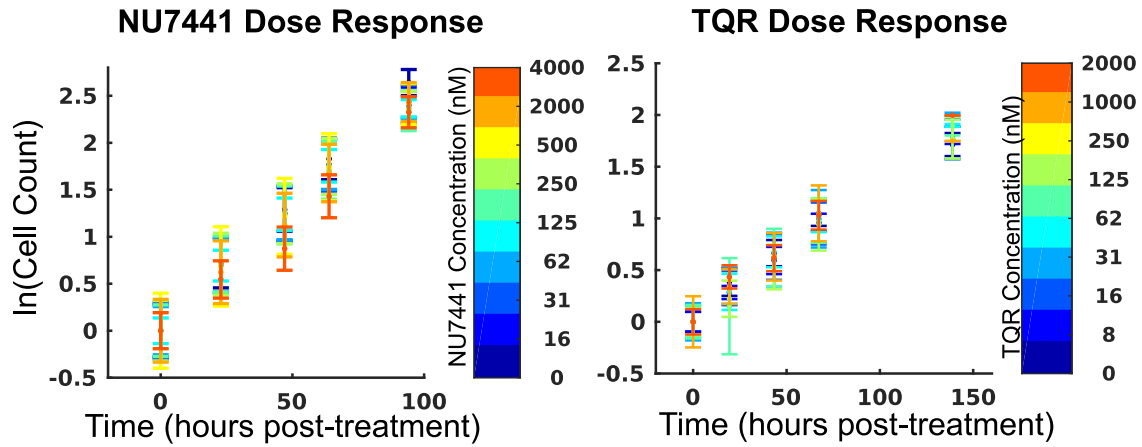
function of TQR. The mean error for this fit to the MDA-MB-468$_{MDR1}$ uptake data was 95.9 nM. Under this assumption, k_{EF} and k_{FE} were measured to be 3.08 ×10^{-6} hr^{-1} and 0.0212 hr^{-1} across all TQR concentrations, respectively. The k_{FE} value for doxorubicin monotherapy was 0.313 hr^{-1}. The equivalent dose statistic was calculated for all treatment conditions in the MDA-MB-468$_{MDR1}$ cell line. For these calculations, the k_{FE} value for each TQR concentration was estimated with the optimization routine outlined in section 3.4.7, and the k_{EF} and k_{FB} values were fixed to the values reported above. The optimized k_{FE} values for each TQR concentration are shown in Figure 3.8. Decreasing k_{FE} values are observed with increasing TQR concentrations, matching the measurements from the uptake studies in Figure 3.4. The equivalent dose can describe all treatment conditions with a single statistic that is predictive of response (Figure 3.8). When response model parameters (i.e., $k_{d,a}$, $k_{d,b}$, and r) from all treatment conditions (doxorubicin monotherapy and combination therapy) are plotted as a function of equivalent dose, they fall along a single, smooth path. The response of the MDA-MB-468$_{MDR1}$ cell line is a function of D_{eq}.

3.5.2 Treatment Response in SUM-149PT Line

The measured intracellular doxorubicin concentration timecourses for the SUM-149PT cell line under doxorubicin monotherapy and combination therapy with NU7441 are shown in Figure 3.9. Eqs. (3.1) – (3.3) are fit to these data, and the best fit model is overlaid on the timecourses. The corresponding model parameters are shown in Figure 3.9. The mean error of the best fit pharmacokinetic model was 90.9 nM across all treatment conditions and timepoints. NU7441 does not affect intracellular doxorubicin accumulation. Comparing the intracellular doxorubicin concentration over the last 10 timepoints among all sensitizer concentrations, no significant difference is observed at the $p = 0.05$ significance level (one-way ANOVA). Further, similar values of k_{FE}, k_{EF}, and k_{FB} are observed across all NU7441 concentrations. Of note, the 95% CI's are particularly large for k_{FE} as the brightest cells in each well are often removed along with doxorubicin at 8 hours, causing an artificially high decrease in intracellular doxorubicin accumulation following treatment.

Treatment response timecourses of the SUM-149PT line to doxorubicin monotherapy are shown in Figure 3.10. Eqs. (3.4) – (3.6) are fit to these data, and the best fit models are overlaid on the observed cell counts. The mean percent error of the best fit model across all treatment conditions is 11.92%. The SUM-149PT line demonstrated a proliferation rate (k_p) of

Figure 3.8: Treatment response in the MDA-MB-468$_{MDR1}$ cell line varies smoothly as a function of equivalent dose. TQR impairs the function of the MDR1 pump, decreasing doxorubicin efflux. Subsequently, we hypothesized the effect of TQR is limited to the k_{FE} parameter (a). Significant differences were observed in doxorubicin accumulation under treatment with TQR (b). The colors from blue to red represent increasing TQR concentrations. Estimates of k_{FE} were obtained through the optimization routine in Section 3.4.7, and optimized k_{FE} are plotted as a function of TQR concentration in panel c. Model parameters from all treatment conditions (doxorubicin monotherapy and co-treatment with TQR) are plotted as a function of equivalent dose in d-f. The black points are from the doxorubicin monotherapy experiments. The red, green, and blue points are from combination experiments with 78 nM, 156 nM, and 312 nM doxorubicin, respectively. Note that parameter values vary smoothly as a function of equivalent dose (D_{eq}). The treatment response from a subset of treatment conditions is shown in panels g-i. These plots are color-coded by the equivalent dose describing each treatment condition. Similar colors demonstrate similar timecourses. Similar treatment response timecourses are observed across different doxorubicin monotherapy and co-treatment conditions. The equivalent dose can describe all monotherapy and co-treatment conditions with a single statistic that is predictive of response.
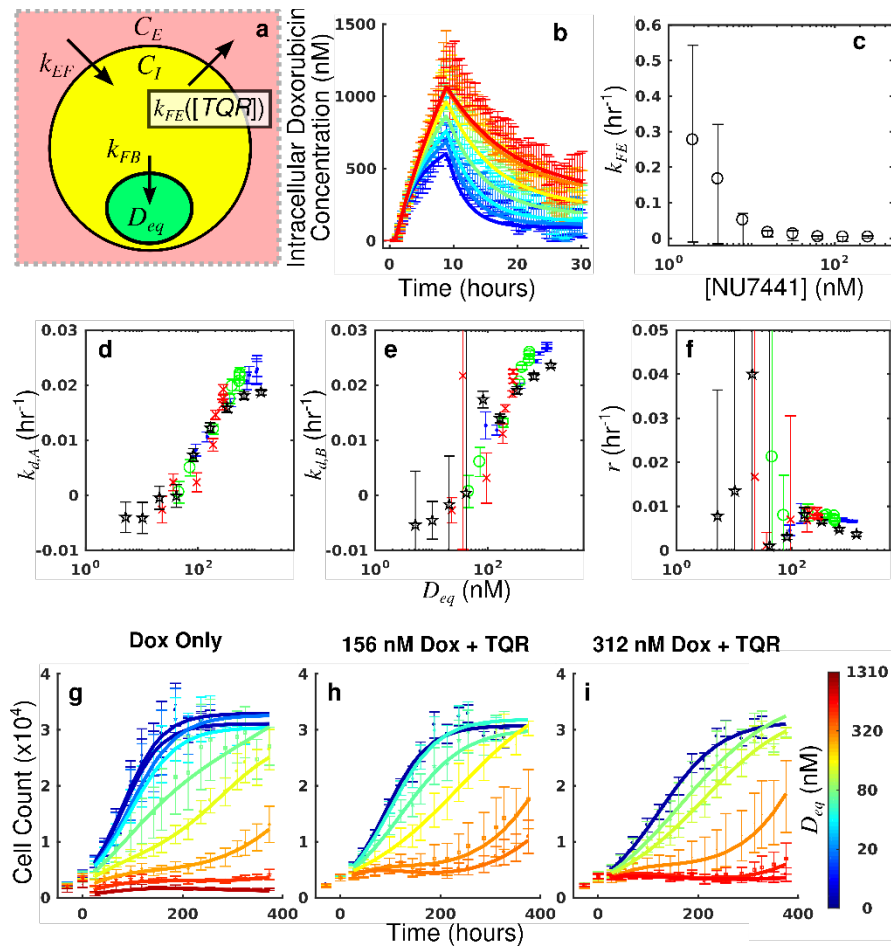
2.58 ($\pm$0.03) $\times$ 10^{-2} hr^{-1}. A graded dose response to doxorubicin was observed, and this response is quantified by the parameters in Figure 3.10. Treatment response timecourses with accompanying best-fit model overlays under doxorubicin co-treatment with NU7441 are shown in Figure 3.11. For a fixed concentration of doxorubicin, increasing concentrations of NU7441 increased the sensitivity of the cell line to doxorubicin. For example, with a fixed dose of 156 nM doxorubicin, NU7441 concentrations increased the death rate ($k_{d,a}$) from 0.25 ($\pm$0.16) $\times$ 10^{-2} hr^{-1} to 2.00 ($\pm$0.06) $\times 10^{-2}$ hr^{-1}. Notably, NU7441 as monotherapy did not affect the growth of these cells as shown in Figure 3.7.

The equivalent dose statistic was calculated for all treatment conditions in the SUM-149PT cell line. The k_{FB} value for each NU7441 concentration was estimated with the optimization routine outlined in section 3.4.7. Notably, as similar concentrations were observed in the uptake studies, k_{EF} and k_{FE} were fixed to 4.00 $\times 10^{-6}$ hr^{-1} and 0.165 hr^{-1} for all NU7441 concentrations, respectively. For doxorubicin monotherapy, k_{FB} was set to 0.236 hr^{-1}. These were calculated by fitting the SUM-149PT uptake studies assuming constant parameters for all NU7441 concentrations. The mean error for this fit to the SUM-149PT uptake data was 68.5 nM. Increasing k_{FB} values are observed with increasing NU7441 concentrations (Figure 3.12). We attribute k_{FB} values smaller than the doxorubicin monotherapy to experimental error. In these cases, the effect of treatment is small (death rates near 0 hr^{-1}). The equivalent dose can describe all treatment conditions with a single statistic that is predictive of response. When response model parameters (i.e., $k_{d,a}$, $k_{d,b}$, and r) from all treatment conditions (doxorubicin monotherapy and combination therapy) are plotted as a function of equivalent dose, they fall along a single, smooth path. The response of the SUM-149PT cell line is a function of D_{eq}.

3.5.3 Comparison of MDA-MB-468$_{MDR1}$ and MDA-MB-468$_{H2B}$

The measured intracellular doxorubicin concentration timecourses with accompanying best-fit models for the MDA-MB-468$_{H2B}$ and MDA-MB-468$_{MDR1}$ are shown in Figure 3.13. Decreased doxorubicin accumulation was observed in the MDA-MB-468$_{MDR1}$ cell line relative to its parental line, MDA-MB-468$_{H2B}$. Notably, the drug efflux was significantly elevated in the MDA-MB-468$_{MDR1}$ line relative to its parental line with k_{EF} values of 1.01($\pm$0.08) $\times$ 10^{-1} hr^{-1} and 0.52 ($\pm$0.04) $\times$ 10^{-1} hr^{-1}, respectively ($p < 0.05$). The mean errors of the best fit pharmacokinetic

Figure 3.9: Doxorubicin uptake in SUM-149PT under doxorubicin combination therapy with NU7441. The mean intracellular concentrations with corresponding standard deviations are shown throughout the course of the uptake study for each treatment condition in a. No significant difference in doxorubicin accumulation was observed as a function of NU7441 concentration. Eqs. (3.1) – (3.3) were fit to the data, and the best fit models are overlaid on the data (smooth lines) in a. Model parameter fits corresponding to the best fits models are shown in b-d. The control data (0 nM NU7441) is shown in red. For each model parameter, similar vales were observed across all NU7441 concentrations, consistent with the similar intracellular doxorubicin timecourses in a.

Figure 3.10: Treatment response in SUM-149PT cell line under doxorubicin monotherapy. The top plot shows cell counts over time from treatment response studies. For these studies, cells were treated with a fixed concentration of doxorubicin for 24 hours. These counts are fit to Eqs. (3.4) - (3.6) as described in Section 3.4.7, and the best fit model is overlaid on the cell counts (smooth lines in top panels). The model fits and cell counts are color-coded to reflect the varying doxorubicin concentrations used. Error bars represent the 95% CI from six experimental replicates for each treatment condition. Model parameters with corresponding 95% CI are shown in the bottom row as a function of doxorubicin concentration. For each doxorubicin concentration, the death rates ($k_{d,a}$ and $k_{d,b}$) increased with increasing doxorubicin concentrations.
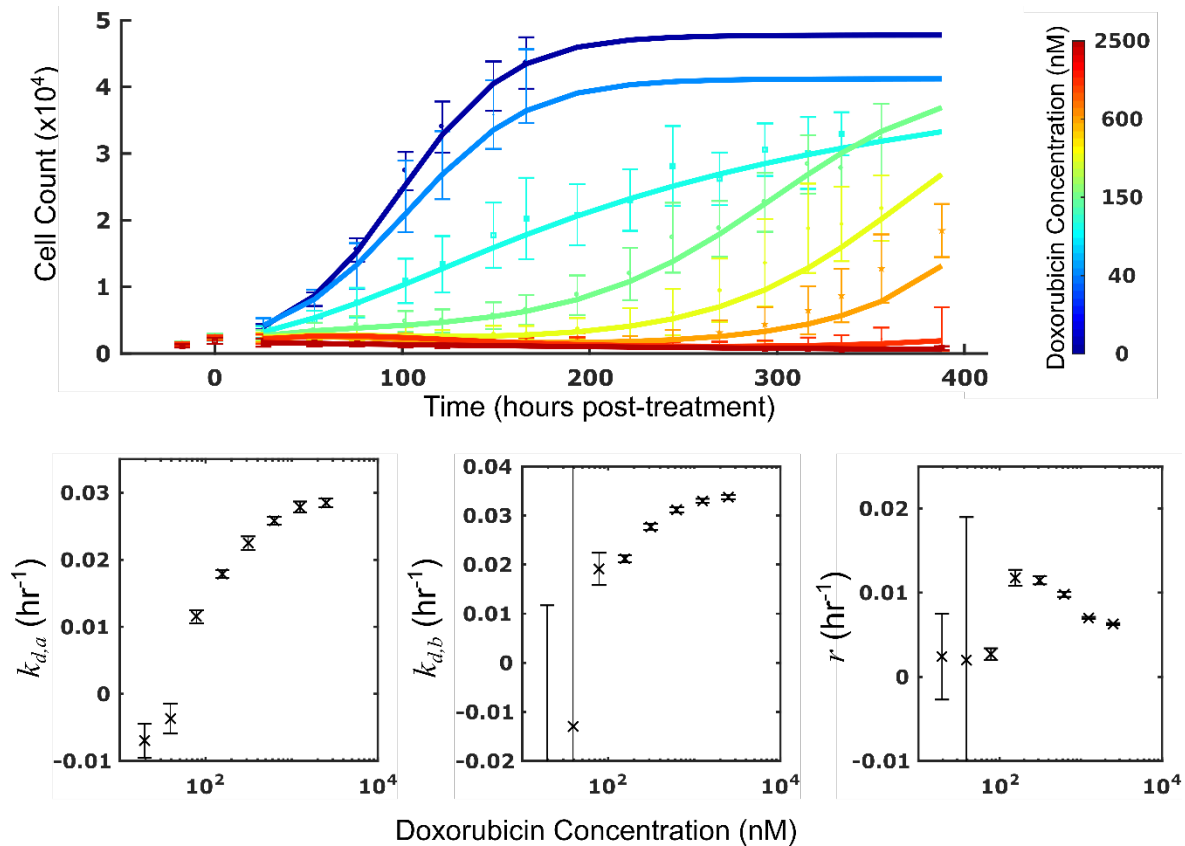
Figure 3.11: Treatment response in SUM-149PT cell line under combination therapy with doxorubicin and NU7441. The top row shows cell counts over time from treatment response studies. In each plot, a fixed concentration of doxorubicin is applied with variable NU7441 concentrations. These counts are fit to Eqs. (3.4) - (3.6) as described in Section 3.4.7, and the best fit model is overlaid on the cell counts (smooth lines in top panels). The model fits and cell counts are color-coded to reflect the varying NU7441 concentrations used. Error bars represent the 95% CI from six experimental replicates for each treatment condition. Model parameters with corresponding 95% CI are shown in the bottom row as a function of NU7441 concentration. Data are color-coded to reflect the doxorubicin concentration used. For each doxorubicin concentration, the death rate ($k_{d,a}$) increased with increasing NU7441 concentrations.
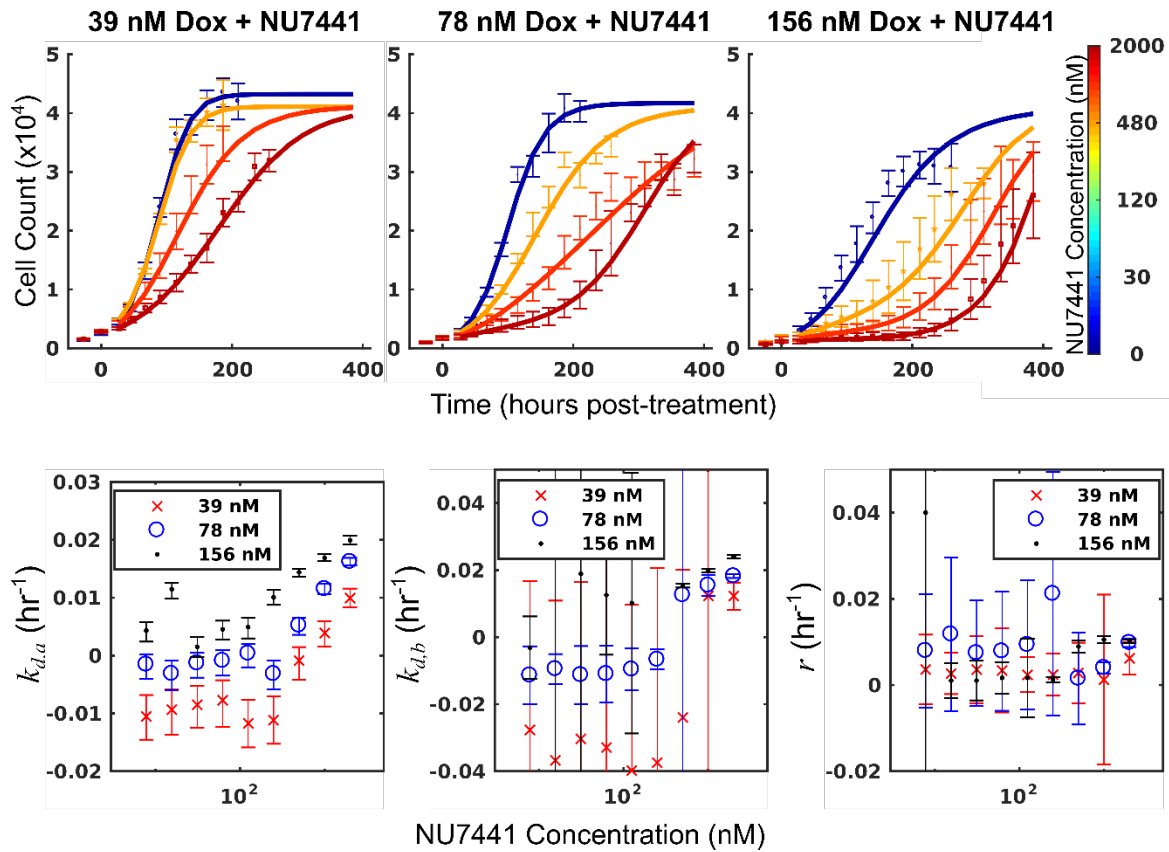
Figure 3.12: Treatment response in the SUM-149PT cell line varies smoothly as a function of equivalent dose. NU7441 impairs the DNA damage response in the SUM-149PT cell line. Subsequently, we hypothesized the effect of NU7441 is limited to the k_{FB} parameter (a). No significant difference is observed in doxorubicin accumulation under treatment with NU7441 (b). The colors from blue to red represent increasing NU7441 concentrations. Estimates of k_{FB} were obtained through the optimization routine in Section 3.4.7, and optimized k_{FB} are plotted as a function of NU7441 concentration in panel c. Model parameters from all treatment conditions (doxorubicin monotherapy and co-treatment with NU7441) are plotted as a function of equivalent dose in d-f. The black points are from the doxorubicin monotherapy experiments. The red, green, and blue points are from combination experiments with 39 nM, 78 nM, and 156 nM doxorubicin, respectively. Note that parameter values vary smoothly as a function of equivalent dose (D_{eq}). The treatment response from a subset of treatment conditions is shown in panels g-i. These plots are color-coded by the equivalent dose describing each treatment condition. Similar colors demonstrate similar timecourses. Similar treatment response timecourses are observed across different doxorubicin monotherapy and co-treatment conditions. The equivalent dose can describe all monotherapy and co-treatment conditions with a single statistic that is predictive of response.
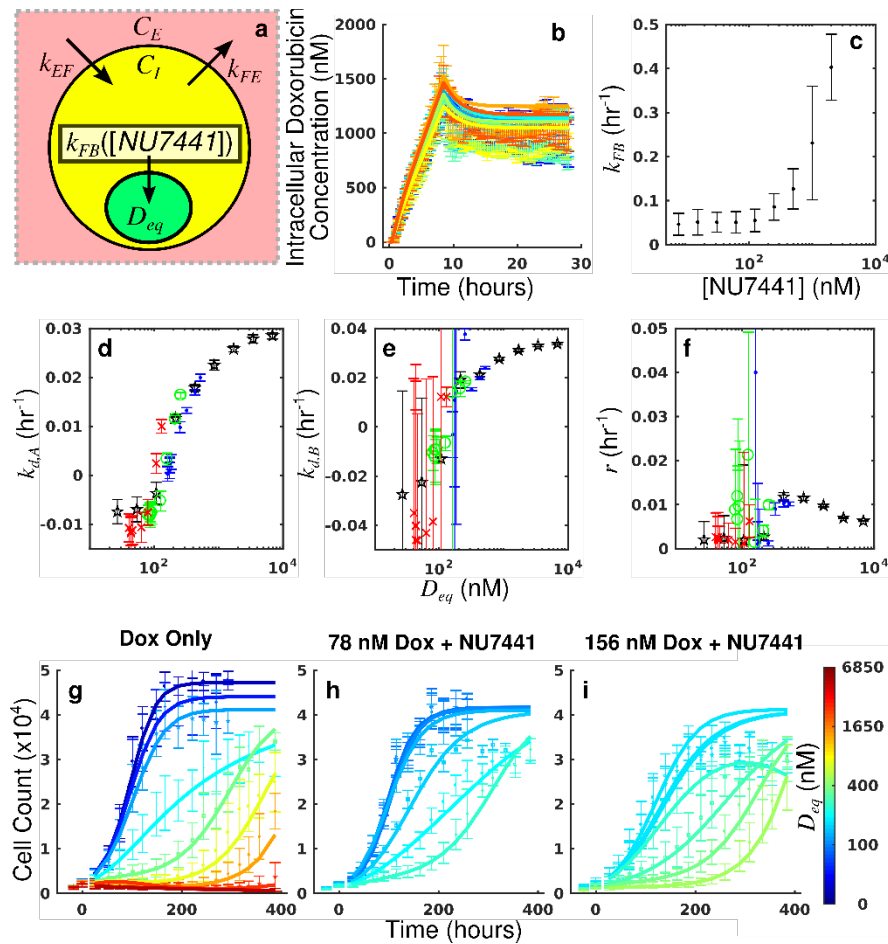
models across all timepoints were 44.7 nM and 58.7 nM for the MDA-MB-468$_{H2B}$ and the MDA-MD-468$_{MDR1}$ lines, respectively.

The survival of each cell line three days following treatment is compared as a function of extracellular doxorubicin concentration and equivalent dose in Figure 3.13. The EC_{50} as measured with the extracellular doxorubicin concentration for the MDA-MB-468$_{H2B}$ and the MDA-MB-468$_{MDR1}$ are 101.6 ($\pm$28.9) nM and 350.6 ($\pm$109) nM, respectively. These measures indicate that there is a significant difference between these cell lines ($p < 0.05$). The EC_{50} as measured with the equivalent dose for the MDA-MB-468$_{H2B}$ and the MDA-MB-468$_{MDR1}$ lines are 53.3 ($\pm$15.1) nM and 93.7 ($\pm$29.2) nM, respectively. These values are not statistically significant at $p = 0.05$, indicating the similarity of these lines.

3.6 Discussion

We have proposed and demonstrated the utility of equivalent dose to normalize for variable cell line pharmacologic properties. With the data presented here, we show that a mechanistic mathematical model of treatment response can succinctly summarize a range of treatments to allow for more precise comparison of treatment response among cell lines. Further, we have shown how this model provides biological insight into the biochemical drivers of treatment response. In summary, we have demonstrated that cancer cell populations behave in consistent, predictable ways and this behavior can be summarized by a parsimonious mathematical model. Just as anticancer therapeutics can be precisely selected using tumor genotypes, these results provide evidence that the dosing of those agents can be precisely tuned to match tumor properties.

Treatment response is driven by cell-line specific pharmacologic properties. To more effectively advance the study of treatment response, assays that explicitly consider this variability are needed to more precisely identify biological drivers of treatment response. While previous treatment response assays provide insight in the relative sensitivity of a cell line to therapy (176), the proposed approach identifies and quantifies specific drivers of treatment sensitivity. Future work includes investigating the biological factors that influence each component of the model. MDR1 is only one factor that can modulate doxorubicin pharmacokinetics just as DNA-PK is only a single protein involved in doxorubicin pharmacodynamics. Through the approach proposed in this work, these pharmacologic properties can be quantified using population-level observations

Figure 3.13: Comparison of MDA-MB-468$_{H2B}$ and MDA-MB-468$_{MDR1}$ cell lines using equivalent dose. The doxorubicin uptake with 95% CI in each cell line is shown in a. The MDA-MB-468$_{H2B}$ demonstrates increased intracellular accumulation of doxorubicin relative to the MDA-MB-468$_{MDR1}$ line. Eqs. (3.1) – (3.3) are fit to the doxorubicin uptake data, and the best fit model is overlaid on the data in a (smooth line). The corresponding parameters with 95% CI are shown in b-d. The MDA-MB-468$_{H2B}$ data are shown in red, and the MDA-MB-468$_{MDR1}$ data are shown in blue. Notably, the efflux of drug from the MDA-MB-468$_{MDR1}$ (k_{FE}) line is significantly greater than the corresponding rate in the MDA-MB-468$_{H2B}$ line ($p < 0.05$). Treatment response is traditionally summarized by cell survival and plotted against applied drug concentration. The cell count relative to control for each cell line is shown as a function of extracellular doxorubicin concentration and equivalent dose in e and f, respectively. While a significant difference is observed when comparing these cell lines *via* extracellular EC_{50}, no significant difference is observed when comparing this statistic derived from the equivalent dose. The equivalent dose can account for the differing pharmacokinetic properties to reveal similar doxorubicin pharmacodynamics in these cell lines.
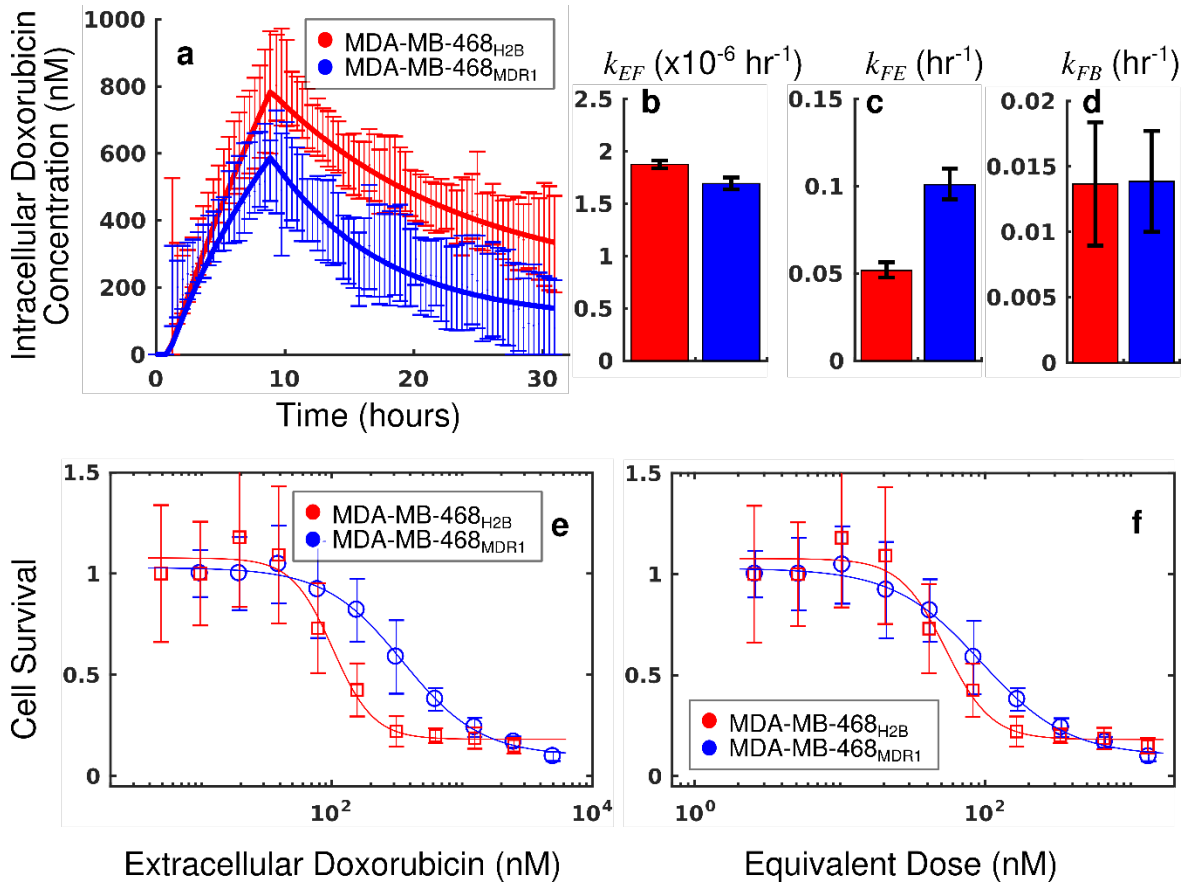
of treatment response. We hypothesize that biomarker discovery approaches will be more successful when confounding pharmacokinetic and pharmacodynamics effects are normalized through the use of the equivalent dose.

Therapies that target PK/PD pathways offer the potential to sensitize cells to genotoxic therapies, increasing the efficacy of therapy and allowing for lower doses of such therapeutics. The approach proposed in this work provides a means to quantify the respective contributions of each PK/PD pathway, providing mechanistic insight into treatment response. Specifically, we quantified the effect of TQR and NU7441 in modulating doxorubicin response. This approach stands in contrast to previous approaches proposed to describe synergy of therapies when used in combination, such as the combination index (188,189). While these methods provide insight into the extent to which treatments synergize, such metrics are not designed to provide guidance on how these therapies can be precisely applied. While therapeutic approaches intended to sensitize tumors to doxorubicin have demonstrated great preclinical activity, their efficacy has been limited in clinical trials. Specifically, negative results have been seen with TQR due to excess toxicities and inactivity (112,113). Similarly, DNA-PK inhibitors such as NU7441 have yet to demonstrate an effect clinically despite their preclinical promise(114–116). We hypothesize that the proposed modeling framework can be used to identify more effective strategies for dosing and assessing these therapeutics. In particular, the proposed modeling approach can provide *precise* guidance on the necessary dose adjustments to maximize efficacy while limiting toxicities. While realizing this goal will require a more complete model of treatment response (i.e., one that incorporates plasma pharmacokinetics and organ system toxicities), we have demonstrated the proposed model to be robust to various doxorubicin treatments and is general to sensitizing agents. For example, as demonstrated in this work, MDR1 pumps do confer resistance to doxorubicin therapy. However, when normalizing for the increased efflux of drug *via* the equivalent dose, the dose-response curve of the MDR1 over-expressing cell line is not significantly different from that of its parental line. Potentially, there is a window in which doxorubicin dose can be decreased in the presence of MDR1 expression treated with TQR therapy that will confer a benefit to the patient while theoretically decreasing off-target toxicities. The mechanistic framework used in this work, expanded to account for off-target toxicities, will provide precise guidelines to the optimal dose adjustments needed when doxorubicin is used in combination with agents that modulate pharmacological properties.

This work is limited by its use of doxorubicin, which is intrinsically fluorescent, thereby allowing for the uptake model to be precisely fit with experimental data. However, we posit that this approach need not be limited to fluorescent drugs. With appropriate experimental design, the approach used to estimate k_{FB} can be leveraged to specifically quantify any of the rates proposed in the model. Indeed, the optimized values of doxorubicin efflux in the MDA-MB-468$_{MDR1}$ line in Figure 3.8 are similar to those values measured by the uptake assay in Figure 3.4. Importantly, this work demonstrates that all treatment conditions collapse onto a single, smooth trajectory through parameter space as a function of equivalent dose, and this property can be leveraged to provide quantitative insight into the biological drivers of treatment response. While cell lines could not be compared without precise estimates of all model parameters, this approach can nevertheless be used to more precisely quantify therapeutic perturbations within a given cell line. It is straightforward to extend the equivalent dose as a means to more precisely quantify the effects of other parameters in the experimental microenvironment (e.g., how does pH or a specific nutrient concentration affect treatment response?). In this way, these variables can be mapped onto a unified treatment response framework to more efficiently advance discovery of treatment response biomarkers.

While the results of this study are promising, several limitations exist in the current approach. This method remains to be validated in additional cell lines with other pharmacologic targets to address its generalizability, and the utility of the equivalent dose remains to be tested *in vivo*. Further, properties of *in vitro* assays not explicitly considered in the current model have been shown to confound observed effects. For example, local cell densities have been found to affect observed treatment response (190). Finally, this model is deterministic and does not consider either population heterogeneity or cell evolution. Despite these limiting assumptions we note the utility of the equivalent dose in summarizing a range of doxorubicin treatment conditions.

3.7 Conclusion

We have demonstrated that a mechanistic model of treatment response can completely describe doxorubicin therapy over a wide range of treatment conditions. We further provide demonstration of the utility of the mechanistic modeling approach, which consolidates contributions of pharmacokinetics and pharmacodynamics into a holistic measure of treatment response. This approach provides more biological insight relative to previous assays of treatment

response. Further, we have demonstrated how mathematical modeling can be leveraged to infer biological properties that are difficult to explicitly measure (e.g., k_{FB} in the context of DNA-PK inhibition). It is the ultimate goal of precision cancer therapy to deliver the optimal therapy on the optimal schedule for the individual patient. A necessary step toward this goal is to establish a robust functional relationship between applied treatment and subsequent response. The present study demonstrates the utility of the modeling framework and provides additional evidence that the response to therapy is *predictable*. Further, it provides a generalization of our previously-published model (177) to incorporate the effect of sensitizing agents. We hypothesize that this framework may even be applicable to targeted agents, which target proteins expressed at various levels among cell lines. Looking forward, these approaches will allow for treatment responses to be precisely titrated to match patient-specific and tumor-specific pharmacologic properties.

CHAPTER 4

VARIABLE CELL LINE PHARMACOKINETICS CONTRIBUTE TO NON-LINEAR RESPONSE TO DOXORUBICIN THERAPY IN HETEROGENEOUS CELL POPULATIONS

4.1 Introduction and Contribution of Study

In this chapter, we extend the experimental-mathematical modeling approach proposed in Chapter 2 to study treatment response in heterogeneous cell populations. Tumors are composed of distinct cell clones that demonstrate a range of sensitivities to treatment. While this phenomenon has been observed across several tumor types, the quantitative study of treatment response in heterogeneous systems has been limited by the difficulty in assessing the phenotypic effects of cellular heterogeneity. Indeed, much of the literature on intratumoral heterogeneity relies on genetic expression data rather than the corresponding phenotypes to quantify heterogeneity. This fundamentally limits investigation into the non-linear behaviors exhibited by heterogeneous populations that arise due to interactions among clones.

We study heterogeneity in the context of multi-drug resistant breast cancer. We culture the green fluorescent protein-tagged, multi-drug resistant protein 1 (MDR1) overexpressing cell line developed in Chapter 3 with its parental cell line, which expresses a red fluorescent protein-tagged histone H2B. In this way, each cell line can be independently tracked *via* fluorescence, allowing for the proposed mathematical model to be fit to each cell line within the heterogeneous population. We found that the combination of the MDR1-overexpressing cell line with its parental line is non-linear in that model parameter values change as a function of the co-culture conditions. We propose and experimentally test a pharmacokinetic-based hypothesis to explain the observed nonlinearity. The data presented in this chapter indicate that intercellular pharmacokinetic variability should be considered in analyzing treatment response in heterogeneous cell populations.

4.2 Abstract

Tumors are composed of heterogeneous populations of cells that demonstrate a range of sensitivities to treatment. In this chapter, we develop a combined experimental-mathematical framework to quantify how heterogeneity impacts treatment response. Specifically, we investigate heterogeneity in the context of multi-drug resistant breast cancer treated with doxorubicin, a

standard-of-care cytotoxic therapy. We engineered a cell line to over-express the multi-drug resistance 1 protein (MDR1), an ATP-dependent pump that effluxes drug from the cytoplasm and into the extracellular space. A series of longitudinal fluorescence microscopy experiments in which the MDR1-overexpressing cell line is co-cultured with its parental cell line is utilized to assess the impact of cell population heterogeneity on response to doxorubicin therapy. These data are subsequently analyzed using a coupled pharmacokinetics/pharmacodynamics model to quantify the effect of heterogeneity. We observed that the death rate in the parental line under low-dose doxorubicin conditions is increased more than two-fold, from 0.64 ($\pm$0.22) $\times$ 10^{-2} hr^{-1} to 1.46 ($\pm$0.58) $\times$ 10^{-2} hr^{-1}, in the presence of the MDR1-overexpressing line. Further, we observe a 29% increase in growth rate in the MDR1-overexpressing line as the fraction of MDR1-overexpressing cells at the time of seeding is decreased. We demonstrate, both mathematically and experimentally, that the differential pharmacokinetics of these lines contribute to the observed increase in death rate in the parental population. Specifically, in pharmacokinetic simulations, we observe an increase in accumulation of doxorubicin in the parental cell line that potentially contributes to the increasing death rate in co-culture experiments. Finally, under treatment with an MDR1 inhibitor, the death rate of the parental cell line appears independent of the presence of the MDR1-overexpressing line. These data indicate that intercellular pharmacokinetic variability should be considered in analyzing treatment response in heterogeneous cell populations.

4.3 Introduction

The advent of precision medicine has brought significant advances to oncology. The majority of these efforts have focused on the use of genetics to classify and pharmaceutically target cancers (2). This approach has led to a paradigm in which tumor genotypes are matched to appropriate treatments (3,4). While the current genetic-centric approach to cancer therapy has great merit in appropriately selecting therapies and identifying new pharmaceutical targets, it can frequently overlook a host of patient- and tumor-specific measures that influence response to therapy. For example, the microenvironment of the tumor alters response (6), delivery of therapy to tumors is variable as tumor perfusion is limited (7,8), and patient-specific pharmacokinetic properties vary (9,10). In addition to these factors, tumors often demonstrate significant intratumoral heterogeneity that evolves over time (191). Specifically, tumors are composed of cells

that demonstrate significant differences in phenotypes, such as gene expression and sensitivity to anti-cancer agents (117,150). It is an ongoing challenge in clinical oncology to quantify tumor heterogeneity to adjust therapy choice, dose, and frequency to account for evolving tumor behavior in the individual patient.

Intratumoral heterogeneity affects the response of tumors to therapy (118,192). Accordingly, this heterogeneity presents a significant challenge to precision medicine initiatives that seek to match treatment protocols to biopsy data (119). Tumor initiation and progression has long been described as an evolutionary process in which the tumor is composed of discrete clones that are selected according to their relative fitness (193). Specifically, the fitness of a single clone is defined by its interactions with neighboring clones and the microenvironment (194). These inter-clonal interactions include those defined in ecology such as competition, under which clones compete for a limited resource, and mutualism, in which clonal interactions provide a benefit to each clone (118). Some of these interactions result in selective sweeps, in which a single clone expands to dominate a neoplasm. Alternatively, non-autonomous behavior, in which driver mutations in one clone confer benefit to neighboring clones, selects for heterogeneous populations to maximize tumor population fitness, often to the detriment of the patient. For example, in a small cell lung cancer model, clonal heterogeneity was found to enhance tumor proliferation and metastatic potential (195).

The dynamics of cancer progression have been a target of mathematicians for decades (18,196). Several models have been proposed to describe the evolution of a tumor in response to therapy over time (197,198). However, given the technical challenges of deciphering cellular heterogeneity, there are few experimental systems in which treatment response in heterogeneous cell populations can be rigorously and mathematically studied. Of note, Frick and colleagues proposed the clonal fractional proliferation assay to investigate how heterogeneity within a cell line impacts population-level measures of treatment response (150). Additionally, clone tracking approaches, such as cellular barcoding (199), have been developed to monitor cell lineages in heterogeneous populations both *in vitro* and *in vivo*. Clone tracking techniques have been leveraged to understand how both genetic and non-genetic heterogeneity influence tumor behavior (200,201) and study intratumoral evolution (202). While these approaches provide insight into how heterogeneity affects treatment response, these insights have yet to be codified into a mechanistic mathematical model.

A goal of mathematical modeling is to abstract the key features of a physical system to succinctly describe its behavior in a series of mathematical equations. In this way, the system can be simulated *in silico* to further understand system behavior, generate specific, experimentally-testable hypotheses, and guide experimental design. With respect to treatment response in heterogeneous populations, a coupled experimental-mathematical modeling approach is needed to parameterize proposed models and provide mechanistic insight into how heterogeneous populations respond to treatment (22). In this work, we develop such an approach to measure and predict treatment response in heterogeneous cell populations. Specifically, we systematically investigate this problem in triple negative breast cancer cell lines subject to standard-of-care doxorubicin therapy. We develop two cell lines: a doxorubicin-sensitive line and a doxorubicin resistant, multi-drug resistance protein 1 (MDR1)-overexpressing line. MDR1 is a surface membrane pump that actively effluxes drug from cells, decreasing drug accumulation within cells and conferring resistance to anthracyclines (including doxorubicin), taxanes, and several other agents (120). Notably, up to 40% of breast cancers demonstrate expression of MDR1 (203). Each cell line is engineered to be distinguished *via* fluorescence imaging, which is utilized to monitor cell population dynamics. We build on a coupled pharmacokinetic/pharmacodynamic model of doxorubicin treatment response (177) to quantify how sensitive and resistant cell lines respond to treatment independently and in combination. Finally, we leverage mathematical models to predict aspects of treatment response in heterogeneous cell populations.

4.4. Materials and Methods

4.4.1 Cell Lines

The MDA-MB-468 triple negative breast cancer cell line was obtained through American Type Culture Collection (ATCC, http://www.atcc.org) and maintained in culture according to ATCC recommendations. The line was virally transduced to express a monomeric red fluorescence protein (mRFP)-tagged H2B protein as described previously(141,150). The H2BmRFP-expressing MDA-MB-468 cell line was again transduced to express green fluorescent protein (GFP)-tagged MDR1 (ABCB1 gene, Origene Technologies, Rockville, MD). Following transduction, the cell line was cultured in 100 nM doxorubicin for two weeks to select a doxorubicin-resistant phenotype. The H2BmRFP MDA-MB-468 and the double positive H2BmRFP, MDR1GFP MDA-MB-468 cell lines are denoted as parental and resistant, respectively. Notably, the

transduced fluorophores are both stably expressed, allowing for these cell lines to be distinguished *via* fluorescence imaging (RFP only for the parental line; RFP and GFP for the resistant line) without the addition of dyes. Sample images of each cell line are shown in Figure 4.1.

4.4.2 Chemicals

Doxorubicin is a standard-of-care cytotoxic agent used in the treatment of several malignancies, including triple negative breast cancer. Doxorubicin canonically induces DNA damage by intercalating DNA bases, stabilizing the topoisomerase II complex, and inducing DNA damage *via* free radical formation (147). Doxorubicin hydrochloride was obtained from Sigma Aldrich and diluted to a stock concentration of 1 mM in saline.

Tariquidar (TQR) is a third-generation MDR1 inhibitor that non-competitively inhibits MDR1 function (182). TQR is leveraged to modulate doxorubicin pharmacokinetics in the resistant cell line. TQR was purchased from Selleckchem (Boston, MA) and dissolved to a 1 mM stock concentration in DMSO. Both doxorubicin and TQR were stored in 250 µL aliquots at -80 °C.

4.4.3 Treatment Response Assays

The response of each cell line to doxorubicin was measured using previously-published dose response assays (177). Briefly, cells were added to 96-well microtiter plates at 5,000 cells per well. Cells were treated with doxorubicin concentrations ranging from 2,500 to 10 nM and subsequently removed *via* media replacement after 24 hours. These experimental conditions were designed such that the areas under the concentration of doxorubicin curves overlapped those observed *in vivo* (143). These cells were imaged daily *via* fluorescent microscopy for up to two weeks following treatment with doxorubicin. For these treatment response studies, fluorescence microscopy images were collected using a Synentec Cellavista High End platform (SynenTec Bio Services, Münster, Germany) with a 20× objective and tiling of 25 images. Two co-registered channels of data were collected for these experiments: a red channel (Excitation: 529 nm, Emission: 585 nm) with 650 ms exposure to image H2BRFP and a green channel (Excitation: 470 nm, Emission: 530 nm) with 20 ms exposure to image the MDR1GFP. At least three replicates of each treatment condition were collected. Media was refreshed every 3 days for the duration of each experiment to ensure sufficient growth conditions for surviving cells.

The response of both the parental and resistant lines were assessed using the above assay. To investigate the behavior of heterogeneous populations, the parental and resistant cell lines were introduced to the microtiter plate at several ratios totaling 5,000 cells per well. For example, to simulate a tumor composed of 20% resistant cells, 1,000 resistant cells were added to 4,000 cells from the parental line. The response of these co-culture conditions was measured in the same way as above. Several co-culture conditions were investigated, ranging from 20% to 80% (in increments of 20-25%) resistant cells.

4.4.4 Image Processing

Nuclei were segmented and counted in MATLAB (Natick, MA) using a previously-described, threshold-based method to quantify cell populations (150). A classification scheme was developed to identify resistant cells (GFP-expressing) in heterogeneous populations. Each identified nucleus and its surrounding area was described by an image feature vector (described below), and a support vector machine (SVM) was used to classify each nucleus as belonging to either the parental or resistant cell line. Support vector machines seek to define a hyperplane to optimally separate two classes (204). The SVM was trained using image feature vectors from a subset of cells identified in parental-only and resistant-only experiments. In all, the training set consisted of 10,000 feature vectors corresponding to 5,000 parental and 5,000 resistant cells.

Each cell identified *via* segmentation was described by a feature vector focusing on the intensity of the green channel image. For each identified nucleus, the average GFP intensity around the nucleus was calculated within a bounding box. Three bounding box sizes were used: 20×20, 30×30, and 40×40 pixels. Additionally, a radial intensity histogram was computed around each identified nucleus. The histogram summarizes the distribution of image intensities as a function of radial distance from the center of the nucleus. Specifically, the histogram consisted of twenty bins, each containing of the average intensity over 5 pixel-wide rings with increasing radii centered on the nucleus. Finally, the distance from the nucleus to peak GFP intensity was calculated. We hypothesized that these features would capture the brightness patterns of the resistant cells, which express the MDR1GFP on the cell membrane (see Figure 4.1 for examples).

A 10-fold cross validation approach was used to train and tune the SVM. To classify images in the test set (i.e., cells in the co-cultured wells), the above features were calculated for each

Figure 4.1: Sample image time series of parental and resistant cell lines and illustration of the counting and classification scheme. Both the parental and resistant cell lines are engineered to express a nuclear H2BmRFP label (left column). The resistant line additionally expresses a GFP-tagged MDR1 protein (middle column). Note that these fluorophores are stably expressed as the images show the same area over six days. The nuclear image (left column) is used for cell segmentation and counting. A SVM classifier is used to classify each detected cell as parental or resistant in co-culture conditions using the GFP image (middle column). A sample segmentation and classification result is shown in the right column. In this example, the resistant cells are colored blue and the parental line is shown in red. The classifier is able to accurately identify each cell line.
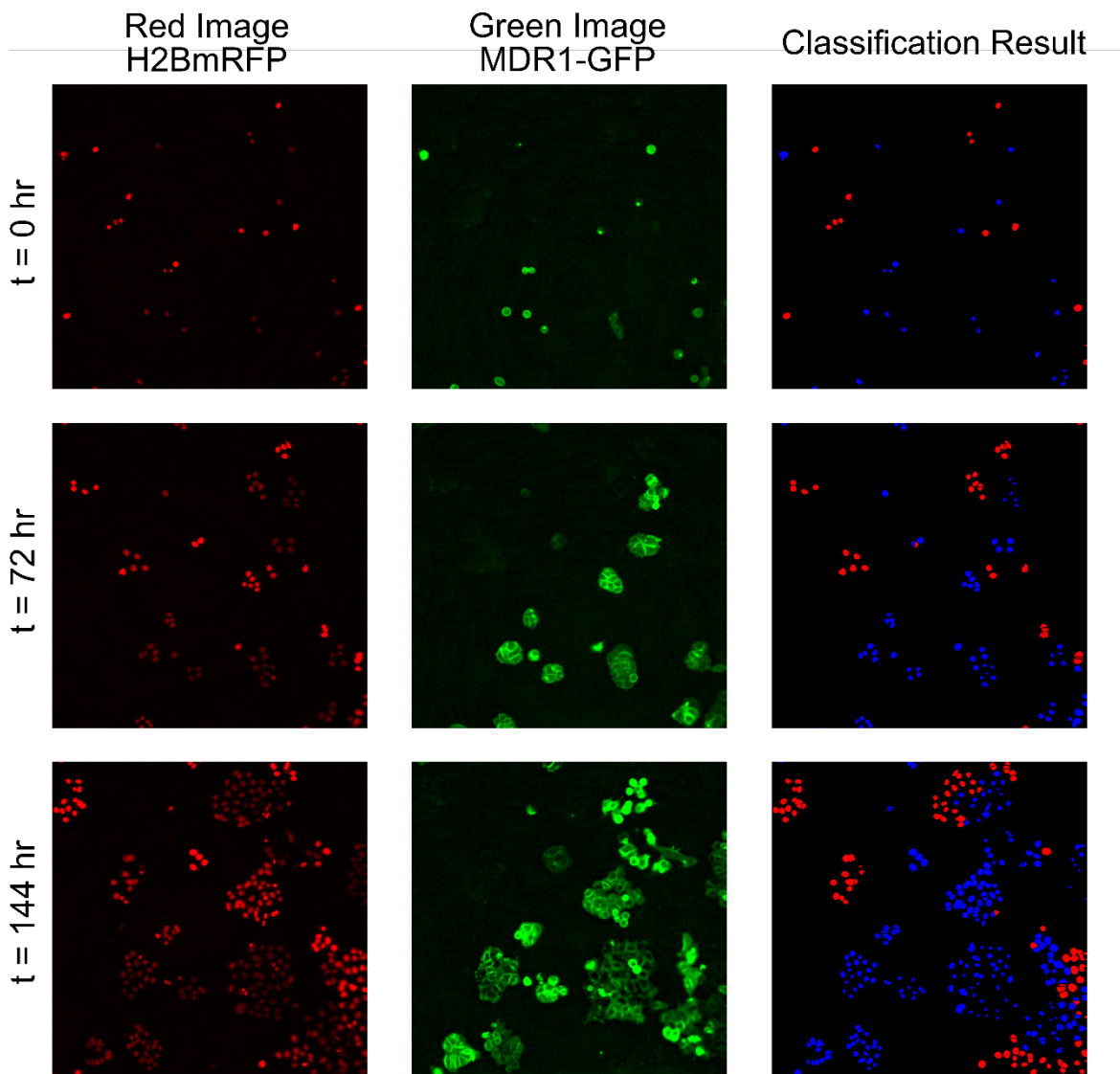
identified cell and passed to the trained SVM. In this way, the image processing pipeline outputs the cell counts of both the parental and resistant lines.

4.4.5 Treatment Response Model

　　We previously proposed and validated a coupled pharmacokinetic/pharmacodynamic model of doxorubicin treatment response *in vitro* (177). The model incorporates measured doxorubicin pharmacokinetic and pharmacodynamic rates and allows for *prediction* of treatment response to a wide range of treatment conditions on a cell-line specific basis. We now extend this model to account for the two cell populations present in the current experimental system. A compartment model is used to describe doxorubicin pharmacokinetics:

$$\frac{dC_E(t)}{dt} = k_{FE,P}\frac{v_{I,P}}{v_E}C_{F,P}(t) - k_{EF,P}C_E(t) + k_{FE,R}\frac{v_{I,R}}{v_E}C_{F,R}(t) - k_{EF,R}C_E(t) \tag{4.1}$$

$$\frac{dC_{F,P}(t)}{dt} = k_{EF,P}\frac{v_E}{v_{I,P}}C_E(t) - k_{FE,P}C_{F,P}(t) - k_{FB,P}C_{F,P}(t) \tag{4.2}$$

$$\frac{dC_{B,P}(t)}{dt} = k_{FB,P}C_{F,P}(t) \tag{4.3}$$

$$\frac{dC_{F,R}(t)}{dt} = k_{EF,R}\frac{v_E}{v_{I,R}}C_E(t) - k_{FE,R}C_{F,R}(t) - k_{FB,R}C_{F,R}(t) \tag{4.4}$$

$$\frac{dC_{B,R}(t)}{dt} = k_{FB,R}C_{F,R}(t) \; , \tag{4.5}$$

where $C_E(t)$, $C_{F,c}(t)$, and $C_{B,c}(t)$ are the concentrations of doxorubicin in the extracellular, free, and bound compartments, respectively, in cell line c (parental, P, or resistant, R) at time t. Both the free and bound compartments are defined to share the same physical space (intracellular). The free compartment represents drug that has diffused into the cell, while the bound compartment represents drug that has bound to DNA. The $k_{ij,c}$ parameters are rate constants that describe the movement of doxorubicin between each of these compartments in each cell line; for example, $k_{FE,R}$ describes the rate of drug transfer from the free, intracellular compartment of the resistant cell line to the extracellular compartment. Similar definitions apply to $k_{EF,R}$, $k_{FB,R}$, $k_{EF,P}$, $k_{FE,P}$, and $k_{FB,P}$.

The volumes of the intracellular and extracellular compartments are denoted with $v_{I,c}$ and $v_{E,c}$, respectively.

The pharmacodynamics model is similarly extended from that presented in previous work (177) to include both parental and resistant cells. Specifically, we define the temporal change of a population consisting of a specified fraction of resistant cells, f, to a delivered doxorubicin dose, D, for all time, t as follows:

$$N_T(t) = N_P(t) + N_R(t) \tag{4.6}$$

$$\frac{dN_P(t)}{dt} = \left(k_{p,P}(f) - k_{d,P}(t,D,f)\right) N_P(t) \left(1 - \frac{N_P(t) + N_R(t)}{\theta(D,f)}\right) \tag{4.7}$$

$$\frac{dN_R(t)}{dt} = \left(k_{p,R}(f) - k_{d,R}(t,D,f)\right) N_R(t) \left(1 - \frac{N_S(t) + N_R(t)}{\theta(D,f)}\right), \tag{4.8}$$

where N_T is the total population size, N_P is the number of parental cells, and N_R is the number of resistant cells. $k_{p,c}$ and $k_{d,c}$ are the proliferation and dose-specific death rates for cell line c, respectively. θ is the dose-specific carrying capacity describing the maximum number of cells that can be supported by the experimental system. Dose, D, is defined as the maximum bound concentration of drug following treatment and is calculated by simulating the pharmacokinetics model using an experimentally-defined extracellular doxorubicin concentration timecourse. Of note, all rates are allowed to vary as a function of co-culture condition, defined by f. The death rate, $k_{d,c}$, for each population can assume either of the following forms:

$$k_{d,c}(t,D,f) = \begin{cases} 0 & t < 0 \\ k_{d,a}(D,f) & t \geq 0 \end{cases} \tag{4.9}$$

$$k_{d,c}(t,D,f) = \begin{cases} 0 & t < 0 \\ k_{d,b}(D,f)r(D,f)te^{1-r(D,f)t} & t \geq 0 \end{cases} . \tag{4.10}$$

Eq. (4.9) assumes an immediate transition to a constant post-treatment death rate, $k_{d,a}$. Eq. (4.10) assumes a smooth induction to and recovery from a maximal death rate, $k_{d,b}$. r describes the rate at which treatment response is induced. A weighted averaging approach is used to combine these two models (i.e., Eqs. (4.6) – (4.8) with the death rate in Eq. (4.9) and Eqs. (4.6) – (4.8) with the

death rate in Eq. (4.10) into a single best-fit model. Additional information on the model can be found in previous work (177).

4.4.6 Treatment Response Model Fitting

The two-species pharmacodynamics model, Eqs. (4.6) – (4.8), is fit to data by minimizing the following objective function, $G(x)$:

$$\min_{x} G(x) = \sum_{t=t_i}^{t_f} \left(\frac{Y_{t,P} - \hat{Y}_{t,P}(x)}{Y_{t,P}} + \frac{Y_{t,R} - \hat{Y}_{t,R}(x)}{Y_{t,R}} + \frac{Y_{t,T} - \hat{Y}_{t,T}(x)}{Y_{t,T}} \right)^2 ,$$

where x is the set of parameters to be estimated, $Y_{t,c}$ is the measured cell counts at time t for cell line c, $\hat{Y}_{t,c}$ is the model-estimated cell counts at time t for cell line c when the model is evaluated with parameters x, and t_i and t_f are the initial and final timepoints respectively. c represents the parental cell line (P), resistant cell line (R), or total cell count (T). Specifically, the proliferation rate ($k_{p,R}$, $k_{p,P}$) and all dose-response parameters ($k_{d,R}$, $k_{d,P}$) for each cell line are optimized to fit the data. Data from each co-culture and treatment condition are fit independently using a nonlinear least squares optimization routine implemented in MATLAB (Natick, MA). Model fits are compared to the measured response for each cell line, and the mean percent error across all timepoints is reported for the best fit model.

In the optimization approach, the model is initialized with the cell counts at the timepoint following treatment for each individual replicate, and all subsequent timepoints are considered in the model fit. To avoid local minima, the fitting process is initialized with 200 sets of parameter estimates selected randomly from expected distributions for each parameter. k_d values are initialized by sampling a uniform distribution $[-1k_p, 5k_p]$. r is bounded within $[0.001, 0.05]$ hr^{-1}. Further, θ is bounded between $[0.7\theta, 1.2\theta]$, where θ is the carrying capacity observed in the control data for each cell line.

To ensure the stability and accuracy of the optimization routine for each of these studies, simulations were conducted with perfectly known population compositions and treatment response parameters. Gaussian noise with zero mean and a standard deviation of 5% of each cell lines' count were added to the simulated data to reflect the accuracy of the classification scheme. The model optimization routine was run on these simulated timecourses. The model parameter fits derived

from these simulated datasets are compared to their specified values, and R^2 statistics comparing simulated to fit parameters are reported.

Table 4.1: Properties for pharmacokinetic simulation

Parameter	Value	Source
v_E	250 μL	Experimentally-defined extracellular volume
v_I	0.005 μL	10,000 cells × 5e-7 μL (estimated volume per cell)
k_{EF}	[0.005, 0.05] hr^{-1}	Jackson (2003) (159)
$k_{FE,P}$	0.05 hr^{-1}	Experimentally derived (Figure 3.13)
$k_{FE,R}$	[0.05, 0.15] hr^{-1}	Experimentally derived (Figure 3.13)
$k_{FB,R}$,$k_{FB,P}$	0.015 hr^{-1}	Experimentally derived (Figure 3.13)

4.4.7 Simulation of Pharmacokinetics in Heterogeneous Cell Populations

We hypothesize that there will be a statistically significant increase in response of the parental cell line to doxorubicin in the presence of resistant cells and that this increase is due to an increased accumulation of drug in the parental cells secondary to efflux of drug from resistant cells. To explore this hypothesis, we simulate the pharmacokinetics model to assess the accumulation of drug in the parental cells ($C_{B,P}$) over a range of co-culture conditions. For these simulations, the parental and resistant cell lines are assumed to have identical pharmacokinetic parameters, except for the doxorubicin efflux parameter ($k_{FE,R}$ and $k_{FE,P}$) (measurements of k_{EF} and k_{FB} in these cell lines are indeed similar (see Figure 3.13)). To assess the effect of the efflux rate on the accumulation of drug in the parental cell line, a range of $k_{FE,R}$ values were simulated while holding $k_{FE,P}$ constant. To simulate a range of co-culture conditions, the total intracellular volume ($v_{I,R} + v_{I,P}$) was held constant while altering the relative volumes of the intracellular compartment of the resistant and parental cell lines. Notably, proportional changes in $k_{EF,P}$ and $k_{EF,R}$ were made to reflect the changing volumes of the intracellular compartments. Doxorubicin primarily diffuses into cells (205), and diffusion, described with the k_{EF} term, is proportional to membrane permeability and surface area. As we assume the cell surface area per unit volume for each cell line is constant in all co-culture conditions, the changing intracellular volumes require corresponding changes in cell surface areas. Specifically, for a simulation consisting of a fraction f of resistant cells and influx rate k_{EF}, $k_{EF,P} = (1-f)k_{EF}$ and $k_{EF,R} = f k_{EF}$. This adjustment ensures that for each cell line the accumulation of drug per unit cell volume is constant in all co-

culture conditions. A complete list of parameter values is shown in Table 4.1. While several of the parameters are derived from the measurements reported in Chapter 3, we rely on literature estimates for k_{EF} (159) as the image-based method used in Chapter 3 underestimates the magnitude of doxorubicin accumulation within cells relative to previous studies (144,205).

4.4.8 Modulation of Pharmacokinetics in Heterogeneous Cell Populations

To test experimentally the hypothesis that the resistant cells cause an increase of doxorubicin accumulation in the parental cells and, therefore, increased death rate, the efflux of drug *via* MDR1 in the resistant cell line is inhibited with TQR. By inhibiting the effect of this pump, we hypothesize that the death rate of the parental population to doxorubicin should be independent of the presence of resistant cells. The treatment response assay described in Section 4.4.3 is repeated with 1 µM of TQR applied one hour prior to doxorubicin therapy and throughout the course of the assay. Notably, low concentrations of doxorubicin (50 and 100 nM) are used to avoid saturating the death rate. These data are fit with the pharmacodynamics model, and the hypothesis is assessed by measuring the change in the death rate of the parental population ($k_{d,P}$) as a function of the percentage of resistant cells at the time of seeding.

4.5. Results

4.5.1 Cell Counting Results

A representative image set and corresponding segmentation and classification results are shown in Figure 4.1. The tuned SVM correctly classified 98.5% of cells in the training set. In a separate image set consisting of experimental replicates with exclusively parental or resistant cells with over 16,000 parental and 12,000 resistant cells, the classifier achieved a sensitivity of 0.942 with a specificity 0.994.

4.5.2 Simulation Results

The treatment response model (i.e., Eqs. (4.6) – (4.8)) was simulated at 11 mixture ratios, ranging from 0% to 100% resistant cells in 10% increments. For these simulations, the proliferation rates of the parental and resistant lines were fixed at 0.02 hr⁻¹ and 0.015 hr⁻¹, respectively. Simulations were run with eight treatment conditions assuming either the death rate

Figure 4.2: Optimization routine accurately identifies simulated death rates. Eqs. (4.6) − (4.8) were simulated over a range of co-culture conditions using the death model assumed in Eq. (4.9). The death rate of each cell line was estimated using the optimization routine in Section 4.4.6. Model estimates and 95% confidence intervals are shown for the parental (left) and resistant (right) cell lines. The legends in each figure panel denote the percentage of resistant cells present at the beginning of the simulation. The death rate for each cell line can be accurately recovered.
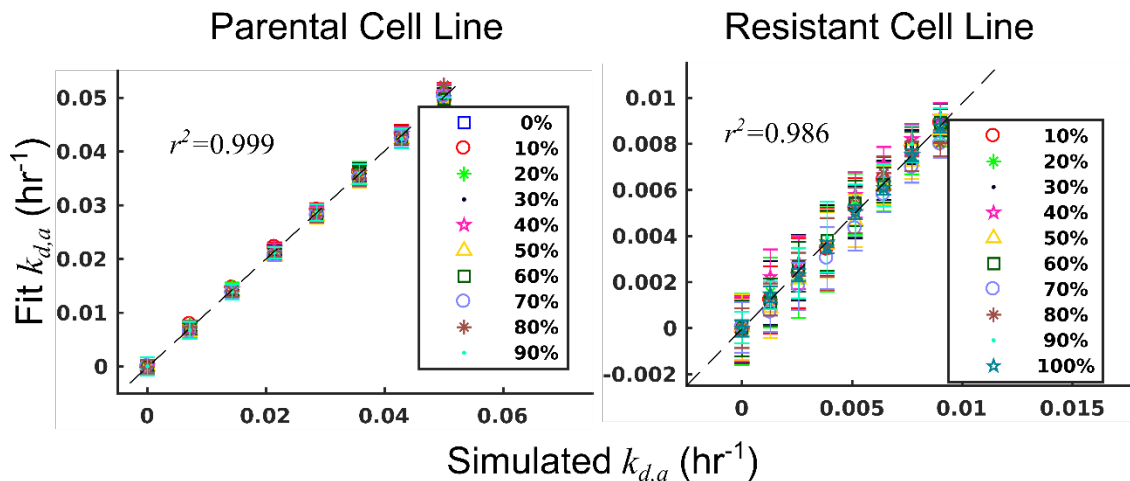
Figure 4.3: Optimization routine accurately identifies simulated proliferation rates. Eqs. (4.6) − (4.8) were simulated over a range of co-culture conditions. The proliferation rate of each cell line was estimated using the optimization routine in Section 4.4.6. Model estimates and 95% confidence intervals are shown for the parental (red) and resistant (blue) cell lines. For these simulations, the proliferation rate of the parental and resistant lines were fixed at 0.02 hr^{-1} and 0.015 hr^{-1}, respectively. The proliferation rate for each cell line can be accurately recovered.
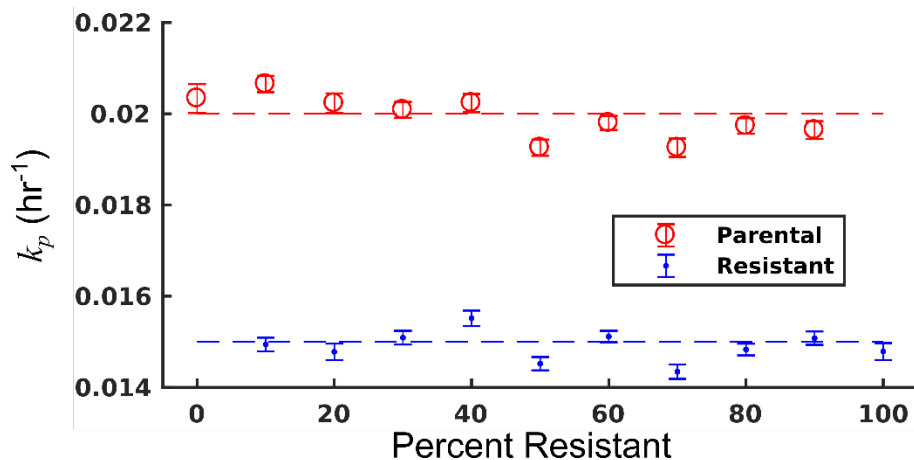
Figure 4.4: Optimization routine accurately identifies simulated death rates. Eqs. (4.6) − (4.8) were simulated over a range of co-culture conditions using the death model assumed in Eq. (4.10). The death rate of each cell line was estimated using the optimization routine in Section 4.4.6. Model estimates and 95% confidence intervals are shown for the parental (left) and resistant (right) cell lines. For these simulations, r was fixed to 0.02 hr^{-1} for both cell lines to avoid the variability observed in $k_{d,b}$ at low values of r previously reported (177). The legends in each figure panel denote the percentage of resistant cells present at the beginning of the simulation. The death rate for each cell line can be accurately recovered.
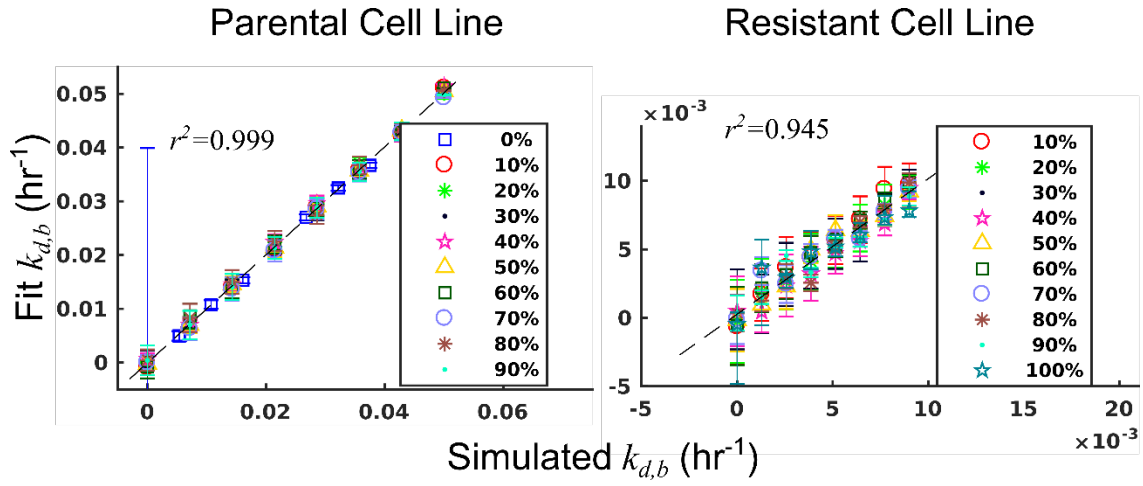
in Eq. (4.9) or Eq. (4.10). Additionally, r (Eq. (4.10)) was fixed to 0.02 hr^{-1} for both cell lines to avoid the variability observed in $k_{d,b}$ at low values of r previously reported (177). The optimization routine outlined in Section 4.4.6 was used to estimate model parameters from the simulated data. The recovered parameter values with corresponding 95% confidence intervals are compared to their simulated values in Figures 4.2 – 4.4. The optimization framework successfully returned model parameters with $R^2 > 0.94$ for all model parameters.

4.5.3 Model Fits

The treatment response model (i.e., Eqs. (4.6) - (4.8)) was fit to each co-culture and treatment condition. Model fits are superimposed on the total population cell counts in Figure 4.5. The model was able to accurately capture the total cell count over a wide range of co-culture and treatment conditions with a mean percent error of 10.1% across all data points. Additionally, the model was able to describe the behavior of each cell line in co-cultured conditions. The cell counts for the resistant and parental cell lines under a range of co-culture conditions at a representative doxorubicin treatment are shown in Figure 4.6. The best fit model is overlaid on these data. The mean percent errors over all timepoints of the model fits to the parental and resistant lines are 17.2% and 8.9%, respectively. Of note, the high error rates of the parental line are concentrated in conditions of high cell death with relatively low cell counts.

Prior to treatment with doxorubicin, the parental and resistant cell lines displayed exponential growth in monoculture with proliferation rates (k_P) of 2.07 ($\pm$0.08) $\times$ 10^{-2} hr^{-1} and 1.72 ($\pm$0.04) $\times$ 10^{-2} hr^{-1}, respectively (the bounds here and below correspond to the 95% confidence interval of the parameter estimates). The proliferation rate of the resistant cell line increases as the percent of resistant cells at the time of seeding decreases. Conversely, the proliferation rate of the parental cell line decreases as the percent of resistant cells increases. The proliferation rate of each species as a function of the percentage of resistant cells is shown in Figure 4.7. For example, in an untreated control in the 75% resistant culture, the parental proliferation rate decreases 30% from its monoculture rate to 1.45 ($\pm$0.07) $\times$10^{-2} hr^{-1}. In the untreated 25% resistant culture control, the proliferation rate of the resistant line increases 29% from its monoculture rate to 2.22 ($\pm$0.07) $\times$ 10^{-2} hr^{-1}. The mean percent error of the model fits in these control conditions were 9.1% and 14.9% for the resistant and parental lines, respectively.

Figure 4.5: Treatment response in heterogeneous cell populations and pharmacodynamic model fits. The total cell counts (sum of resistant and parental cells) over time and corresponding 95% confidence intervals are shown for in a representative set of doxorubicin treatments and co-culture conditions. These data are fit by Eqs. (4.6) – (4.8), and the model fit is overlaid on the data (smooth lines in all panels). The parental line is more sensitive to doxorubicin therapy relative to the resistant line. Complete population regression of the parental line is seen for doxorubicin treatments ≥ 500 nM (a). The resistant cell line continues to proliferate under 500 nM doxorubicin (f). The proposed model can describe the observed pharmacodynamics.
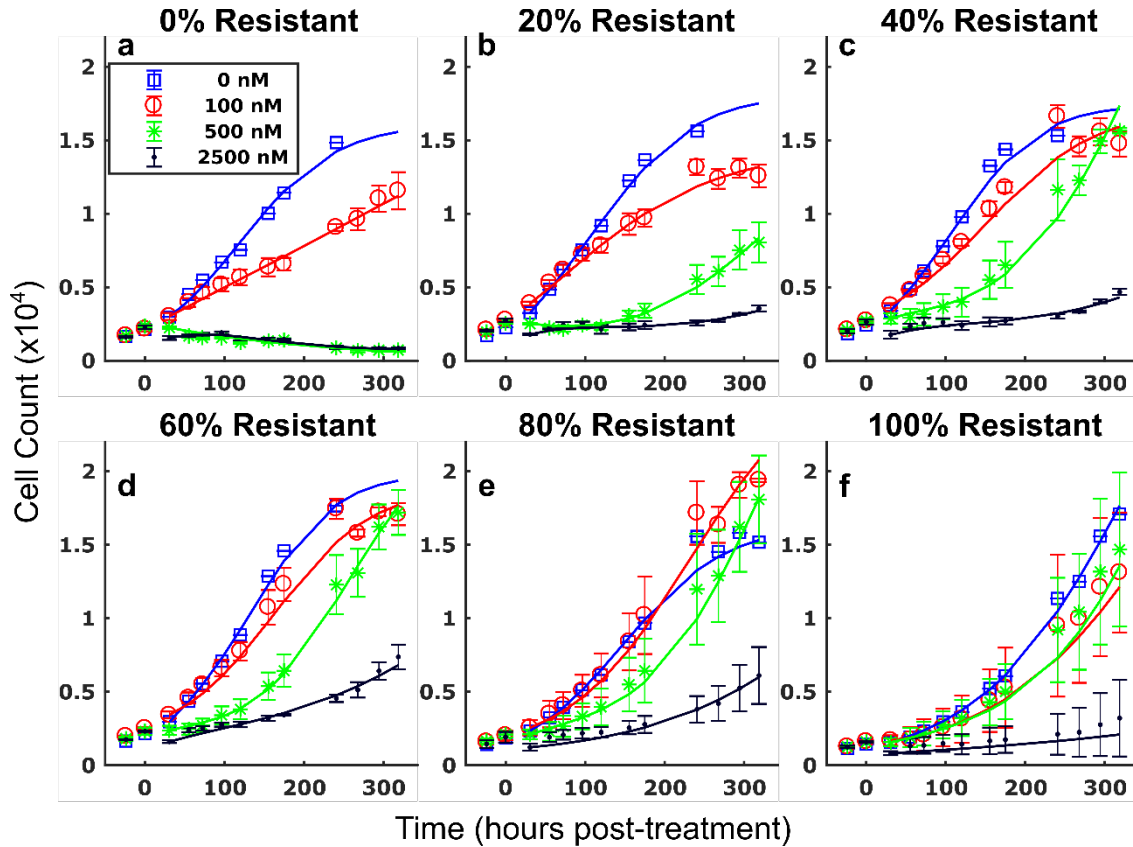
Figure 4.6: Model fits for each cell line in several co-culture conditions following treatment with 100 nM of doxorubicin. In the current system, each cell line can be quantified throughout the course of the experiment. The cell counts of the parental (red) and resistant (blue) lines with 95% confidence intervals are shown following treatment with 100 nM doxorubicin. The total cell counts with 95% confidence intervals are shown in black. Eqs. (4.6) – (4.8) are fit to these data, and the best-fit model is overlaid on the observed cell counts (smooth line in all panels). While the parental line demonstrates continued positive proliferation in monoculture (a), the net proliferation rate of the parental line decreases with increasing fractions of resistant cells (b-e).
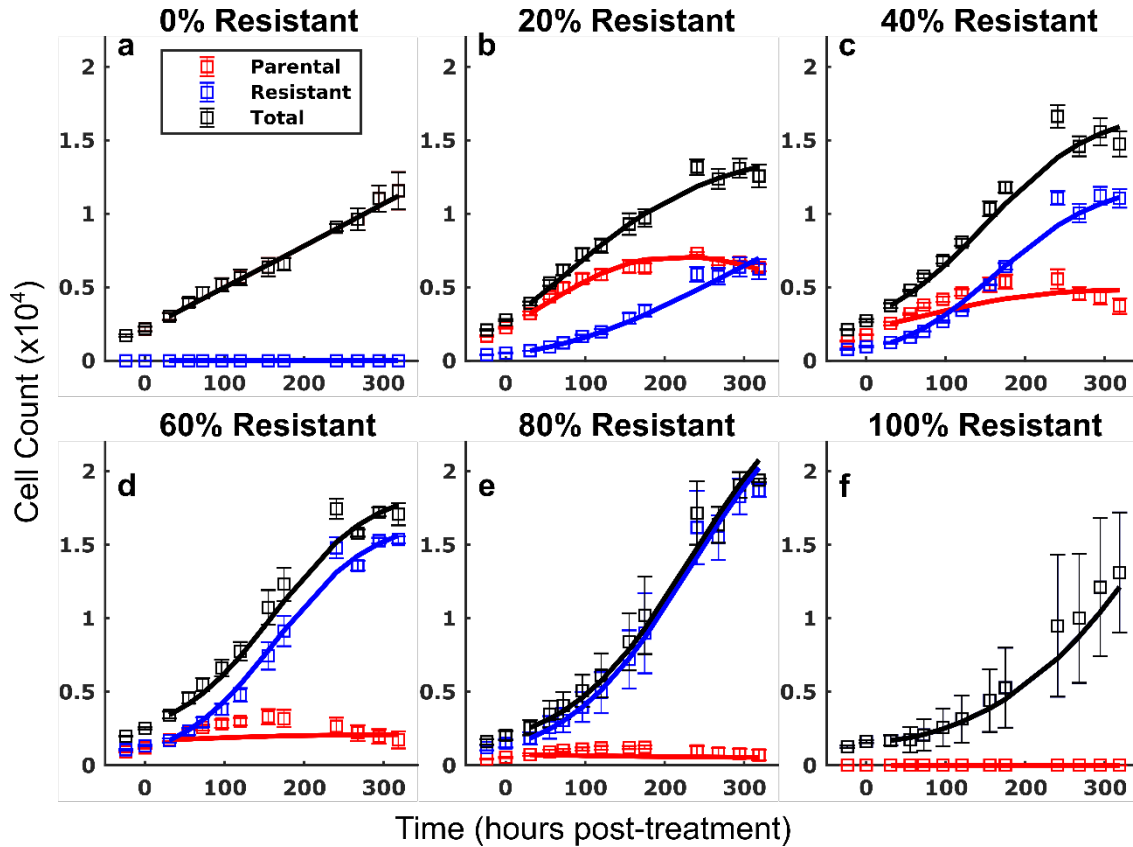
Figure 4.7: Proliferation rate of each cell line changes as a function of co-culture condition. The proliferation rate of each cell line and corresponding 95% confidence interval are estimated from control experiments (no doxorubicin). These rates are shown as a function of the percentage of resistant cells at the time of seeding. The proliferation rate of the resistant cell line increases as the fraction of resistant cells decreases. Conversely, the proliferation rate of the parental cell line decreases as the fraction of resistant cells increases.
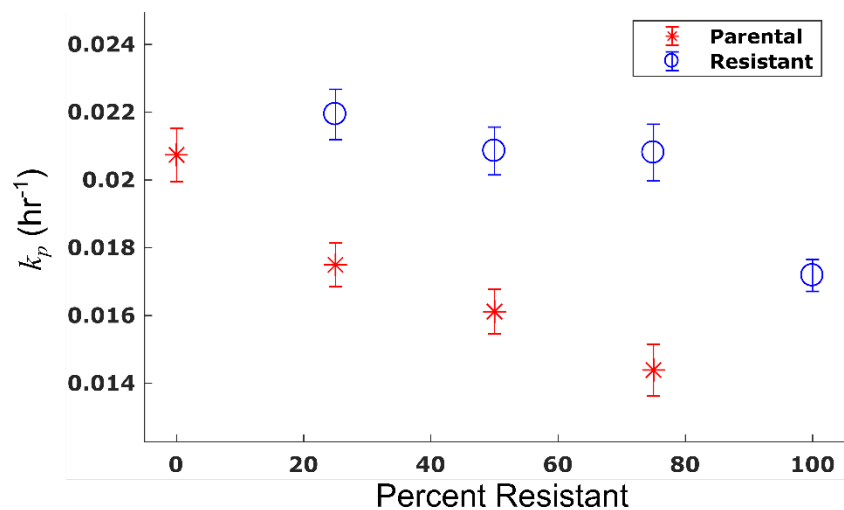
Figure 4.8: Net proliferation rate of the parental (left) and resistant (right) cell lines as a function of the number of resistant cells present at the time of seeding. Eqs. (4.6) – (4.8) were fit to each cell line in each co-culture and treatment condition. The net proliferation rate (k_p - $k_{d,a}$) with corresponding 95% confidence intervals under 100 and 500 nM of doxorubicin is shown for each cell line as a function of the percentage of resistant cells. Sensitivity to doxorubicin in the parental cell line increases with increasing fractions of resistant cells as demonstrated by the significant decrease in net proliferation rate under 100 nM of treatment with increasing fractions of resistant cells(left). The net proliferation rate of the parental line appears saturated at approximately -0.5 × 10^{-2} hr^{-1} under treatment with 500 nM doxorubicin. Conversely, the net proliferation rate of the resistant line increases with decreasing numbers of resistant cells (right). This indicates that the increase in proliferation rate in the resistant line more than offsets the effects of low-dose doxorubicin.
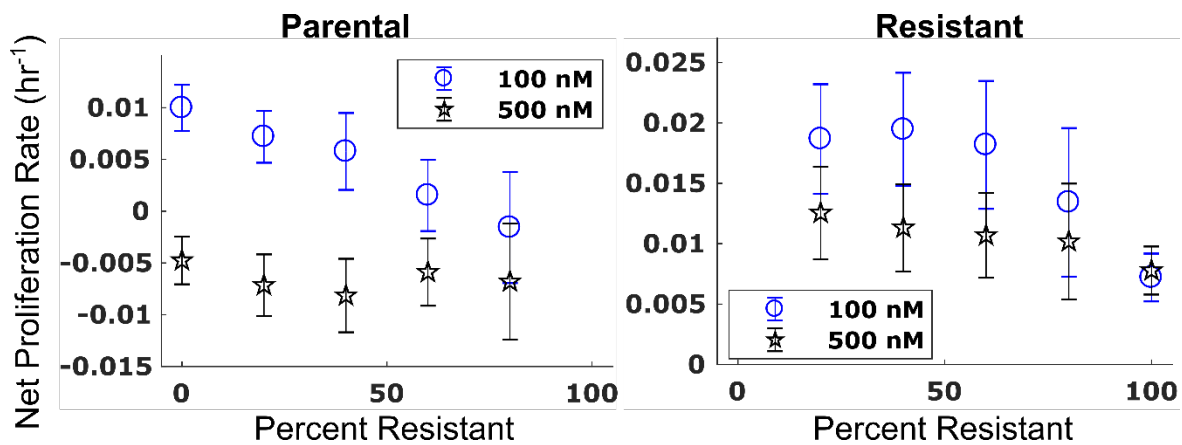
Table 4.2: Model parameter fits for parental cell line (error represents 95% confidence interval)

Parental:Resistant	Concentration (nM)	$k_{d,a}$ ($\times 10^{-2}$ hr^{-1})				$k_{d,b}$ ($\times 10^{-2}$ hr^{-1})				r ($\times 10^{-2}$ hr^{-1})			
		0	100	500	2500	0	100	500	2500	0	100	500	2500
	100:0	-0.03 (±0.55)	0.64 (±0.22)	2.11 (±0.23)	1.88 (±0.31)	-0.28 (±5.35)	0.98 (±0.65)	2.57 (±0.49)	2.15 (±0.11)	5.00 (±64.2)	0.58 (±0.36)	0.86 (±0.12)	0.58 (±0.07)
	80:20	-0.36 (±0.44)	0.63 (±0.25)	2.07 (±0.30)	1.66 (±0.31)	-0.98 (±1.51)	2.07 (±1.65)	2.44 (±0.27)	1.92 (±0.25)	4.53 (±6.38)	0.15 (±0.24)	0.87 (±0.03)	0.54 (±0.05)
	60:40	-0.37 (±0.72)	0.69 (±0.37)	2.08 (±0.35)	1.62 (±0.38)	-0.99 (±3.41)	2.91 (±0.44)	2.42 (±0.28)	1.98 (±0.31)	4.45 (±13.6)	0.10 (±1.28)	0.62 (±0.02)	0.46 (±0.06)
	40:60	-0.32 (±0.86)	1.13 (±0.34)	1.87 (±0.32)	1.64 (±0.37)	-1.12 (±3.53)	3.62 (±0.16)	2.31 (±0.31)	1.89 (±0.32)	5.00 (±14.5)	0.10 (±0.82)	0.72 (±0.03)	0.51 (±0.05)
	20:80	-0.10 (±1.30)	1.35 (±0.54)	1.87 (±0.56)	1.39 (±0.47)	-1.02 (±3.62)	4.20 (±0.20)	2.26 (±0.48)	1.63 (±0.50)	5.00 (±18.5)	0.10 (±1.01)	0.48 (±0.04)	0.54 (±0.07)

Table 4.3: Model parameter fits for resistant cell line (error represents 95% confidence interval)

Parental:Resistant	Concentration (nM)	$k_{d,a}$ ($\times 10^{-2}$ hr^{-1})				$k_{d,b}$ ($\times 10^{-2}$ hr^{-1})				r ($\times 10^{-2}$ hr^{-1})			
		0	100	500	2500	0	100	500	2500	0	100	500	2500
	80:20	-0.51 (±0.87)	-0.17 (±0.45)	0.44 (±0.38)	0.75 (±0.57)	-1.39 (±2.03)	1.82 (±4.34)	0.51 (±0.41)	1.10 (±1.41)	0.19 (±5.40)	0.10 (±1.44)	0.62 (±1.13)	0.33 (±0.35)
	60:40	-0.52 (±0.91)	-0.22 (±0.47)	0.59 (±0.36)	0.89 (±0.57)	-1.72 (±3.42)	1.82 (±3.27)	0.68 (±0.40)	1.06 (±0.61)	0.16 (±4.75)	0.10 (±1.37)	0.56 (±0.72)	0.45 (±0.43)
	40:60	-0.37 (±0.73)	-0.20 (±0.53)	0.54 (±0.35)	0.65 (±0.51)	-1.61 (±3.68)	1.60 (±2.14)	0.60 (±0.66)	1.03 (±0.85)	0.10 (±3.58)	0.10 (±1.38)	2.05 (±1.34)	0.34 (±0.59)
	20:80	-0.10 (±0.60)	0.16 (±0.61)	0.49 (±0.48)	0.77 (±0.71)	-0.94 (±2.22)	0.88 (±1.37)	0.63 (±0.72)	0.97 (±0.83)	0.10 (±6.69)	0.11 (±3.03)	1.24 (±1.21)	0.39 (±0.52)
	0:100	0.00 (±0.37)	0.31 (±0.20)	0.25 (±0.20)	0.69 (±0.40)	0.05 (±5.08)	1.50 (±2.84)	0.36 (±0.17)	0.88 (±0.31)	4.98 (±292)	5.00 (±5.59)	1.39 (±1.78)	0.39 (±0.49)

Each cell line demonstrated a concentration-dependent response to doxorubicin treatment. The parameter fits with 95% confidence intervals from a representative experimental replicate are shown in Tables 4.2 and 4.3 for the parental and resistant lines, respectively. The death rate of the parental cell line ($k_{d,P}$)appears to saturate to approximately 2.0×10^{-2} hr^{-1} at high doxorubicin doses (≥ 500 nM) (this is the death rate assumed in Eq. (4.9)). A similar trend was noted in the death rate derived from Eq. (4.10) (see Tables 4.2 and 4.3)). Notably, the death rate in the parental cells for the 100 nM treatment condition increases with the number of resistant cells present in the population. In the parental-only condition, the death rate is 0.64 (± 0.22) $\times 10^{-2}$ hr^{-1}. This rate increases to 1.46 (± 0.58) $\times 10^{-2}$ hr^{-1} when the population consists of 80% resistant cells. Increasing death rate in the parental population with increasing numbers of resistant cells was noted in all experimental replicates (Figure 4.10a). The resistant cell line demonstrates decreased sensitivity to doxorubicin therapy relative to the parental line. For example, the death rate in the resistant line under 100 nM treatment (0.31 (± 0.20) $\times 10^{-2}$ hr^{-1}) is half that observed in the parental line.

In Figure 4.8, the net proliferation rate (k_p - k_d) for each species is shown as a function of the percentage of resistant cells at the time of seeding. Notably, the increase in the death rate in the parental cell line is compounded by the decreasing proliferation rate, creating a synergistic effect leading to a significantly decreased net proliferation rate with increasing fractions of resistant cells. Further, the increased proliferation rate in the resistant line is greater than the effect of doxorubicin, causing an increasing net proliferation rate with decreasing fractions of resistant cells.

4.5.4 PK Simulation

Based on the results of section 4.5.3, it is clear that the presence of resistant cells increases the sensitivity of parental cells to treatment. Simulation of the pharmacokinetic model (i.e., Eqs. (4.1) – (4.5)) predicts an increase in drug accumulation (up to 15%) in the parental cell line ($C_{B,P}$) in the presence of resistant cells. Simulation results are shown in Figure 4.9. As the accumulation of doxorubicin is proportional to therapy response (177), these simulations are consistent with the decreased net proliferation rate of the parental line with increasing fractions of resistant cells seen in Figure 4.8 and Table 4.2. A synergistic effect of the efflux rate of the resistant cells ($k_{FE,R}$) and the fraction of resistant cells present in the co-culture condition in increasing the accumulation of drug in the parental line is observed. The magnitude of this effect is proportional to k_{EF}.

Figure 4.9: Pharmacokinetics model predicts increased doxorubicin accumulation in the parental cell line with increasing efflux rate in the resistant line ($k_{FE,R}$) and increasing fractions of resistant cells. The pharmacokinetics model was simulated to assess the effect of $k_{FE,R}$ and the fraction of resistant cells on the accumulation of drug in the parental cells ($C_{B,P}$). In these simulations, the drug binding rate was equal for each cell line ($k_{FB,R} = k_{FB,P}$), and the diffusion rate into each cell line was equal ($k_{EF,R} = k_{EF,P} = k_{EF}$). The fraction of resistant cells in the population was varied between 0 (entirely parental) and 0.95. The efflux rate for the resistant cells ($k_{FE,R}$) was varied between 0.05 and 0.15 hr^{-1}. The efflux rate for the parental population ($k_{FE,P}$) was fixed at 0.05 hr^{-1}. All other parameter values are specified in Table 4.1. The drug accumulation in the parental cell line ($C_{B,P}$) is normalized to the minimum simulated value in each plot to show the percent increase in drug accumulation as the fraction of resistant cells, k_{EF}, and $k_{FE,R}$ are varied. As the percentage of resistant cells increase, there is an increase in the drug accumulation in parental cells. This accumulation is further increased as $k_{FE,R}$ increases. The magnitude of this effect is proportional to the simulated value of k_{EF}.
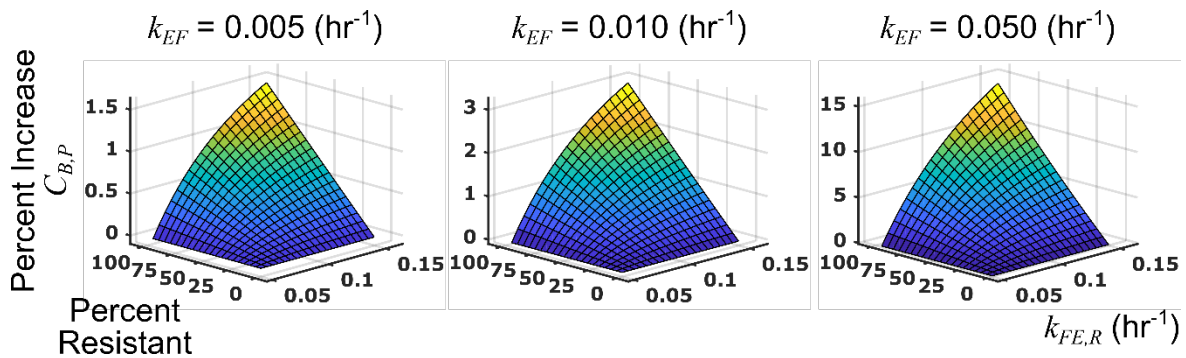
Additionally, no difference in $C_{B,P}$ is observed when $k_{FE,R} = k_{FE,P}$. This suggests that the response of the parental line to therapy would be independent of the presence of resistant cells if $k_{FE,R}$ were decreased to match $k_{FE,P}$.

4.5.5 MDR1 Inhibition

      The co-culture treatment response experiments were repeated with addition of 1 μM TQR, and the treatment response model was fit to the resulting timecourses. The mean percent errors over all timepoints and treatment conditions of the model fits to the parental and resistant lines in these experiments are 6.5% and 5.9%, respectively. The death rate of the resistant cell line increased with the addition of TQR. For example, under treatment with 100 nM doxorubicin, the death rate of the resistant line increased an order of magnitude from 0.093 ($\pm$0.084) $\times$ 10^{-2} hr^{-1} to 2.00 ($\pm$0.87) $\times$ 10^{-2} hr^{-1} with addition of TQR. Contrary to the previous observation that the death rate of the parental line increases with increasing numbers of resistant cells, the death rate of the parental line appears constant across co-culture conditions with addition of TQR. These results are illustrated in Figure 4.10. This observation is consistent with the prediction of the PK model. By equalizing the efflux rate of the two cell lines through use of TQR, the death rate of the parental cell population appears independent of the presence of resistant cells. Of note, while treatment with TQR appeared to restore the linearity of the death rate with respect to co-culture condition in the parental population, the proliferation rate of each cell line still varied with respect to co-culture condition. This is illustrated in Figure 4.11. Again, the model described these control data well with mean percent errors of 9.7% and 7.0% for the parental and resistant lines, respectively.

4.6 Discussion

      We have established an experimental-mathematical modeling framework to investigate the response of heterogeneous cell populations to doxorubicin therapy. While the treatment response of a cell line in monoculture can be described by a parsimonious mathematical model, the treatment response of heterogeneous cell populations is non-linear in that model parameters change as a function of population composition. Specifically, over a range of clinically-relevant doses, the death rate of parental cells is increased in the presence of resistant cells. Further, the proliferation rate of the resistant cell line increases with decreasing fractions of resistant cells, and the proliferation rate of the parental cells is depressed with increasing fractions of resistant cells. We

Figure 4.10: The death rate in the parental population is constant as a function of co-culture condition when the MDR1 pump is inhibited. The death rate in the parental cell line appears to increase with increasing percentages of resistant cells (a). The resistant cell line is relatively insensitive to doxorubicin treatment as demonstrated by the small death rates in b. The assay is repeated with the addition of 1 µM TQR, which inhibits MDR1 function. The addition of TQR reverses the trend observed in a, and the response to therapy in the parental line appears constant as a function of co-culture condition (c). The death rate of the resistant cell line increases significantly with addition of TQR (d).
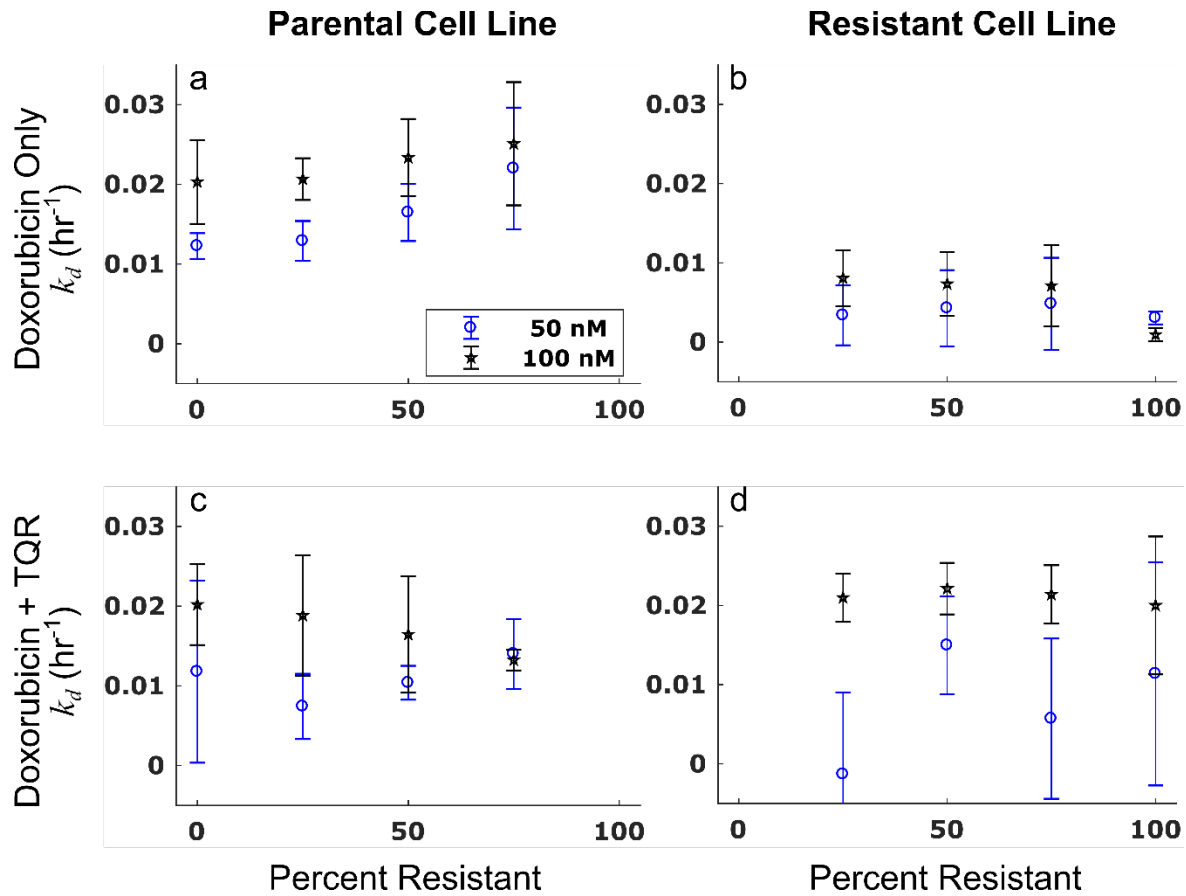
Figure 4.11: Proliferation rates of parental and resistant cell lines under treatment with TQR. Proliferation rates were estimated from control (i.e., no doxorubicin) treatment response studies with 1 µM TQR. The proliferation rate of the parental line decreases with increasing fractions of resistant cells. Conversely, the proliferation rate of the resistant cells increases slightly as the fraction of resistant cells decreases. This is consistent with the observation in Figure 4.7.
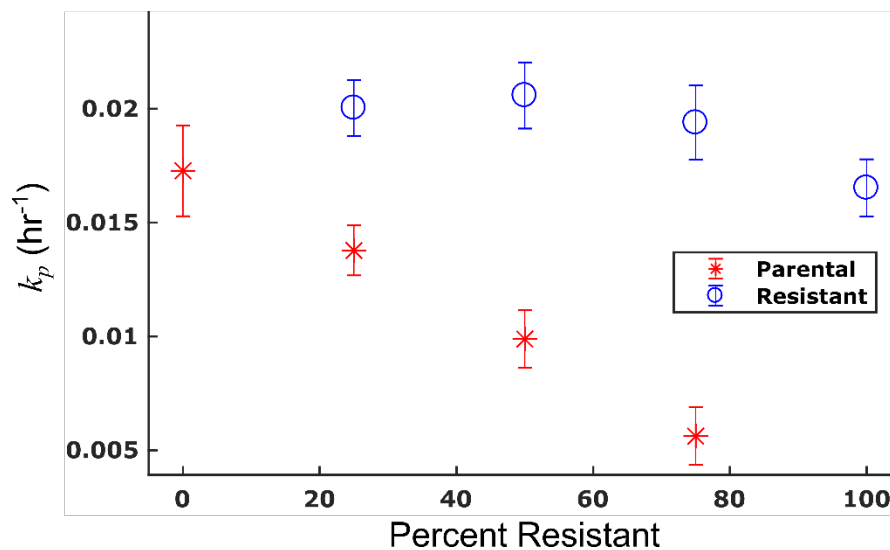
have proposed and validated a pharmacokinetics-based mechanism contributing to the nonlinearities in the observed death rates. We believe this framework to be a useful tool to systematically investigate the behavior of heterogeneous systems and to characterize *quantitatively* how heterogeneity affects therapy response.

Both the growth and death rates of each cell line are altered in co-culture conditions. The MDR1-overexpressing cell line demonstrates increased resistance to doxorubicin treatment relative to the parental cell line, and this difference is accentuated in co-culture conditions. When grown together, the resistant line grows more quickly, and the parental cell line is further sensitized to doxorubicin therapy. Taken together, we posit these observations largely agree with the ligand-capture hypothesis of cell competition (206,207). Briefly, the ligand-capture hypothesis assumes: 1) the ligand is in limiting supply; 2) the ligand is a survival signal; and 3) partial withdrawal of the ligand triggers apoptosis.

The differing proliferation rates could be explained through competition for growth nutrients. Specifically, the MDR1 pump is ATP-dependent (208), and in other MDR1-positive cell lines, glucose uptake and ATP consumption are significantly increased relative to MDR1-negative cell lines (209,210). Potentially, with transduction of MDR1, the resistant cells in this work evolve an improved ability to capture nutrients from the environment to support the metabolic demands of the pump. The enhanced growth rate of resistant cells seen at low fractions of resistant cells may arise due to a decrease in competition for nutrients with fewer resistant cells. Conversely, the decreasing proliferation rate of the parental cells in the presence of resistant cells may arise due to the increased nutrient consumption by the resistant cells. Indeed, ATP generation mechanisms have been shown as a basis for cellular competition (211). The proposed model can be extended to describe these effects through inclusion of metabolic rates into the proliferation rate. Just as the death rate was defined to account for varying drug concentrations (Eqs. (4.9) – (4.10)), the proliferation rate can be defined to include the availability of nutrients, similar to the model proposed by Silva and colleagues (210).

The enhanced death rate of the parental line requires a slight modification of the ligand-capture hypothesis, which we denote as the ligand-rejection hypothesis. Specifically, we assume again that the ligand (in this case drug) is in limiting supply. However, the ligand is a cell death signal, and addition of ligand induces death. Cells that are able to reject or metabolize ligand will out-compete those that avidly consume the ligand. This is indeed the behavior predicted by

simulations of the extended pharmacokinetic model in Figure 4.9 and validated with the experiments presented in Figure 4.10. We hypothesize that this pharmacokinetic-based mechanism may also contribute to responses to targeted anti-cancer agents.

We proposed and validated a mechanism that contributes to the increasing death rates in the parental cell line in co-culture conditions. Notably, simulation of the pharmacokinetic model (Eqs. (4.1) – (4.5)) suggested that increasing the efflux rate of the resistant cell line increased drug accumulation within the parental cells. This increased accumulation would, in turn, lead to increased death rates of the parental line in co-culture conditions. These simulations generated a specific hypothesis (i.e., inhibition of the MDR1 pump could restore the linearity of the death rate) that could be tested experimentally. Indeed, when MDR1 function is inhibited with TQR, the death rate of the parental cell line appears constant across co-culture conditions (Figure 4.10c). These data indicate that variable cellular pharmacokinetics contribute to the nonlinear death rate of parental cells. We note that these data do not exclude alternative hypotheses explaining the observed phenotype. Specifically, additional intercellular interactions (e.g., cell-cell signaling, extrusion of toxic metabolites from the resistant line *via* MDR1, or impaired DNA repair mechanisms in the parental line secondary to nutrient depletion) may contribute to the observed increase in death rate. Indeed, these additional interactions may be necessary as the increase in drug accumulation predicted by the PK model is relatively small compared to the fractional increase in death rate over co-culture conditions.

In this work, we proposed a biophysical mathematical model that describes the temporal dynamics of clones interacting within a heterogeneous population. Such interactions are inherent in heterogeneous tumors and form the basis of tumor evolution (212,213). Mathematical modeling and evolutionary game theory approaches have been used to study the co-culture-dependent behavior observed in the current experiments (214). For example, in a mouse xenograft model in which non-autonomous behaviors were observed, a mathematical framework was proposed to quantify dynamic interactions among individual clones (201). While such modeling approaches are a powerful tool to identify the magnitude of clonal interactions, the models are not designed to provide mechanistic insight into the interactions they describe. Indeed, it is not readily apparent how such methods can leverage the genetic data generally used to assess tumor heterogeneity to predict phenotypic clonal interactions. This work provides a framework that can be used to derive mechanistic, biophysical models describing clonal interactions. Specifically, we posit the proposed

high-throughput experimental-modeling platform can be leveraged to elucidate the biophysical basis of the interactions that underlie the emerging phenotypes observed in heterogeneous populations. In this way, these models can be used to generate precise hypotheses as to optimal means to improve treatment response in cancer (215).

The current approach has several limitations. While the variability in cell line pharmacokinetics is significant in predicting treatment response in the engineered cell populations in this work, these observations remain to be tested in additional cell lines and *in vivo*. Further, the proposed pharmacokinetic interaction does not preclude the presence of additional inter-clonal interactions that alter treatment response. For example, cells can secrete factors to stimulate growth and transfer resistance to previously-sensitive cells (216,217). The spatial dependency of the clonal interactions observed in this study remains to be investigated. Indeed, local cell densities have been found to affect treatment response *in vitro* (190). Finally, the hypothesized metabolism-based competition driving differing proliferation rates in co-culture conditions requires further exploration. However, with these limitations come opportunities to iteratively increase the complexity of the experimental-modeling framework to quantify the magnitude of each of the above effects. Indeed, a major goal of mathematical modeling in cancer is to build models that distill the relevant biology into a parsimonious set of equations. The framework proposed in this work provides a rich platform from which these equations can be constructed.

4.7 Conclusion

In the *in vivo* setting, the genetic composition of a tumor is unknown *a priori*. While biopsy and imaging data provide insight into the dominant genetic and phenotypic behavior of the tumor, these response measurements are often limited to coarse measurements of the bulk tumor. These measures, in isolation, are unable to resolve and quantitatively characterize small subpopulations of tumor cells. Additionally, these data are unable to predict treatment response, limiting clinicians to use standardized dosing regimens, despite the known inter- and intra-patient heterogeneity in several solid tumor types. While it is our ultimate goal to resolve the phenotypes of several parameters using bulk data measurements, we must identify first principles that govern the behavior of tumor cells in response to therapy. In this work, we provide quantitative evidence that intratumoral heterogeneity significantly impacts treatment response. Additionally, we posit that these changes arising from heterogeneity are *predictable* through use of mathematical models of

pharmacokinetics and pharmacodynamics. Through discovery of these first principles that govern treatment response, we move closer to 1) estimating tumor heterogeneity from population-level data and 2) realizing the ultimate goal of precision medicine: delivery of the optimal therapy at the optimal dose on the optimal schedule.

CHAPTER 5

SYNOPSIS AND FUTURE DIRECTIONS

5.1 Dissertation Summary

Mathematical models of tumor growth and treatment response can be leveraged to guide and optimize patient therapies. A growing and maturing literature exists on the development of such models (18,22,218). Formulation of these models must strike a balance between complexity and applicability. As we reviewed in Chapter 1, simple models of tumor growth, such as logistic or Gompertz models, are easily parameterized with experimental data and can describe tumor volume changes observed experimentally and clinically (39,219,220). Indeed, Norton and Simon's dose-dense hypothesis was constructed using a Gompertz model of tumor growth (40). However, these models often fail to capture the spatial, temporal, and biological heterogeneity observed in tumor development. Models structured to account for such heterogeneity are more complex, characterized by numerous parameters that are difficult to measure with the requisite spatial or temporal resolution (221–223). Often, authors must draw parameter values from the literature or simply estimate them (19). While these models have potential to investigate fundamental laws of tumor growth and inform experiments to probe tumor behavior, we currently lack the framework to use these models "off the shelf" to make predictions for a specific experimental system. This limits their potential translation to a clinical population.

It is our ultimate goal to realize the utility of mathematical models in guiding clinical decision making. With this ultimate objective, this Dissertation is submitted having established a robust mathematical model of doxorubicin treatment response in an *in vitro* model of triple negative breast cancer. We posit the experimental-modeling framework presented in this Dissertation is an exemplar for the quantitative study of treatment response. A mechanistic mathematical model of treatment response was proposed and iteratively refined to account for increasing levels of complexity observed in data. The ability for the model to describe cellular response to therapy in a wide range of doxorubicin (Chapter 2), co-treatment (Chapter 3), and co-culture conditions (Chapter 4) demonstrates the promise of mathematical modeling in quantifying treatment response. By studying these various perturbations within a single mathematical

framework, this approach provides a means for more efficient discovery of predictive biomarkers and translation of those discoveries into patient care.

5.2 Significance

Fundamentally, treatment response is driven by patient-, tumor-, and cell-specific pharmacologic and biological processes. At the cellular level, these processes include drug metabolism and binding. At the cell population level, response is complicated by interactions among heterogeneous cell clones. In tumors and 3D culture, microenvironmental properties, including mechanical stiffness and composition, further shape the response to treatment. At the *in vivo* scale, treatment response is further impacted by the communication among various organ systems (circulatory, immune, etc.). Often, these many sources of variability are not explicitly considered in the development and evaluation of therapeutics (224). We hypothesize that this unsophisticated approach is partly responsible for the high failure rates of clinical trials of proposed anti-cancer therapies (14).

This Dissertation provides a foundation from which the complexity detailed above can be approached. Specifically, we have developed and validated a biophysical model of the cellular response to doxorubicin in Chapter 2. This model withstood perturbation by agents that alter cellular pharmacology in Chapter 3, providing further validation of the mathematical model. Finally, the model was leveraged to study the effect of clonal interactions in a simple experimental model of heterogeneity in Chapter 4. Throughout this Dissertation, complexity was introduced modularly, and the model was iteratively refined to account for that complexity. We posit that this approach provides a more organized and precise approach to anti-cancer drug development. Previous *in vitro* methods used to evaluate drug efficacy provide limited quantitative data on the effect of various genetic and environmental markers on drug efficacy. Specifically, they do not provide the quantitative data needed to generate precise hypotheses in differing contexts. Conversely, the framework proposed in this dissertation has been shown to translate easily across various treatment and cell culture conditions.

From a biological and clinical perspective, the TNBC designation is a label of exclusion. Breast cancer is canonically classified by the expression of estrogen, progesterone, and HER2 receptors. TNBC lacks upregulation of these markers, limiting therapeutic options. This label has limited progress towards improved therapies as clinical trials are clouded by the genetic and

phenotypic heterogeneity among triple negative tumors (139). The modeling framework we proposed provides a new lens through which TNBC treatment can be approached. We have demonstrated that a heterogeneous panel of TNBC cell lines respond similarly to doxorubicin therapy. While the absolute responses vary, the underlying physiology remains the same (i.e., the same mathematical model can describe treatment response in all of these lines). This work provides additional insight into the cellular phenotypes driving treatment response, thereby providing specific targets for future research.

5.3 Innovation

We developed a coupled experimental-modeling framework to understand the effects of a common chemotherapeutic, doxorubicin, under a range of experimental conditions. We highlight three particularly innovative components of this Dissertation:

Temporal response to therapy. Traditionally, cytotoxic therapies are evaluated in a dose-response framework *via* colorimetric assays, such as MTT and ATP assays (111). These approaches assess cell viability after exposure to a 10^5-fold range of drug concentrations for 72 hours. The effects of these drugs are often summarized by potency metrics, such as EC_{50}, the extracellular drug concentration eliciting a half-maximal effect. However, slight changes in experimental duration or growth conditions have been shown to significantly impact estimation of model parameters (130,131). Consequently, the predictive potential of such approaches is fundamentally limited, particularly in the setting of cytotoxic agent use *in vivo*, in which agents are applied as impulses and resilient populations, which demonstrate temporally-varying population growth rates following therapy, are often observed. The proposed model explicitly characterizes temporal aspects of treatment and subsequent response. We posit that this will allow for the *in vitro* observations to more easily scale to treatment response assessment *in vivo*.

Incorporation of combination therapies into a unified mathematical framework. The concept of precisely targeting molecular deficits in tumors has long driven the development of anti-cancer therapies (225). Given a tumor's complexity and ability to evolve, it is likely that rational combinations of these therapeutics will be needed to maintain durable responses (226). Rational combination therapies seek to optimally combine drugs to maximize response while minimizing toxicities. The promise of combination therapies relies on the precise dosing of these agents (189). The equivalent dose metric proposed in Chapter 3 provides an example of how

mathematical models can be leveraged to provide precise guidance on the dosing of combination therapies. While the proposed equivalent dose metric leverages a relatively simple model for its calculation, the concept of targeting a response and modulating underlying biological factors to achieve that response is readily extendable to other therapy combinations.

Incorporation of heterogeneity into a unified mathematical framework. Intratumoral heterogeneity affects the response of tumors to therapy and presents a significant challenge to precision medicine initiatives (118,119,192). While mathematical modeling approaches are a powerful tool to study the effects of heterogeneity (18,196–198,214), these models often provide little mechanistic insight into tumor behavior. In Chapter 4, we proposed a framework that can be used to derive mechanistic, biophysical models describing clonal interactions. We posit the proposed high-throughput experimental-modeling platform can be leveraged to elucidate the biophysical basis of the interactions that underlie the emerging phenotypes observed in heterogeneous populations. In this way, these models can be used to generate precise hypotheses as to optimal means to improve treatment response in heterogeneous tumors.

5.4 Limitations

While the proposed model accurately describes treatment response observed *in vitro*, the model remains to be validated *in vivo*. Cells grown on plastic in 2D culture behave much differently than cells grown in 3D culture (227). The *in vivo* environment presents additional challenges relative to 3D culture. Specifically, the solid tumor microenvironment is constrained by perfusion, impairing nutrient and drug delivery (6).

The coupled pharmacokinetic/pharmacodynamics model proposed in this work is robust to a host of doxorubicin, sensitizer, and co-culture conditions. However, in the current form, the approach is limited to drugs with intrinsic fluorescent properties. While we proposed a means to extend this to non-fluorescent agents in Chapter 3, the proposed approach remains to be validated with additional therapeutic agents.

The heterogeneity investigated in Chapter 4 was experimentally induced. While similar inter-clonal interactions undoubtedly occur, the magnitude and character of these effects remain to be investigated in other heterogeneous cell populations.

5.5 Future Directions and Recommendations

The coupled experimental-mathematical modeling system developed in this Dissertation offers a robust platform from which treatment response can be quantitatively investigated. To future investigators, I offer below four proposals that naturally and immediately follow the developments in this Dissertation.

5.5.1 Translation in vivo

It is the ultimate goal to scale the proposed model *in vivo* to create a framework in which therapies can be assessed *in vitro* and rapidly translated *in vivo*. While the proposed model can handle the temporally-varying plasma drug concentrations seen *in vivo* following injection of doxorubicin, the model must be extended to incorporate the effects of the tumor microenvironment. Specifically, tumor vasculature is functionally immature (89), affecting the distribution of doxorubicin *in vivo* (228). Doxorubicin has been found to diffuse only ~100 μm from vessels (228), and intratumoral doxorubicin gradients have been observed in patient samples (229). In keeping with the experimental-modeling framework used throughout this Dissertation, we propose leveraging dynamic contrast enhanced magnetic resonance imaging to estimate intratumoral doxorubicin distribution in an *in vivo* model of breast cancer. Just as the model was iteratively extended to incorporate cellular heterogeneity with use of an experimental system allowing for tracking of discrete sub-populations, so too can it be extended to incorporate tumor vasculature though an experimental system assessing vascular properties. We report on the preliminary data collected towards this proposal in Appendix A.

I propose taking the same modular approach used *in vitro* to the *in vivo* study. After establishing the relationship between DCE-MRI and doxorubicin distribution, I recommend the interested investigator to modulate pharmacokinetic properties (e.g., drug clearance) and tumor vasculature (e.g., with anti-angiogenic agents) to rigorously investigate the relationship between pharmacokinetics, tumor vasculature, and treatment response.

5.5.2 Explanation of Changing Proliferation Rates in Co-Culture System

The biophysical basis of the changing proliferation rates of cell lines in co-culture conditions reported in Chapter 4 remains to be elucidated. While we hypothesize that this phenomenon is driven through metabolic pathways (230), further investigation is warranted. An alternative hypothesis is that the changing proliferation rates are secondary to factors secreted by

each cell line. I suggest the role of secreted factors be investigated first with conditioned media experiments, and I point the interested investigator to a previous model that incorporates cell-line specific metabolic properties (210).

5.5.3 Model of Multiple Treatments

Dosing schemes with cytotoxic agents all follow a common pattern: cycles of a high dose nearing the maximum tolerated dose followed by a recovery period. The goal of this strategy is to maximize tumor cell kill, while trying to minimize adverse effects *via* drug holidays between each cycle. The model proposed in this Dissertation needs to be extended to incorporate the effects of multiple treatment cycles. With a model describing multiple treatment cycles, optimization routines can be used to identify optimal treatment regimens. I suggest a simple experimental paradigm first focusing on two treatments, each with a fixed doxorubicin dose and variable time between these doses.

5.5.4 General Model for DNA-damaging Therapies

DNA-damaging agents have long formed the basis of cancer therapies. Recent efforts have focused on improving the response to these agents by targeting DNA-damage response pathways (231). These various therapies, including doxorubicin, platinum salts, and radiation, induce DNA lesions which trigger a cascade of responses resulting in lesion repair or cell death. A source of inspiration for this Dissertation was the linear quadratic model used in radiation therapy. I posit that the model proposed in this Dissertation is simply the dynamic realization of the linear quadratic model. I encourage the motivated investigator to expand the proposed equivalent dose metric to the study of all DNA-damaging agents. This would provide a more precise understanding of the biological underpinnings of the response to each of these therapies. In this way, a robust framework would be developed to tailor DNA-damaging therapy to tumor-specific biology.

5.6 Conclusion

The goal of precision medicine is to deliver the optimal therapy at the optimal dose on the optimal schedule. The current genetic-centric approach to precision cancer therapy has great merit in appropriately selecting therapies and identifying new pharmaceutical targets; however, it can

frequently overlook a host of patient-specific measures that influence response to therapy. Mathematical models of treatment response that incorporate patient-specific pharmacokinetic and pharmacodynamic measures offer the promise of tumor-specific treatment plans in which the dose and schedules of therapeutics are optimized in the same way the therapeutic is selected. The mechanistic models proposed and validated in this Dissertation provide the first step towards design of patient-specific treatment regimens. Specifically, we have shown that the treatment response of cell populations *in vitro* is predictable under various treatment and co-culture conditions. By incorporating these mechanistic models with the *in vivo* data available clinically, we envision a future for clinical oncology in which treatments can be precisely adjusted on a patient- and tumor-specific basis.

CORRELATION OF DCE-MRI PARAMETERS WITH DOXORUBICIN DISTRIBUTION IN AN *IN VIVO* MODEL OF TRIPLE NEGATIVE BREAST CANCER

A.1 Introduction and Contribution of Study

It is our ultimate goal to scale the proposed *in vitro* pharmacokinetic/pharmacodynamic model to an *in vivo* model of breast cancer. While the model proposed in Chapter 2 can handle the temporally-varying plasma drug concentrations seen *in vivo* following injection of doxorubicin, the model must be extended to incorporate the spatial constraints of the tumor microenvironment. Specifically, we note that the distribution of doxorubicin *in vivo* is perfusion-limited as doxorubicin diffuses only 100 µm from vessels. In this Appendix, we provide initial data collected to assess the utility of dynamic contrast enhanced magnetic resonance imaging in estimating intratumoral doxorubicin distribution in an *in vivo* model of breast cancer. In this way, a framework leveraging non-invasive imaging could be established to scale the model *in vivo*.

A.2 Abstract

Doxorubicin is a standard-of-care cytotoxic agent that forms the basis of neoadjuvant chemotherapy regimens for a variety of malignancies, including triple negative breast cancer (TNBC). Despite its prevalence clinically, a quantitative understanding of how doxorubicin therapy alters tumor growth is currently lacking. Accordingly, treatment schedules with doxorubicin are generalized with doses adjusted only to account for patient body surface area or excessive toxicity. While the treatment plans are homogenous, the responses to doxorubicin therapy among TNBC patients are heterogeneous. This is potentially due to a host of factors, including high variability in tumor perfusion. Tumor perfusion affects both the intratumoral distribution of drug and the response to therapy. In order to correct for heterogeneous tumor perfusion, we propose the use of dynamic contrast enhanced (DCE) magnetic resonance imaging (MRI) to estimate intratumoral doxorubicin distribution in an *in vivo* model of TNBC. In this Appendix, we propose a registration framework to register histology to *in vivo* MRI, and we present initial *in vivo* imaging data collected to assess tumor vasculature *via* DCE-MRI.

A.3 Introduction

Inducing and sustaining angiogenesis is a hallmark of cancer (87). Tumor vasculature is often morphologically and functionally immature. Relative to a healthy vasculature, tumor vasculature is tortuous and leaky with numerous blind endings and arteriovenous shunts. This impairs delivery of nutrients, causing local microenvironmental changes that alter the response to therapy (6,88,89). Further, significant heterogeneity in perfusion exists within a tumor, impacting both tumor growth and drug delivery (90). Differences in treatment response may arise due to variability in tumor perfusion.

In clinical practice, doses of chemotherapeutic agents are often personalized through use of patient body surface area (BSA) (47,48). BSA was first proposed as a guide for chemotherapy dosing by Pinkel, noting that the accepted cytotoxic dose for pediatric and adult patients, and the dose used in laboratory animals correlated with BSA across those scales (49). While a BSA-based dosing strategy is of great practical utility for calculating doses for each patient, BSA correlates poorly with the underlying physiological processes that affect drug pharmacology (e.g., liver metabolism and glomerular filtration rate) (52,53). For example, in a study of 110 patients receiving doxorubicin therapy, doxorubicin clearance was found to weakly correlate with BSA (9). Despite the weak relationship between BSA and pharmacokinetics for several therapeutics, BSA remains widely used clinically to guide dosing.

Evaluation of treatment response in solid tumors focuses exclusively on gross tumor volume changes as defined by the Response Evaluation Criteria in Solid Tumors (RECIST) (97). These criteria categorize response based on changes in the longest dimension of tumors over the course of therapy. These measurements do not consider the delivered dose of therapy despite the known heterogeneity in perfusion. Analysis of tumor images in this way provides little guidance on how to adjust treatments; indeed, it was never designed for such an application.

The current framework of drug dosing and treatment response evaluation does not consider interpatient variability in pharmacokinetics or tumor perfusion, fundamentally limiting the realization of precision medicine (i.e., delivery of the optimal dose of the optimal therapy for each patient). This approach is imprecise relative to the dose-planning approaches used in radiotherapy. Specifically, radiation oncologists leverage X-ray computed tomography images to estimate radiation dose distribution (70). An analogous measure of chemotherapy dose is currently lacking. As chemotherapy is delivered *via* tumor vasculature, we propose to develop a spatially-resolved

measure of chemotherapy dose by coupling pharmacokinetic estimates of plasma drug concentrations to non-invasive, functional vascular imaging data. Whereas several methods have been proposed to estimate patient-specific pharmacokinetic parameters (80), relatively few methods have been developed to leverage vascular imaging data to estimate intratumoral drug distribution. Of note, Tagami *et al*. estimated intratumoral drug distribution *via* encapsulation of drug with a magnetic resonance imaging (MRI) contrast agent. Changes in MR T_1 relaxation time were measured and correlated with distribution of drug within tumors (94).

In this Appendix, we propose the use of DCE-MRI to estimate the intratumoral distribution of doxorubicin. Doxorubicin, which is a standard of care cytotoxic agent used in the treatment of TNBC, has been found to diffuse only 100 µm from vessels (228). Further, parameters extracted from DCE-MRI have been shown to be predictive of tumor response to therapy (92). In this preliminary work, we assess tumor vasculature in an *in vivo* model of breast cancer. We further propose a method to register *ex vivo* histology with *in vivo* MRI. We hypothesize that DCE-MRI parameters, which provide spatially-resolved measures of tumor perfusion will correlate with doxorubicin distribution, allowing for spatially-resolved intratumoral dose estimates.

A.4 Methods

A.4.1 In vivo Tumor Model

Experiments were performed in the MDA-MB-231 model of TNBC. MDA-MB-231 cells were obtained through American Type Culture Collection (ATCC, http://www.atcc.org) and maintained in culture according to ATCC recommendations. Prior to injection, cells were grown to 80-90% confluency at 37°C in 5% CO_2. 2×10^6 MDA-MB-231 cells suspended in 100 µL of serum-free DMEM media with 20% growth factor-reduced Matrigel were injected subcutaneously into the left flank of nude athymic female mice (Jackson Laboratories) ($n = 12$). Tumors were monitored weekly with caliper measurements (ellipsoid tumor volume = (length × width^2) / 2) (232) and grown to an average of 502 ($\pm$282) mm^3 at the time of imaging. All procedures were approved by our institution's animal care and use committee.

A.4.2 Doxorubicin Distribution

Doxorubicin hydrochloride was obtained from Sigma Aldrich and diluted to a stock concentration of 10 mM in sterile saline. 250 µL aliquots of doxorubicin were stored at -80°C prior to use.

Each mouse received 20 mg/kg of doxorubicin diluted in 100 µL saline *via* IV jugular catheter injection. Immediately following treatment, mice were imaged *via* MRI, and tumors were harvested after the imaging experiments (approximately 3 hours after doxorubicin injection) for histology. Tumors were sliced in half in an orientation approximately matched to the imaging planes. Each half was subsequently embedded in optimal cutting temperature compound doped with 2% by volume Optiray 320 (Guerbet, Bloomington, IN), frozen in liquid nitrogen, and stored at -80°C prior to histological sectioning. Optiray is a radiopaque iodinated contrast agent. The *ex vivo* sample was imaged *via* micro-computed tomography (microCT) and digital photography to facilitate registration of histological sections to *in vivo* images. An overview of the experimental approach is shown in Figure A.1.

A.4.3 Image Acquisition

A.4.3.1 Magnetic Resonance Imaging

Mice were imaged on a 9.4T MR scanner (Agilent Technologies, Palo Alto, CA) with a 38 mm quadrature coil (Doty Scientific, Columbia, SC). During image acquisition, the mice were anesthetized using a 2%–98% isoflurane–oxygen mixture, and body temperature was maintained *via* a flow of warm air through the magnet bore. Each animal was placed in a custom-built restraint and loaded into the scanner. Temperature and respiratory rate were monitored throughout the imaging experiment. The imaging experiments outlined below follow those in Barnes *et al* (233).

The tumor region was first localized *via* 3D gradient echo scout images. High-resolution T_2-weighted images of the entire tumor volume were acquired using a fast spin echo pulse sequence with the following parameters: TR = 5500 ms, effective TE = 35.6 ms, 15 slices, 1 mm slice thickness, and an acquisition matrix of $128 \times 128 \times 15$ over a $28 \times 28 \times 15$ mm^3 field of view (FOV). This yielded a voxel size of $0.22 \times 0.22 \times 1$ mm^3.

Pre-contrast T_1 maps were obtained using a multi-slice inversion recovery snapshot FLASH (Fast Low Angle Shot) gradient echo sequence with an adiabatic inversion pulse with seven inversion times (TI) ranging from 250 to 10,000 ms (250, 450, 830, 1,500, 2,700, 5,000, 10,000 ms). Scan acquisition parameters were as follows: TR/TE = 100/2.1 ms, $\alpha = 25°$, *NEX* = 2,

15 slices, 1 mm slice thickness, and an acquisition matrix of 64×64 over a $28 \times 28 \times 15$ mm^3 FOV, yielding a voxel size of $0.44 \times 0.44 \times 1$ mm^3. Dynamic T_1-weighted images were acquired using a spoiled gradient echo sequence at a temporal resolution of 12.8 s for approximately 20 min with the following parameters: TR/TE = 100 ms/2.1 ms, $\alpha = 25º$, $NEX = 2$. These sequences used the same acquisition matrix and FOV as the pre-contrast T_1 map. Baseline images were acquired for approximately 2.5 min before a bolus of 0.05 mmol/kg of Gado-DTPA (BioPAL, Worchester, MA) was administered through the jugular catheter over 3 seconds using an automated syringe pump (Harvard Apparatus, Holliston, MS) at a rate of 2.4 mL/min

A.4.2.2 Micro-Computed Tomography

The tumor volume, embedded in an iodinated contrast-doped OCT block, was imaged *via* microCT. The frozen tissue blocks were imaged on the Scanco vivaCT80 (Scanco Medical, Brüttisellen, Switzerland). The block was identified from a scout scan. The entire frozen block was imaged with an isotropic voxel size of 78 μm^3 with X-ray source settings at 45 kVp and 177 mA, 250 projections per 180°, and an integration time of 100 ms.

A.4.2.3 Blockface imaging

Following microCT, the tissue block was serially sectioned on a cryotome. With the use of a Canon EOS Rebel XTi digital camera with a 18- to 300-mm zoom lens, the block was digitally photographed every 50 μm prior to cutting. The in-plane resolution of these images was 70 μm isotropic. Every 1 mm, three 5-μm thick sections were mounted on slides for histological processing (described below). The blockface images were manually cropped to remove background, and the images were stacked to create a 3D blockface volume. To correct for slight block movements during the sectioning procedure, all images were aligned *via* a rigid registration to create an aligned gross tissue volume.

A.4.2.4 Histology

Following antigen retrieval, the tissue sections were stained with an anti-CD31 antibody (ab28364, Abcam Cambridge, MA) to visualize tumor vasculature. Doxorubicin is intrinsically fluorescent with excitation and emission peaks near 480 and 580 nm, respectively (234). A DAPI counter-stain was used to visualize nuclei. Slides were digitally scanned in brightfield (CD-31)

and fluorescence (DAPI and doxorubicin) with a 10× objective on the Aperio Versa 200 Slide Scanner (Leica Microsystems Inc, Buffalo Grove, IL). The brightfield and fluorescent images have resolutions of 0.547 μm and 0.648 μm isotropic, respectively.

A.4.3 Image Registration

To assess the correlation of doxorubicin distribution with *in vivo* MRI, the histological sections must first be registered to *in vivo* images. We propose the registration scheme outlined in Figure A.1. Briefly, the blockface volume is registered to the microCT volume *via* a rigid registration. The high resolution T_2-weighted anatomical image is then registered to the co-registered microCT/blockface volume *via* a nonrigid registration procedure. Specifically, the microCT is used to delineate the frozen tumor sample boundary, and the textural information in the blockface volume is used to drive the elastic registration. Finally, the histological sections are registered to their corresponding blockface images. In this way, the histological sections can be aligned with the *in vivo* MRI.

A.4.4 Image processing

A region of interest (ROI) was manually drawn around the tumor using the T_2-weighted images, and only those voxels within the tumor were used in the analyses outlined below. Pre-contrast T_1 maps were computed by fitting data collected from the inversion recovery snapshot sequence. This signal from these experiments can be described:

$$S(TI) = S_0 \left| \left(1 - 2e^{-TI/T_1} + e^{-TR/T_1}\right) \right| ,$$

where S_0 and S are the signal intensities at equilibrium and the inversion time (TI), respectively. The signal intensity measured from the spoiled gradient echo sequence is given by:

$$S(t) = S_0 \frac{\sin(\alpha)\left(1 - e^{-TR/T_1}\right)}{1 - \cos(\alpha)e^{-TR/T_1}} ,$$

where S_0 is a constant describing the scanner gain and proton density, α is the flip angle, and TR is the repetition time (we assume that TE $\ll T_2^*$). Further, we assume the fast exchange limit (FXL) model (235), and thus the longitudinal relaxation time is described by:

$$R_1 \equiv \frac{1}{T_1} = rC_t(t) + \frac{1}{T_{10}} ,$$

134

Figure A.1: Overview of registration procedure. Immediately following MRI experiments, the tumor is harvested and sliced in half in an orientation approximately matched to the imaging planes. Each half is subsequently embedded in optimal cutting temperature compound doped with 2% by volume Optiray 320 and flash-frozen. The frozen tissue blocks are imaged *via* microCT and subsequently sectioned. During sectioning, the exposed blockface is serially photographed to construct a gross tissue volume. Finally, the histology slides are imaged *via* brightfield and fluorescence. These slides are then registered to the gross tissue volume. The gross tissue volume, in turn, is registered to the microCT image. Finally, this volume is registered to a high resolution anatomical MR image. In this way, histology sections can be registered to *in vivo* MRI.
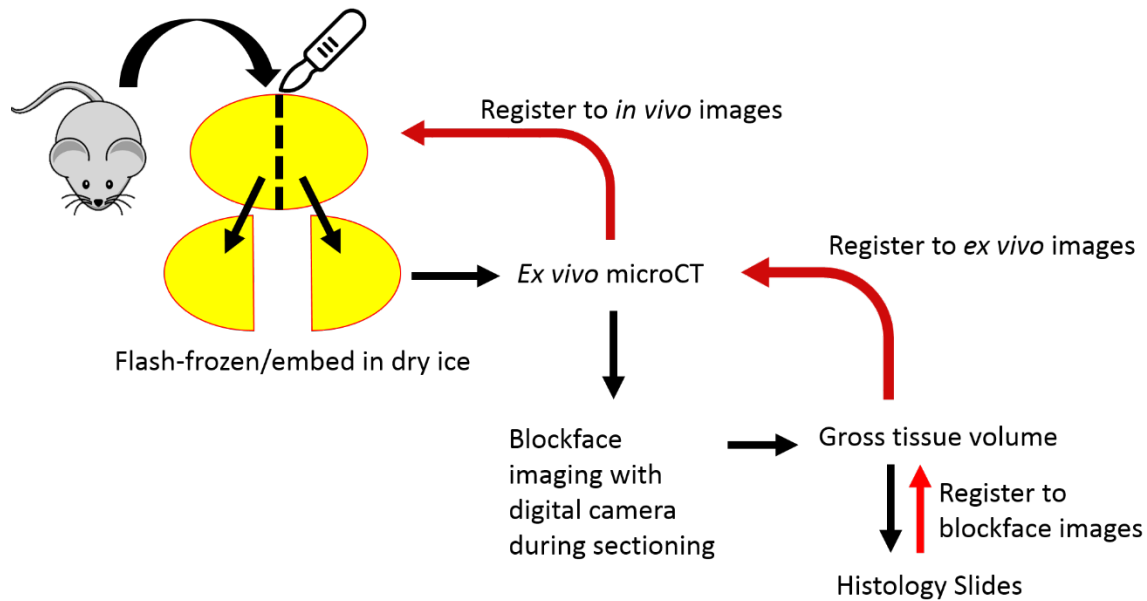
where r is the relaxivity for Gado-DTPA at 9.4T (4.7 mM^{-1}s^{-1}), $C_t(t)$ is the time-varying concentration of the contrast in the tissue, and T_{10} is the pre-contrast T_1 value. The dynamic T_1-weighted data can then be fit to the standard Tofts–Kety model:

$$C_t(t) = K^{trans} \int_0^t C_p(\tau) e^{\frac{-K^{trans}}{v_e}(t-\tau)} d\tau \, ,$$

where K^{trans} is the contrast agent transfer rate, $C_p(t)$ is the concentration of contrast in the blood plasma, and v_e is the extravascular extracellular volume fraction. Physiologically, K^{trans} is related to vessel perfusion and permeability. A population-derived vascular input function was used for $C_p(t)$ (236). Voxel-wise estimates were made for each parameter (K^{trans} and v_e) using a nonlinear least squares optimization routine implemented in MATLAB (Natick, MA).

A.5 Results

A.5.1 Sample Images

A sample *in vivo* MRI dataset is illustrated in Figure A.2. The T_1-weighted timecourses are analyzed with the standard Tofts-Kety model to extract parameter maps. These maps illustrate a common pattern of vascularity in these tumors. The tumor periphery is often well perfused, and correspondingly high K^{trans} values are observed in these regions. The tumor core often become necrotic due to poor perfusion. This is reflected by the small K^{trans} values in the tumor centers.

The *ex vivo* images corresponding to the tumor shown in Figure A.2 are shown in Figure A.3. The blockface images provide intratumoral textural information while the microCT image provides a means to precisely segment the tumor within the block. The image sets can, in theory, be combined to perform a non-rigid registration to the *in vivo* dataset.

A.6 Discussion

Building towards patient-specific treatment response predictions, we proposed and validated a coupled pharmacokinetic/pharmacodynamic model of doxorubicin treatment response *in vitro* (177). Scaling the model to the *in vivo* environment presents several challenges. Specifically, tumor microenvironmental heterogeneity can significantly impact response to therapy. In anticipation of this heterogeneity, we propose the use of quantitative MRI to account for variable tumor perfusion. In this work, we present initial data to assess the utility of DCE-MRI to estimate intratumoral distribution of doxorubicin. We note that DCE-MRI provides a functional

Figure A.2: Sample *in vivo* MRI dataset. T_2-weighted anatomical images for each mouse are first collected using a fast spin echo sequence (a – c). Following estimation of the T_{10} map, the mouse is injected with contrast agent and serially imaged. The T_1-weighted image timecourses are analyzed with the standard Tofts-Kety to measure tumor vascular properties. Voxel-wise maps of K^{trans} are shown in (d – f). High K^{trans} values are observed on the tumor periphery with relatively small values of K^{trans} in the tumor center
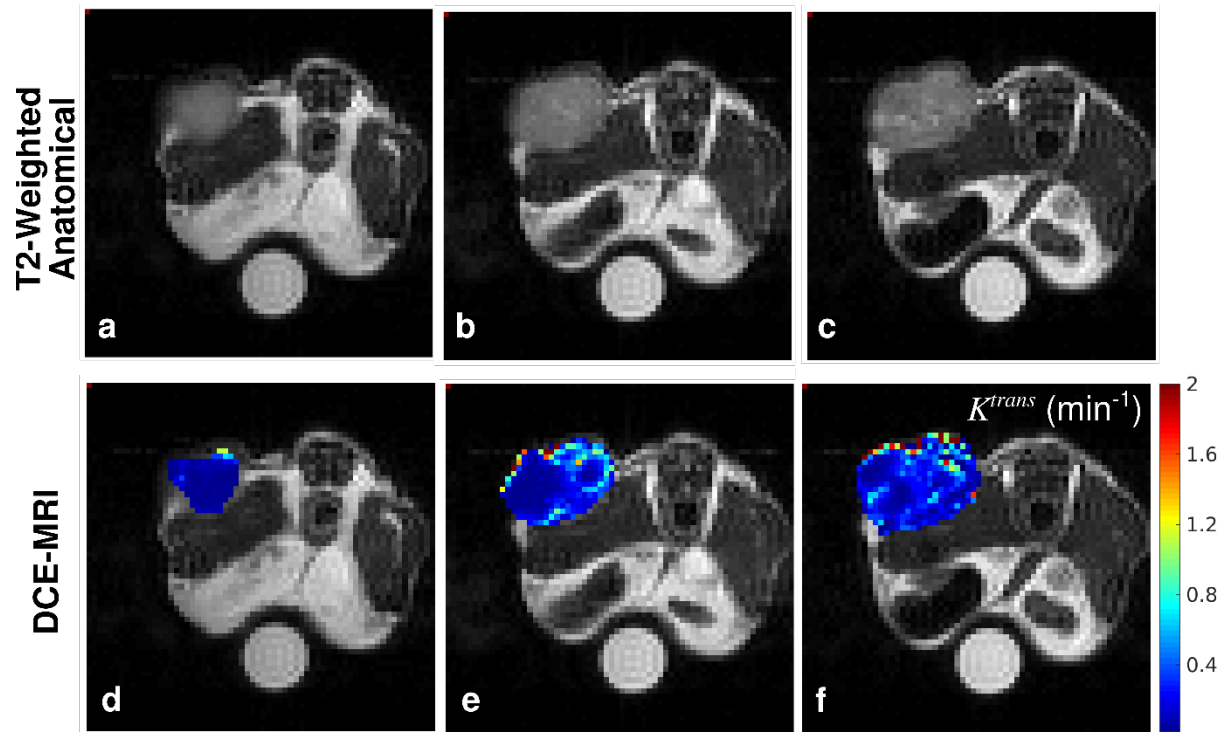
Figure A.3: Sample *ex vivo* dataset. The frozen tissue block is imaged *via* digital photography (a) and X-ray micro-computed tomography (b). The blockface images provide intratumoral textural information that is not available on the microCT image. The microCT provides clearly-delineated boundaries of each tumor sample. Of note, the OCT used to freeze this block was doped with 0.5% by volume Optiray 320.
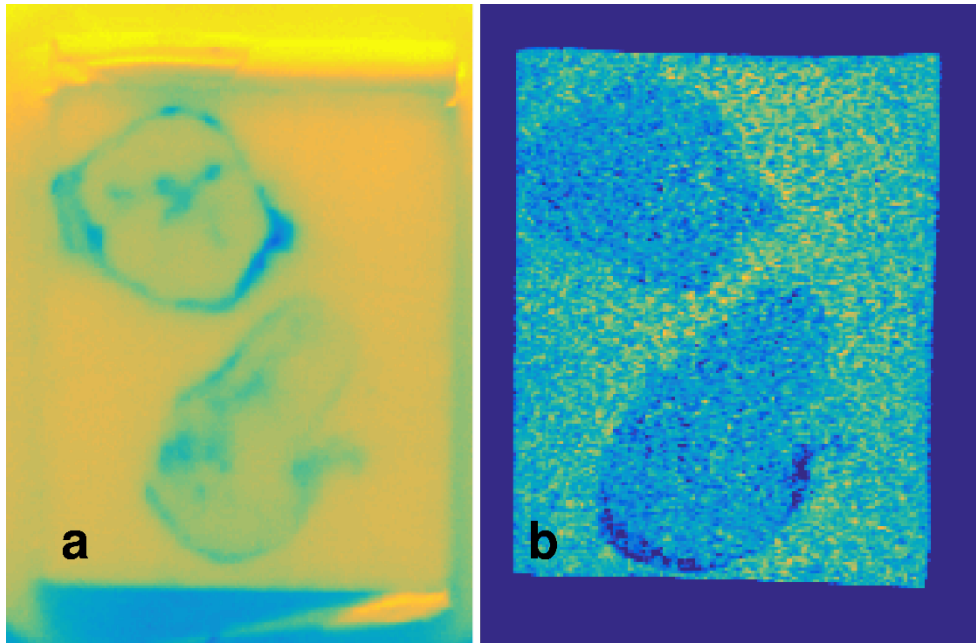
assessment of tumor vasculature and that microCT and blockface imaging represent a promising approach to register histology to *in vivo* MRI.

Given the preliminary nature of this work, the limitations are numerous. The registration pipeline remains to be constructed, and we were unable to collect histological images of doxorubicin distribution. Additionally, the current dataset was collected at a single timepoint following doxorubicin injection. Further, it is likely that increased image resolutions will be necessary to establish the relationship between drug distribution and parameter values derived from DCE-MRI studies.

Non-invasive imaging represents a promising pathway to scale the proposed treatment response model *in vivo*. To realize this goal, a relationship between imaging measures and intratumoral drug distribution must first be established. With this proposal, we aim to develop a precise measure of delivered chemotherapeutic dose to complement treatment response measurements.

REFERENCES

1. National Research Council (US) Committee on A Framework for Developing a New Framework for Developing a New Taxonomy of Disease, Taxonomy of. Toward Precision Medicine. Towar. Precis. Med. Build. a Knowl. Netw. Biomed. Res. a New Taxon. Dis. National Academies Press (US); 2011.

2. Garraway LA, Verweij J, Ballman K V. Precision oncology: an overview. J Clin Oncol. 2013;31:1803–5.

3. Garraway LA. Genomics-Driven Oncology: Framework for an Emerging Paradigm. J Clin Oncol. 2013;31:1806–14.

4. Olopade OI, Grushko TA, Nanda R, Huo D. Advances in breast cancer: Pathways to personalized medicine. Clin Cancer Res. 2008;14:7988–99.

5. Romond EH, Perez EA, Bryant J, Suman VJ, Geyer CE, Davidson NE, et al. Trastuzumab plus Adjuvant Chemotherapy for Operable HER2-Positive Breast Cancer. N Engl J Med. 2005;353:1673–84.

6. Trédan O, Galmarini CM, Patel K, Tannock IF. Drug resistance and the solid tumor microenvironment. J Natl Cancer Inst. 2007;99:1441–54.

7. Jain RK. Normalizing tumor microenvironment to treat cancer: bench to bedside to biomarkers. J Clin Oncol. 2013;31:2205–18.

8. Jain RK. Normalization of Tumor Vasculature: An Emerging Concept in Antiangiogenic Therapy. Science. 2005;307:58–62.

9. Rudek M., Sparreboom A, Garrett-Mayer E., Armstrong D., Wolff A., Verweij J, et al. Factors affecting pharmacokinetic variability following doxorubicin and docetaxel-based therapy. Eur J Cancer. 2004;40:1170–8.

10. Weinshilboum RM, Wang L. Pharmacogenetics and Pharmacogenomics: Development, Science, and Translation. Annu Rev Genomics Hum Genet. 2006;7:223–45.

11. Citron ML, Berry DA, Cirrincione C, Hudis C, Winer EP, Gradishar WJ, et al. Randomized trial of dose-dense versus conventionally scheduled and sequential versus concurrent combination chemotherapy as postoperative adjuvant treatment of node-positive primary breast cancer: First report of Intergroup Trial C9741/Cancer and Leukemia. J Clin Oncol. 2003;21:1431–9.

12. Montagna E, Cancello G, Dellapasqua S, Munzone E, Colleoni M. Metronomic therapy and breast cancer: A systematic review. Cancer Treat Rev. 2014;40:942–50.

13. Sorace AG, Quarles CC, Whisenant JG, Hanker AB, McIntyre JO, Sanchez VM, et al. Trastuzumab improves tumor perfusion and vascular delivery of cytotoxic therapy in a murine model of HER2+ breast cancer: preliminary results. Breast Cancer Res Treat. 2016;155:273–84.

14. Moreno L, Pearson AD. How can attrition rates be reduced in cancer drug discovery? Expert Opin Drug Discov. 2013;8:363–8.

15. Li X, Abramson RG, Arlinghaus LR, Kang H, Chakravarthy AB, Abramson VG, et al. Multiparametric magnetic resonance imaging for predicting pathological response after the first cycle of neoadjuvant chemotherapy in breast cancer. Invest Radiol. 2015;50:195–204.

16. Gillies RJ, Verduzco D, Gatenby RA. Evolutionary dynamics of carcinogenesis and why targeted therapy does not work. Nat Rev Cancer. 2012;12:487–93.

17.   Rockne R, Alvord Jr. EC, Rockhill JK, Swanson KR. A mathematical model for brain tumor response to radiation therapy. J Math Biol. 2009;58:561–78.

18.   Altrock PM, Liu LL, Michor F. The mathematics of cancer: integrating quantitative models. Nat Rev Cancer. 2015;15:730–45.

19.   Yankeelov TE, Atuegwu N, Hormuth D, Weis JA, Barnes SL, Miga MI, et al. Clinically relevant modeling of tumor growth and treatment response. Sci Transl Med. 2013;5:187ps9.

20.   Gatenby RA, Silva AS, Gillies RJ, Frieden BR. Adaptive therapy. Cancer Res. 2009;69:4894–903.

21.   Atuegwu NC, Arlinghaus LR, Li X, Welch EB, Chakravarthy BA, Gore JC, et al. Integration of diffusion-weighted MRI data and a simple mathematical model to predict breast tumor cellularity during neoadjuvant chemotherapy. Magn Reson Med. 2011;66:1689–96.

22.   Anderson AR, Quaranta V. Integrative mathematical oncology. Nat Rev Cancer. 2008;8:227–34.

23.   Anderson ARA. A hybrid mathematical model of solid tumour invasion: the importance of cell adhesion. Math Med Biol. 2005;22:163–86.

24.   Yankeelov TE, Quaranta V, Evans KJ, Rericha EC. Toward a science of tumor forecasting for clinical oncology. Cancer Res. 2015;75:918–23.

25.   Box GEP. Robustness in the Strategy of Scientific Model Building. 1979.

26.   Yankeelov TE, An G, Saut O, Luebeck EG, Popel AS, Ribba B, et al. Multi-scale Modeling in Clinical Oncology: Opportunities and Barriers to Success. Ann Biomed Eng. 2016;44:2626–41.

27.   Conley RH, Meszoely IM, Weis JA, Pheiffer TS, Arlinghaus LR, Yankeelov TE, et al. Realization of a biomechanical model-assisted image guidance system for breast cancer surgery using supine MRI. Int J Comput Assist Radiol Surg. 2015;10:1985–96.

28.   Fisher B, Slack N, Katrych D, Wolmark N. Ten year follow-up results of patients with carcinoma of the breast in a co-operative clinical trial evaluating surgical adjuvant chemotherapy. Surg Gynecol Obstet. 1975;140:528–34.

29.   Goodman LS, Wintrobe MM, Dameshek W, Goodman MJ, Gilman A, McLennan MT, et al. Nitrogen Mustard Therapy. J Am Med Assoc. 1946;132:126-132.

30.   Liedtke C, Mazouni C, Hess KR, André F, Tordai A, Mejia JA, et al. Response to neoadjuvant therapy and long-term survival in patients with triple-negative breast cancer. J Clin Oncol. 2008;26:1275–81.

31.   Chatterjee K, Zhang J, Honbo N, Karliner JS. Doxorubicin cardiomyopathy. Cardiology. 2010;115:155–62.

32.   Fisher B. From Halsted to prevention and beyond: advances in the management of breast cancer during the twentieth century. Eur J Cancer. 1999;35:1963–73.

33.   Skipper HE. Kinetics of mammary tumor cell growth and implications for therapy. Cancer. 1971;28:1479–99.

34.   Fisher B, Carbone P, Economou SG, Frelick R, Glass A, Lerner H, et al. L-Phenylalanine Mustard (L-PAM) in the Management of Primary Breast Cancer. N Engl J Med. 1975;292:117–22.

35.   Bonadonna G, Brusamolino E, Valagussa P, Rossi A, Brugnatelli L, Brambilla C, et al. Combination Chemotherapy as an Adjuvant Treatment in Operable Breast Cancer. N Engl

J Med. 1976;294:405–10.

36. Hortobagyi GN. High-dose chemotherapy for primary breast cancer: facts versus anecdotes. J Clin Oncol. 1999;17:25–9.

37. Stadtmauer EA, O'Neill A, Goldstein LJ, Crilley PA, Mangan KF, Ingle JN, et al. Conventional-dose chemotherapy compared with high-dose chemotherapy plus autologous hematopoietic stem-cell transplantation for metastatic breast cancer. Philadelphia Bone Marrow Transplant Group. N Engl J Med. 2000;342:1069–76.

38. Norton L, Simon R. Growth curve of an experimental solid tumor following radiotherapy. J Natl Cancer Inst. 1977;58:1735–41.

39. Norton L. A Gompertzian model of human breast cancer growth. Cancer Res. 1988;48:7067–71.

40. Simon R, Norton L. The Norton-Simon hypothesis: designing more effective and less toxic chemotherapeutic regimens. Nat Clin Pract Oncol. 2006;3:406–7.

41. Goldie JH, Coldman AJ. A mathematic model for relating the drug sensitivity of tumors to their spontaneous mutation rate. Cancer Treat Rep. 1979;63:1727–33.

42. Bonadonna G, Zambetti M, Moliterni A, Gianni L, Valagussa P. Clinical relevance of different sequencing of doxorubicin and cyclophosphamide, methotrexate, and Fluorouracil in operable breast cancer. J Clin Oncol. 2004;22:1614–20.

43. Browder T, Butterfield CE, Kräling BM, Shi B, Marshall B, O'Reilly MS, et al. Antiangiogenic scheduling of chemotherapy improves efficacy against experimental drug-resistant cancer. Cancer Res. 2000;60:1878–86.

44. Foo J, Michor F. Evolution of resistance to anti-cancer therapy during general dosing schedules. J Theor Biol. 2010;263:179–88.

45. Byrne HM. Dissecting cancer through mathematics : from the cell to the animal model. Nat Rev Cancer. 2010;10:221–30.

46. Gatenby RA. A change of strategy in the war on cancer. Nature. 2009;459:508–9.

47. Miller AA. Body Surface Area in Dosing Anticancer Agents: Scratch the Surface! J Natl Cancer Inst. 2002;94:1822–31.

48. Redlarski G, Palkowski A, Krawczuk M, Meeh K, Bois D Du, Bois EF Du, et al. Body surface area formulae: an alarming ambiguity. Sci Rep. 2016;6:27966.

49. Pinkel D. The Use of Body Surface Area as a Criterion of Drug Dosage in Cancer Chemotherapy. Cancer Res. 1958;18:853-856.

50. Blanchard OL, Smoliga JM. Translating dosages from animal models to human clinical trials--revisiting body surface area scaling. FASEB J. 2015;29:1629–34.

51. Gehan EA, George SL. Estimation of human body surface area from height and weight. Cancer Chemother reports. 1970;54:225–35.

52. Sawyer M, Ratain MJ. Body Surface Area as a Determinant of Pharmacokinetics and Drug Dosing. Invest New Drugs. 2001;19:171–7.

53. Gurney H. Dose calculation of anticancer drugs: a review of the current practice and introduction of an alternative. J Clin Oncol. 1996;14:2590–611.

54. Bernier J, Hall EJ, Giaccia A. Timeline: Radiation oncology: a century of achievements. Nat Rev Cancer. 2004;4:737–47.

55. Prise KM, Schettino G, Folkard M, Held KD. New insights on cell death from radiation exposure. Lancet Oncol. 2005;6:520–8.

56.	Wouters BG. Cell death after irradiation: how, when and why cells die. In: Joiner MC, van der Kogel AJ, editors. Basic Clin Radiobiol. 4th ed. CRC Press; 2009. page 27–40.

57.	Joiner MC. Quantifying cell kill and cell survival. In: Joiner MC, van der Kogel AJ, editors. Basic Clin Radiobiol. 4th ed. 4: CRC Press; 2009. page 41–55.

58.	Douglas BG, Fowler JF. The effect of multiple small doses of x rays on skin reactions in the mouse and a basic interpretation. Radiat Res. 1976;66:401–26.

59.	Curtis SB. Lethal and Potentially Lethal Lesions Induced by Radiation --- A Unified Repair Model. Radiat Res. 1986;106:252–70.

60.	Pajonk F, Vlashi E, McBride WH. Radiation resistance of cancer stem cells: the 4 R's of radiobiology revisited. Stem Cells. 2010;28:639–48.

61.	Withers HR, Thames HD, Peters LJ. A new isoeffect curve for change in dose per fraction. Radiother Oncol. 1983;1:187–91.

62.	Bentzen SM, Joiner MC. The linear-quadratic approach in clinical practice. In: Joiner M, Kogel A van der., editors. Basic Clin Radiobiol. 4th ed. CRC Press; 2009. page 120–34.

63.	Bourhis J, Overgaard J, Audry H, Ang KK, Saunders M, Bernier J, et al. Hyperfractionated or accelerated radiotherapy in head and neck cancer: a meta-analysis. Lancet. 2006;368:843–54.

64.	Whelan TJ, Pignol J-P, Levine MN, Julian JA, MacKenzie R, Parpia S, et al. Long-Term Results of Hypofractionated Radiation Therapy for Breast Cancer. N Engl J Med. 2010;362:513–20.

65.	Verellen D, Ridder M De, Linthout N, Tournel K, Soete G, Storme G. Innovations in image-guided radiotherapy. Nat Rev Cancer. 2007;7:949–60.

66.	Oelkfe U, Scholz C. Dose Calculation Algorithms. New Technol Radiat Oncol. 2006. page 187–96.

67.	Andreo P. Monte Carlo techniques in medical radiation physics. Phys Med Biol. 1991;36:861–920.

68.	Hubbell JH, Seltzer SM. Tables of X-ray mass attenuation coefficients and mass energy-absorption coefficients 1 keV to 20 MeV for elements $Z= 1$ to 92 and 48 additional substances of dosimetric interest. National Inst. of Standards and Technology-PL; 1995.

69.	Jackson DF, Hawkes DJ. X-ray attenuation coefficients of elements and mixtures. Phys Rep. 1981;70:169–233.

70.	Schneider W, Bortfeld T, Schlegel W. Correlation between CT numbers and tissue parameters needed for Monte Carlo simulations of clinical dose distributions. Phys Med Biol. 2000;45:459–78.

71.	Brahme A. Dosimetric Precision Requirements in Radiation Therapy. Acta Radiol Oncol. 1984;23:379–91.

72.	Boyer AL, Schultheiss T. Effects of dosimetric and clinical uncertainty on complication-free local tumor control. Radiother Oncol. 1988;11:65–71.

73.	Rockne R, Rockhill JK, Mrugala M, Spence a M, Kalet I, Hendrickson K, et al. Predicting the efficacy of radiotherapy in individual glioblastoma patients in vivo: a mathematical modeling approach. Phys Med Biol. 2010;55:3271–85.

74.	Peck RW. The right dose for every patient: a key step for precision medicine. Nat Rev Drug Discov. 2015;15:145–6.

75.	Paci A, Veal G, Bardin C, Levêque D, Widmer N, Beijnen J, et al. Review of therapeutic

drug monitoring of anticancer drugs part 1 – Cytotoxics. Eur J Cancer. 2014;50:2010–9.

76. Undevia SD, Gomez-Abuin G, Ratain MJ. Pharmacokinetic variability of anticancer agents. Nat Rev Cancer. 2005;5:447–58.

77. Rousseau A, Marquet P. Application of pharmacokinetic modelling to the routine therapeutic drug monitoring of anticancer drugs. Fundam Clin Pharmacol. 2002;16:253–62.

78. Evans WE, Relling M V., Rodman JH, Crom WR, Boyett JM, Pui C-H. Conventional Compared with Individualized Chemotherapy for Childhood Acute Lymphoblastic Leukemia. N Engl J Med. 1998;338:499–505.

79. Dasgupta A, Datta P. Analytical Techniques for Measuring Concentrations of Therapeutic Drugs in Biological Fluids. Handb Drug Monit Methods. Totowa, NJ: Humana Press; 2008. page 67–86.

80. Barbolosi D, Ciccolini J, Lacarelle B, Barlési F, André N. Computational oncology — mathematical modelling of drug regimens for precision medicine. Nat Rev Clin Oncol. 2015;13:242–54.

81. Gustafson DL, Rastatter JC, Colombo T, Long ME. Doxorubicin pharmacokinetics: Macromolecule binding, metabolism, and excretion in the context of a physiologic model. J Pharm Sci. 2002;91:1488–501.

82. Rousseau A, Marquet P, Debord J, Sabot C, Lachatre G. Adaptive Control Methods for the Dose Individualisation of Anticancer Agents. Clin Pharmacokinet. 2000;38:315–53.

83. Barbolosi D, Ciccolini J, Meille C, Elharrar X, Faivre C, Lacarelle B, et al. Metronomics chemotherapy: Time for computational decision support. Cancer Chemother Pharmacol. 2014;74:647–52.

84. Joerger M, Kraff S, Huitema ADR, Feiss G, Moritz B, Schellens JHM, et al. Evaluation of a Pharmacology-Driven Dosing Algorithm of 3-Weekly Paclitaxel Using Therapeutic Drug Monitoring. Clin Pharmacokinet. 2012;51:607–17.

85. Calvert AH, Newell DR, Gumbrell LA, O'Reilly S, Burnell M, Boxall FE, et al. Carboplatin dosage: prospective evaluation of a simple formula based on renal function. J Clin Oncol. 1989;7:1748–56.

86. Weinshilboum R, Wang L. Pharmacogenomics: bench to bedside. Nat Rev Drug Discov. 2004;3:739–48.

87. Hanahan D, Weinberg RA. Hallmarks of Cancer: The Next Generation. Cell. 2011;144:646–74.

88. Teicher BA. Hypoxia and drug resistance. Cancer Metastasis Rev. 1994;13:139–68.

89. Vaupel P. Tumor microenvironmental physiology and its implications for radiation oncology. Semin Radiat Oncol. 2004;14:198–206.

90. Minchinton AI, Tannock IF. Drug penetration in solid tumours. Nat Rev Cancer. 2006;6:583–92.

91. Li X, Arlinghaus LR, Ayers GD, Chakravarthy a B, Abramson RG, Abramson VG, et al. DCE-MRI analysis methods for predicting the response of breast cancer to neoadjuvant chemotherapy: pilot study findings. Magn Reson Med. 2013;71:1592–602.

92. Yankeelov TE, Arlinghaus LR, Li X, Gore JC. The Role of Magnetic Resonance Imaging Biomarkers in Clinical Trials of Treatment Response in Cancer. Semin Oncol. 2011;38:16–25.

93. Venkatasubramanian R, Arenas R, Henson M, Forbes N. Mechanistic modelling of dynamic

MRI data predicts that tumour heterogeneity decreases therapeutic response. Br J Cancer. 2010;103:486–97.

94. Tagami T, Foltz WD, Ernsting MJ, Lee CM, Tannock IF, May JP, et al. MRI monitoring of intratumoral drug delivery and prediction of the therapeutic effect with a multifunctional thermosensitive liposome. Biomaterials. 2011;32:6570–8.

95. Kim M, Gillies RJ, Rejniak KA. Current advances in mathematical modeling of anti-cancer drug penetration into tumor tissues. Pharmacol Anti-Cancer Drugs. 2013;3:278.

96. Lehmann BD, Bauer JA, Chen X, Sanders ME, Chakravarthy AB, Shyr Y, et al. Identification of human triple-negative breast cancer subtypes and preclinical models for selection of targeted therapies. J Clin Invest. 2011;121:2750–67.

97. Eisenhauer EA, Therasse P, Bogaerts J, Schwartz LH, Sargent D, Ford R, et al. New response evaluation criteria in solid tumours: Revised RECIST guideline (version 1.1). Eur J Cancer. 2009;45:228–47.

98. Atuegwu NC, Gore JC, Yankeelov TE. The integration of quantitative multi-modality imaging data into mathematical models of tumors. Phys Med Biol. 2010;55:2429–49.

99. Pickles MD, Gibbs P, Lowry M, Turnbull LW. Diffusion changes precede size reduction in neoadjuvant treatment of breast cancer. Magn Reson Imaging. 2006;24:843–7.

100. Dose Schwarz J, Bader M, Jenicke L, Hemminger G, Jänicke F, Avril N. Early prediction of response to chemotherapy in metastatic breast cancer using sequential 18F-FDG PET. J Nucl Med. 2005;46:1144–50.

101. Kinahan PE, Fletcher JW. Positron emission tomography-computed tomography standardized uptake values in clinical practice and assessing response to therapy. Semin Ultrasound CT MR. 2010;31:496–505.

102. Dawson S-J, Tsui DWY, Murtaza M, Biggs H, Rueda OM, Chin S-F, et al. Analysis of Circulating Tumor DNA to Monitor Metastatic Breast Cancer. N Engl J Med. 2013;368:1199–209.

103. Thress KS, Paweletz CP, Felip E, Cho BC, Stetson D, Dougherty B, et al. Acquired EGFR C797S mutation mediates resistance to AZD9291 in non–small cell lung cancer harboring EGFR T790M. Nat Med. 2015;21:560–2.

104. Siravegna G, Mussolin B, Buscarino M, Corti G, Cassingena A, Crisafulli G, et al. Clonal evolution and resistance to EGFR blockade in the blood of colorectal cancer patients. Nat Med. 2015;21:795–801.

105. Garcia-Murillas I, Schiavon G, Weigelt B, Ng C, Hrebien S, Cutts RJ, et al. Mutation tracking in circulating tumor DNA predicts relapse in early breast cancer. Sci Transl Med. 2015;7:302ra133-302ra133.

106. Li X, Abramson RG, Arlinghaus LR, Kang H, Chakravarthy AB, Abramson VG, et al. Combined DCE-MRI and DW-MRI for Predicting Breast Cancer Pathological Response After the First Cycle of Neoadjuvant Chemotherapy. Invest Radiol. 2015;50:195–204.

107. Harrold JM, Parker RS. Clinically relevant cancer chemotherapy dose scheduling via mixed-integer optimization. Comput Chem Eng. 2009;33:2042–54.

108. Liu Y, Sadowski SM, Weisbrod AB, Kebebew E, Summers RM, Yao J. Patient specific tumor growth prediction using multimodal images. Med Image Anal. 2014;18:555–66.

109. Shi J, Alagoz O, Erenay FS, Su Q. A survey of optimization models on cancer chemotherapy treatment planning. Ann Oper Res. 2011;221:331–56.

110. Singer DS, Jacks T, Jaffee E. A U.S. "Cancer Moonshot" to accelerate cancer research. Science. 2016;353.

111. Riss TL, Niles AL, Minor L. Cell Viability Assays Assay Guidance Manual. Assay Guid Man. 2004;1–23.

112. Pusztai L, Wagner P, Ibrahim N, Rivera E, Theriault R, Booser D, et al. Phase II study of tariquidar, a selective P-glycoprotein inhibitor, in patients with chemotherapy-resistant, advanced breast carcinoma. Cancer. 2005;104:682–91.

113. Fox E, Bates SE. Tariquidar (XR9576): a P-glycoprotein drug efflux pump inhibitor. Expert Rev Anticancer Ther. 2007;7:447–59.

114. Davidson D, Amrein L, Panasci L, Aloyz R. Small Molecules, Inhibitors of DNA-PK, Targeting DNA Repair, and Beyond. Front Pharmacol. 2013;4:5.

115. Helleday T, Petermann E, Lundin C, Hodgson B, Sharma RA. DNA repair pathways as targets for cancer therapy. Nat Rev Cancer. 2008;8:193–204.

116. Zhao Y, Thomas HD, Batey MA, Cowell IG, Richardson CJ, Griffin RJ, et al. Preclinical Evaluation of a Potent Novel DNA-Dependent Protein Kinase Inhibitor NU7441. Cancer Res. 2006;66:5354–62.

117. Heppner GH. Tumor Heterogeneity. Cancer Res. 1984;44.

118. Marusyk A, Polyak K. Tumor heterogeneity: Causes and consequences. Biochim Biophys Acta - Rev Cancer. 2010;1805:105–17.

119. Gerlinger M, Rowan AJ, Horswell S, Larkin J, Endesfelder D, Gronroos E, et al. Intratumor Heterogeneity and Branched Evolution Revealed by Multiregion Sequencing. N Engl J Med. 2012;366:883–92.

120. Mechetner E, Kyshtoobayeva A, Zonis S, Kim H, Stroup R, Garcia R, et al. Levels of Multidrug Resistance (MDR1) P-Glycoprotein Expression by Human Breast Cancer Correlate with in Vitro Resistance to Taxol and Doxorubicin. Clin Cancer Res. 1998;4:389–98.

121. Fisher B, Ravdin RG, Ausman RK, Slack NH, Moore GE, Noer RJ. Surgical adjuvant chemotherapy in cancer of the breast: results of a decade of cooperative investigation. Ann Surg. 1968;168:337–56.

122. Fornier M, Norton L. Dose-dense adjuvant chemotherapy for primary breast cancer. Breast Cancer Res. 2005;7:64–9.

123. Enriquez-Navas PM, Kam Y, Das T, Hassan S, Silva A, Foroutan P, et al. Exploiting evolutionary principles to prolong tumor control in preclinical models of breast cancer. Sci Transl Med. 2016;8:327ra24.

124. Hanahan D, Bergers G, Bergsland E. Less is more, regularly: metronomic dosing of cytotoxic drugs can target tumor angiogenesis in mice. J Clin Invest. 2000;105:1045–7.

125. Bocci G, Kerbel RS. Pharmacokinetics of metronomic chemotherapy: a neglected but crucial aspect. Nat Rev Clin Oncol. 2016;13:659–73.

126. Santana-Davila R, Perez EA. Treatment options for patients with triple-negative breast cancer. J Hematol Oncol. 2010;3:42.

127. Cleator S, Heller W, Coombes RC. Triple-negative breast cancer: therapeutic options. Lancet Oncol. 2007;8:235–44.

128. Kaufmann M, Hortobagyi GN, Goldhirsch A, Scholl S, Makris A, Valagussa P, et al. Recommendations from an international expert panel on the use of neoadjuvant (primary)

systemic treatment of operable breast cancer: an update. J Clin Oncol. 2006;24:1940–9.

129. Goutelle S, Maurin M, Rougier F, Barbaut X, Bourguignon L, Ducher M, et al. The Hill equation: a review of its capabilities in pharmacological modelling. Fundam. Clin. Pharmacol. 2008. page 633–48.

130. Harris LA, Frick PL, Garbett SP, Hardeman KN, Paudel BB, Lopez CF, et al. An unbiased metric of antiproliferative drug effect in vitro. Nat Methods. 2016;13:497–500.

131. Hafner M, Niepel M, Chung M, Sorger PK. Growth rate inhibition metrics correct for confounders in measuring sensitivity to cancer drugs. Nat Methods. 2016;13:521–7.

132. Eichholtz-Wirth H. Dependence of the cytostatic effect of adriamycin on drug concenration and exposure time in vitro. Br J Cancer. 1980;41:886–91.

133. Levasseur LM, Slocum HK, Rustum YM, Greco WR. Modeling of the time-dependency of in vitro drug cytotoxicity and resistance. Cancer Res. 1998;58:5749–61.

134. El-Kareh AW, Secomb TW. Two-mechanism peak concentration model for cellular pharmacodynamics of Doxorubicin. Neoplasia. 2005;7:705–13.

135. Lobo ED, Balthasar JP. Pharmacodynamic modeling of chemotherapeutic effects: application of a transit compartment model to characterize methotrexate effects in vitro. AAPS PharmSci. 2002;4:212–22.

136. Lankelma J, Fernández Luque R, Dekker H, van den Berg J, Kooi B. A new mathematical pharmacodynamic model of clonogenic cancer cell death by doxorubicin. J Pharmacokinet Pharmacodyn. 2013;40:513–25.

137. Lankelma J, Fernández Luque R, Dekker H, Pinedo HM. Simulation model of doxorubicin activity in islets of human breast cancer cells. Biochim Biophys Acta. 2003;1622:169–78.

138. Foulkes WD, Smith IE, Reis-filho JS. Triple-Negative Breast Cancer. N Engl J Med. 2010;363:1938–48.

139. Abramson VG, Lehmann BD, Ballinger TJ, Pietenpol JA. Subtyping of triple-negative breast cancer: Implications for therapy. Cancer. 2014;121:8–16.

140. Tyson DR, Garbett SP, Frick PL, Quaranta V. Fractional proliferation: a method to deconvolve cell population dynamics from single-cell data. Nat Methods. 2012;9:923–8.

141. Quaranta V, Tyson DR, Garbett SP, Weidow B, Harris MP, Georgescu W. Trait variability of cancer cells quantified by high-content automated microscopy of single cells. Methods Enzymol. 2009;467:23–57.

142. Karukstis KK, Thompson EHZ, Whiles JA, Rosenfeld RJ. Deciphering the fluorescence signature of daunomycin and doxorubicin. Biophys Chem. 1998;73:249–63.

143. Greene RF, Collins JM, Jenkins JF, Speyer JL, Myers CE. Plasma pharmacokinetics of adriamycin and adriamycinol: Implications for the design of in vitro experiments and treatment protocols. Cancer Res. 1983;43:3417–21.

144. Shin K, Klosterhoff BS, Han B. Characterization of cell-type-specific drug transport and resistance of breast cancers using tumor-microenvironment-on-chip. Mol Pharm. 2016;13:2214–23.

145. Nagasawa K, Natazuka T, Nomiyama M, Ohnishi N, Yokoyama T. Transport mechanism of anthracycline derivatives in human leukemia cell lines: uptake and efflux of daunorubicin and doxorubicin in HL60 and its resistant cells and comparison with those of pirarubicin. Biol Pharm Bull. 1996;19:100–5.

146. Tacar O, Sriamornsak P, Dass CR. Doxorubicin: an update on anticancer molecular action,

toxicity and novel drug delivery systems. J Pharm Pharmacol. 2013;65:157–70.

147. Gewirtz DA. A critical evaluation of the mechanisms of action proposed for the antitumor effects of the anthracycline antibiotics adriamycin and daunorubicin. Biochem Pharmacol. 1999;57:727–41.

148. Shen F, Chu S, Bence AK, Bailey B, Xue X, Erickson PA, et al. Quantitation of Doxorubicin Uptake, Efflux, and Modulation of Multidrug Resistance (MDR) in MDR Human Cancer Cells. J Pharmacol Exp Ther. 2008;324:95–102.

149. Bozdogan H. Model selection and Akaike's Information Criterion (AIC): The general theory and its analytical extensions. Psychometrika. 1987;52:345–70.

150. Frick PL, Paudel BB, Tyson DR, Quaranta V. Quantifying heterogeneity and dynamics of clonal fitness in response to perturbation. J Cell Physiol. 2015;230:1403–12.

151. Chang BD, Broude E V., Dokmanovic M, Zhu H, Ruth A, Xuan Y, et al. A senescence-like phenotype distinguishes tumor cells that undergo terminal proliferation arrest after exposure to anticancer agents. Cancer Res. 1999;59:3761–7.

152. Eom Y-W, Kim MA, Park SS, Goo MJ, Kwon HJ, Sohn S, et al. Two distinct modes of cell death induced by doxorubicin: apoptosis and cell death through mitotic catastrophe accompanied by senescence-like phenotype. Oncogene. 2005;24:4765–77.

153. Keizer HG, Pinedo HM, Schuurhuist GJ, Joenje H. Doxorubicin (Adriamycin) : a critical review of free radical-dependent mechanisms of cytotoxicity. Pharmacol Ther. 1990;47:219–31.

154. Maestre N, Tritton TR, Laurent G, Jaffrézou JP. Cell surface-directed interaction of anthracyclines leads to cytotoxicity and nuclear factor kappaB activation but not apoptosis signaling. Cancer Res. 2001;61:2558–61.

155. Buckland ST, Burnham KP, Augustin NH. Model Selection: An Integral Part of Inference. Biometrics. 1997;53:603–18.

156. Burnham KP, Anderson DR. Model Selection and Multimodel Inference: a Practical Information-theoretic Approach. 2nd ed. New York Springer. New York: Springer; 2002.

157. Marino S, Hogue IB, Ray CJ, Kirschner DE. A methodology for performing global uncertainty and sensitivity analysis in systems biology. J Theor Biol. 2008;254:178–96.

158. Cleveland WS, Devlin SJ. Locally Weighted Regression: An Approach to Regression Analysis by Local Fitting. J Am Stat Assoc. 1988;83:596.

159. Jackson TL. Intracellular accumulation and mechanism of action of doxorubicin in a spatio-temporal tumor model. J Theor Biol. 2003;220:201–13.

160. Eliaz RE, Nir S, Marty C, Szoka FC. Determination and Modeling of Kinetics of Cancer Cell Killing by Doxorubicin and Doxorubicin Encapsulated in Targeted Liposomes. Cancer Res. 2004;64:711–8.

161. Wilkinson DJ. Stochastic modelling for quantitative description of heterogeneous biological systems. Nat Rev Genet. 2009;10:122–33.

162. Kamen BA, Rubin E, Aisner J, Glatstein E. High-time chemotherapy or high time for low dose. J Clin Oncol. 2000;18:2935–7.

163. Piccart-Gebhart MJ. Mathematics and oncology: a match for life? J. Clin. Oncol. 2003. page 1425–8.

164. Cory S, Adams JM. The Bcl2 family: regulators of the cellular life-or-death switch. Nat Rev Cancer. 2002;2:647–56.

165. Georgescu W, Wikswo JP, Quaranta V. CellAnimation: An open source MATLAB framework for microscopy assays. Bioinformatics. 2012;28:138–9.

166. Hormuth II DA, Weis JA, Barnes SL, Miga MI, Rericha EC, Quaranta V, et al. Predicting in vivo glioma growth with the reaction diffusion equation constrained by quantitative magnetic resonance imaging data. Phys Biol. 2015;12:46006.

167. Atuegwu NC, Arlinghaus LR, Li X, Chakravarthy AB, Abramson VG, Sanders ME, et al. Parameterizing the Logistic Model of Tumor Growth by DW-MRI and DCE-MRI Data to Predict Treatment Response and Changes in Breast Cancer Cellularity during Neoadjuvant Chemotherapy. Transl Oncol. 2013;6:256–64.

168. Larsen AK, Skladanowski A. Cellular resistance to topoisomerase-targeted drugs: from drug uptake to cell death. Biochim Biophys Acta - Gene Struct Expr. 1998;1400:257–74.

169. Larsen AK, Escargueil AE, Skladanowski A. Resistance mechanisms associated with altered intracellular distribution of anticancer agents. Pharmacol Ther. 2000;85:217–29.

170. Clarke R, Leonessa F, Trock B. Multidrug Resistance/P-Glycoprotein and Breast Cancer: Review and Meta-Analysis. Semin Oncol. 2005;32:9–15.

171. Fink D, Aebi S, Howell SB. The role of DNA mismatch repair in drug resistance. Clin Cancer Res. 1998;4:1–6.

172. Bouwman P, Jonkers J. The effects of deregulated DNA damage signalling on cancer chemotherapy response and resistance. Nat Rev Cancer. 2012;12:587–98.

173. Smith GC, Jackson SP. The DNA-dependent protein kinase. Genes Dev. 1999;13:916–34.

174. Shen H, Schultz M, Kruh GD, Tew KD. Increased expression of DNA-dependent protein kinase confers resistance to adriamycin. Biochim Biophys Acta - Gen Subj. 1998;1381:131–8.

175. Prentice RL. A Generalization of the Probit and Logit Methods for Dose Response Curves. Biometrics. 1976;32:761.

176. Fallahi-Sichani M, Honarnejad S, Heiser LM, Gray JW, Sorger PK. Metrics other than potency reveal systematic variation in responses to cancer drugs. Nat Chem Biol. 2013;9:708–14.

177. McKenna MT, Weis JA, Barnes SL, Tyson DR, Miga MI, Quaranta V, et al. A Predictive Mathematical Modeling Approach for the Study of Doxorubicin Treatment in Triple Negative Breast Cancer. Sci Rep. 2017;7:5725.

178. Fowler JF. Brief summary of radiobiological principles in fractionated radiotherapy. Semin Radiat Oncol. 1992;2:16–21.

179. Elstrodt F, Hollestelle A, Nagel JHA, Gorin M, Wasielewski M, van den Ouweland A, et al. BRCA1 Mutation Analysis of 41 Human Breast Cancer Cell Lines Reveals Three New Deleterious Mutants. Cancer Res. 2006;66:41–5.

180. Gudmundsdottir K, Ashworth A. The roles of BRCA1 and BRCA2 and associated proteins in the maintenance of genomic stability. Oncogene. 2006;25:5864–74.

181. Farmer H, McCabe N, Lord CJ, Tutt ANJ, Johnson DA, Richardson TB, et al. Targeting the DNA repair defect in BRCA mutant cells as a therapeutic strategy. Nature. 2005;434:917–21.

182. Mistry P, Stewart AJ, Dangerfield W, Okiji S, Liddle C, Bootle D, et al. In Vitro and in Vivo Reversal of P-Glycoprotein-mediated Multidrug Resistance by a Novel Potent Modulator, XR9576. Cancer Res. 2001;61:749–58.

183. Ciszewski WM, Tavecchio M, Dastych J, Curtin NJ. DNA-PK inhibition by NU7441 sensitizes breast cancer cells to ionizing radiation and doxorubicin. Breast Cancer Res Treat. 2014;143:47–55.

184. Jones TR, Carpenter AE, Sabatini DM, Golland P. Methods for High-Content, High-Throughput Image-Based Cell Screening. Proc Work Microsc Image Anal with Appl Biol. 2006. page 65–72.

185. Zimmermann T. Spectral Imaging and Linear Unmixing in Light Microscopy. In: Rietdorf J, editor. Microsc Tech. Springer, Berlin, Heidelberg; 2005. page 245–65.

186. Ivashkevich A, Redon CE, Nakamura AJ, Martin RF, Martin OA. Use of the γ-H2AX assay to monitor DNA damage and repair in translational cancer research. Cancer Lett. 2012;327:123–33.

187. Apostolou P, Toloudi M, Kourtidou E, Mimikakou G, Vlachou I, Chatziioannou M, et al. Use of the comet assay technique for quick and reliable prediction of in vitro response to chemotherapeutics in breast and colon cancer. J Biol Res. 2014;21:14.

188. Chou T-C. Theoretical Basis, Experimental Design, and Computerized Simulation of Synergism and Antagonism in Drug Combination Studies. Pharmacol Rev. 2006;58:621–81.

189. Chen S, Lahav G. Two is better than one; toward a rational design of combinatorial therapy. Curr Opin Struct Biol. 2016;41:145–50.

190. Greene JM, Levy D, Herrada SP, Gottesman MM, Lavi O. Mathematical Modeling Reveals That Changes to Local Cell Density Dynamically Modulate Baseline Variations in Cell Growth and Drug Response. Cancer Res. 2016;76.

191. Swanton C. Intratumor Heterogeneity: Evolution through Space and Time. Cancer Res. 2012;72:4875–82.

192. Marusyk A, Almendro V, Polyak K. Intra-tumour heterogeneity: a looking glass for cancer? Nat Rev Cancer. 2012;12:323–34.

193. Nowell P. The clonal evolution of tumor cell populations. Science. 1976;194:23–8.

194. Merlo LMF, Pepper JW, Reid BJ, Maley CC. Cancer as an evolutionary and ecological process. Nat Rev Cancer. 2006;6:924–35.

195. Calbo J, van Montfort E, Proost N, van Drunen E, Beverloo HB, Meuwissen R, et al. A Functional Role for Tumor Cell Heterogeneity in a Mouse Model of Small Cell Lung Cancer. Cancer Cell. 2011;19:244–56.

196. Michor F, Iwasa Y, Nowak MA. Dynamics of cancer progression. Nat Rev Cancer. 2004;4:197–205.

197. Gatenby RA, Vincent TL. An Evolutionary Model Of Carcinogenesis. Cancer Res. 2003;63.

198. Chmielecki J, Foo J, Oxnard GR, Hutchinson K, Ohashi K, Somwar R, et al. Optimization of dosing for EGFR-mutant non-small cell lung cancer with evolutionary cancer modeling. Sci Transl Med. 2011;3:90ra59.

199. Bhang HC, Ruddy DA, Krishnamurthy Radhakrishna V, Caushi JX, Zhao R, Hims MM, et al. Studying clonal dynamics in response to cancer therapy using high-complexity barcoding. Nat Med. 2015;21:440–8.

200. Kreso A, O'Brien CA, van Galen P, Gan OI, Notta F, Brown AMK, et al. Variable Clonal Repopulation Dynamics Influence Chemotherapy Response in Colorectal Cancer. Science. 2013;339:543–8.

201. Marusyk A, Tabassum DP, Altrock PM, Almendro V, Michor F, Polyak K. Non-cell-autonomous driving of tumour growth supports sub-clonal heterogeneity. Nature. 2014;514:54–8.

202. Hata AN, Niederst MJ, Archibald HL, Gomez-Caraballo M, Siddiqui FM, Mulvey HE, et al. Tumor cells can follow distinct evolutionary paths to become resistant to epidermal growth factor receptor inhibition. Nat Med. 2016;22:262–9.

203. Trock BJ, Leonessa F, Clarke R. Multidrug Resistance in Breast Cancer: a Meta-analysis of MDR1/gp170 Expression and Its Possible Functional Significance. J Natl Cancer Inst. 1997;89:917–31.

204. Burges CJC. A Tutorial on Support Vector Machines for Pattern Recognition. Data Min Knowl Discov. 1998;2:121–67.

205. Dordal MS, Ho AC, Jackson-Stone M, Fu YF, Goolsby CL, Winter JN. Flow cytometric assessment of the cellular pharmacokinetics of fluorescent drugs. Cytometry. 1995;20:307–14.

206. Moreno E, Basler K. dMyc Transforms Cells into Super-Competitors. Cell. 2004;117:117–29.

207. Moreno E. Is cell competition relevant to cancer? Nat Rev Cancer. 2008;8:141–7.

208. Abraham EH, Prat AG, Gerweck L, Seneveratne T, Arceci RJ, Kramer R, et al. The multidrug resistance (mdr1) gene product functions as an ATP channel. Proc Natl Acad Sci U S A. 1993;90:312–6.

209. Broxterman HJ, Pinedo HM, Kuiper CM, Schuurhuis GJ, Lankelma J. Glycolysis in P-glycoprotein-overexpressing human tumor cell lines Effects of resistance-modifying agents. FEBS Lett. 1989;247:405–10.

210. Silva AS, Kam Y, Khin ZP, Minton SE, Gillies RJ, Gatenby RA. Evolutionary Approaches to Prolong Progression-Free Survival in Breast Cancer. Cancer Res. 2012;72:6362–70.

211. Pfeiffer T, Schuster S, Bonhoeffer S. Cooperation and Competition in the Evolution of ATP-Producing Pathways. Science. 2001;292:504–7.

212. McGranahan N, Swanton C. Clonal Heterogeneity and Tumor Evolution: Past, Present, and the Future. Cell. 2017;168:613–28.

213. Greaves M, Maley CC. Clonal evolution in cancer. Nature. 2012;481:306–13.

214. Nowak MA, Sigmund K. Evolutionary Dynamics of Biological Games. Science. 2004;303:793–9.

215. Enriquez-Navas PM, Wojtkowiak JW, Gatenby RA. Application of Evolutionary Principles to Cancer Therapy. Cancer Res. 2015;75:4675–80.

216. Aldonza MBD, Hong J-Y, Lee SK. Paclitaxel-resistant cancer cell-derived secretomes elicit ABCB1-associated docetaxel cross-resistance and escape from apoptosis through FOXO3a-driven glycolytic regulation. Exp Mol Med. 2017;49:e286.

217. Obenauf AC, Zou Y, Ji AL, Vanharanta S, Shu W, Shi H, et al. Therapy-induced tumour secretomes promote resistance and tumour progression. Nature. 2015;520:368–72.

218. Deisboeck TS, Wang Z, Macklin P, Cristini V. Multiscale cancer modeling. Annu Rev Biomed Eng. 2011;13:127–55.

219. Vaidya VG, Alexandro FJ. Evaluation of some mathematical models for tumor growth. Int J Biomed Comput. 1982;13:19–36.

220. Gerlee P. The model muddle: In search of tumor growth laws. Cancer Res. 2013;73:2407–

11.

221. Powathil GG, Swat M, Chaplain M a J. Systems oncology: towards patient-specific treatment regimes informed by multiscale mathematical modelling. Semin Cancer Biol. 2015;30:13–20.

222. Sinek JP, Sanga S, Zheng X, Frieboes HB, Ferrari M, Cristini V. Predicting drug pharmacokinetics and effect in vascularized tumors using computer simulation. J Math Biol. 2008;58:485–510.

223. Frieboes HB, Edgerton ME, Fruehauf JP, Rose FR a J, Worrall LK, Gatenby R a, et al. Prediction of drug response in breast cancer using integrative experimental/computational modeling. Cancer Res. 2009;69:4484–92.

224. Clancy CE, An G, Cannon WR, Liu Y, May EE, Ortoleva P, et al. Multiscale Modeling in the Clinic: Drug Design and Development. Ann Biomed Eng. 2016;44:2591–610.

225. Strebhardt K, Ullrich A. Paul Ehrlich's magic bullet concept: 100 years of progress. Nat Rev Cancer. 2008;8:473–80.

226. Kummar S, Chen HX, Wright J, Holbeck S, Millin MD, Tomaszewski J, et al. Utilizing targeted cancer therapeutic agents in combination: novel approaches and urgent requirements. Nat Rev Drug Discov. 2010;9:843–56.

227. Yamada KM, Cukierman E. Modeling Tissue Morphogenesis and Cancer in 3D. Cell. 2007;130:601–10.

228. Primeau AJ, Rendon A, Hedley D, Lilge L, Tannock IF. The distribution of the anticancer drug doxorubicin in relation to blood vessels in solid tumors. Clin Cancer Res. 2005;11:8782–8.

229. Lankelma J, Dekker H, Luque FR, Luykx S, Hoekman K, van der Valk P, et al. Doxorubicin gradients in human breast cancer. Clin Cancer Res. 1999;5:1703–7.

230. Zhao Y, Butler EB, Tan M. Targeting cellular metabolism to improve cancer therapeutics. Cell Death Dis. 2013;4:e532.

231. Lord CJ, Ashworth A. The DNA damage response and cancer therapy. Nature. 2012;481:287–94.

232. Tomayko MM, Reynolds CP. Determination of subcutaneous tumor size in athymic (nude) mice. Cancer Chemother Pharmacol. 1989;24:148–54.

233. Barnes SL, Sorace AG, Loveless ME, Whisenant JG, Yankeelov TE. Correlation of tumor characteristics derived from DCE-MRI and DW-MRI with histology in murine models of breast cancer. NMR Biomed. 2015;28:1345–56.

234. Motlagh NSH, Parvin P, Ghasemi F, Atyabi F. Fluorescence properties of several chemotherapy drugs: doxorubicin, paclitaxel and bleomycin. Biomed Opt Express. 2016;7:2400–6.

235. Landis CS, Li X, Telang FW, Coderre JA, Micca PL, Rooney WD, et al. Determination of the MRI contrast agent concentration time course in vivo following bolus injection: effect of equilibrium transcytolemmal water exchange. Magn Reson Med. 2000;44:563–74.

236. Loveless ME, Halliday J, Liess C, Xu L, Dortch RD, Whisenant J, et al. A quantitative comparison of the influence of individual versus population-derived vascular input functions on dynamic contrast enhanced-MRI in small animals. Magn Reson Med. 2012;67:226–36.